UNIVERSITY OF SOUTHAMPTON

FACULTY OF PHYSICAL SCIENCES AND ENGINEERING

Department of Physics

Doctor of Philosophy

TOWARDS AN INTEGRATED ION TRAP - CAVITY SYSTEM WITH STRONG COUPLING FOR MULTIPLE IONS

by Jack William Neiphie Morphew

Thesis for the degree of Doctor of Philosophy

September 2016

UNIVERSITY OF SOUTHAMPTON

ABSTRACT

FACULTY OF PHYSICAL SCIENCES AND ENGINEERING

Department of Physics

Doctor of Philosophy

TOWARDS AN INTEGRATED ION TRAP-CAVITY SYSTEM WITH STRONG COUPLING FOR MULTIPLE IONS

by Jack William Neiphie Morphew

Precise control over internal states of atomic ions in ion traps has been possible for many years enabling high precision spectroscopy of atomic transitions. Trapped ions are suitable candidates for quantum information processing due to their long storage times, low decoherence rates and high readout efficiency. Recent advances in micro-machining fibre optic mirrors and integrated fibre optic-ion trap systems for cavity QED allows one to realise strong coupling between an ion and a cavity mode by reducing the mode volume. For strong ion-cavity coupling, deterministic transfer of quantum states between ions and photons is possible.

We have designed and constructed a miniaturised linear Paul trap with an integrated optical cavity, intended for coupling multiple ions to the cavity mode. The RF-electrode separation is 50μm, while the endcap separation is 350μm. The endcap electrodes are narrow tubes of inner diameter 300μm allowing optical fibers through the tubes to form the cavity. The trap depth we calculate to be 650meV for a 10V applied potential at 20MHz. The $4P_{1/2} \rightarrow 3D_{3/2}$ transition of the atomic ion $^{40}Ca^{+}$ with $\Gamma = 24\pi\times$ 22MHz can be coupled to an optical fibre Fabry-Pérot cavity with length of 380μm, finesse of 33,000 and cavity linewidth $\kappa = 2\pi\times$11MHz. The ion-cavity coherent coupling $g = 2\pi \times$ 19.5MHz of this system will put it in single-ion strong coupling regime with cooperativity, C=1.5.

Contents

List of Figures

Acknowledgements

This work has been completed in the group of Matthias Keller between 2012 and 2016 in a joint project between the University of Sussex and Southampton University. It has been my honour to work in the lab of such a talented and dedicated group. Matthias in particular I'd like to thank for his teaching, leadership, everlasting patience, and especially understanding. I wish the lab all the best in the future and look forward to hearing about the quantum internet straight out of Sussex.

Thank you to Arijit Sharma for the last 18 months of co-working on the project. Your experience helped pull the project through the last few stages. Thanks to Hiroki Takahashi, for being the answer to so many questions across the four years - especially relating to fibre stuff! It was a pleasure to work with you and your good humour.

Thanks to Alan Butler, Alan Meyers, Bob, and the rest of the workshop staff for making the entire project possible. Your experience and suggestions made more of an impact on the final experiment than you may think!

Thanks to Hendrik Ulbricht at Southampton University for being my supervisor and point of contact for all things Southampton.

Sadly, I joined the group properly shortly after Wolfgang Lange's passing in 2012. However, during my time at Sussex as an undergraduate, I had the chance to be taught by him in programming, atom-light interactions, and the occasional moment in the undergraduate labs. Your good humour and talent is still fondly remembered, Wolfgang.

To everyone else in the group, many thanks to Amy for our molecule-centric chats and puzzling over nitrogen, thanks to Markus for bringing such an uplifing enthusiasm into the lab everyday, thanks to Ezra for always having a useful contribution to make, and for having a critical

eye when it's needed. Gurpreet, it was fun passing the fibre-machining baton to you - good luck! Good luck to Callan with his new trap, and thanks to you and a series of project students for setting up the new lasers. Previous group members as well - Nic, Kevin, Stephen, thanks so much for your introduction to the lab(s) all those years ago, the time has gone fast!

Thanks to my family, particularly my parents for helping support me through the whole process, and beyond. I wouldn't be here without the amazing start you gave me. And Gracie, thank you for being there to celebrate and enjoy the good times, help me through the difficult times, believe in me during the despairing times, and laugh with me during the hardest times. Thanks finally to my Nan, who always thought I could get here.

Declaration of Authorship

I, Jack Morphew declare that this thesis and the work presented in it are my own and has been generated by me as a result of my own original research.

I confirm that:

1. This work was done wholly or mainly while in candidature for a research degree at this University;
2. Where any part of this thesis has previously been submitted for a degree or any other qualification at this University or any other institution, this has been clearly stated;
3. Where I have consulted the published work of others, this is always clearly attributed;
4. Where I have quoted from the work of others, the source is always given. With the exception of such quotations, this thesis is entirely my own work;
5. I have acknowledged all main sources to help;
6. Where the thesis is based on work done by myself jointly with others, I have made clear exactly what was done by others and what I have contributed myself;
7. Parts of this work have been published as: H. Takahashi, J. Morphew, F.Oruĉević, A. Noguchi, E. Kassa, M. Keller (2015) Novel laser machining of optical fibers for long cavities with low birefringence, Optics Express Vol 22, Issue 25 doi: 10.1364/OE.22.031317

Signed
Date: 25/09/2016

Chapter 1

Motivation and Background

The 20th century beckoned a golden age of discovery in physics, bringing forth the dramatic, new quantum theory that threatened existing contemporary understandings of how the world functioned. The century progressed and the theory was developed, and up until the 1950s it was widely believed that despite the *concept* of single atom interactions being continually better understood, the *realisaton* of performing them would remain impossible.[1] However, the invention of the quadropole mass filter in 1953 by Wolfgang Paul would eventually lead to this being demonstratably false. By the late 1970s, radiative damping of trapped ions' motion using the discovery of the laser from 1960 lead up to the first single ion, Ba^+ being trapped in 1980 [1]. From this point, the field has branched repeatedly into various studies of fundamental and particle physics, chemical-physics [3][4][5][6], and the relatively new field of quantum information procesing using cavity quantum electrodynamics

[1] Erwin Schrödinger in 1952 said "We never experiment with just one electron or atom or (small) molecule. In thought-experiments, we sometimes assume that we do; this invariable entails ridiculous consequences."[2]

(cQED) [7][8][9].

Cavity quantum electrodynamics has developed from a research topic of purely fundamental interest to a versatile tool in quantum information processing[11]. In order to obtain strong coupling between atomic particles and a cavity, and to create compact systems, several implementations of micro-cavities have been pursued[10][12][13]. Among these fiber-based Fabry-Perot cavities (FFPC) are attracting increasing attention. Due to their quality and compactness, FFPCs are being employed in a wide range of experiments [14][15][16] and research continues into their production and usage [17][18][19][20].

This thesis posits that the DiVincenzo criteria, can be satisified with a strongly coupled ion-cavity system. In summary, each are addressed as follows:

1. *A scalable physical system with well characterized qubits.* By means of laser cooling, the level structure of atomic ions are very well defined, and a given state can be used as a qubit state. Scalability can be achieved merely through increasing the number of ions present, or by linking two spatially separate ions in different traps via a flying qubit, with information encoded into its polarization state.

2. *The ability to initialize the state of the qubits to a simple state.* State preparation of ions is a routine method in many existing atomic ion experiments.

3. *Long relevant decoherence times, much longer than the gate operation time.* In an ion-cavity coupled system in the strong regime,

(as discussed in section 4.5) the coherence times are much longer than the decoherent processes.

4. *A universal set of quantum gates.* In classical computing, a universal gate is logically complete, which is to say it can complete any Boolean function without the addition of a second type of gate. NAND and NOR gates are two such cases. In quantum computing this definition still holds true, where the 'controlled NOT' gate can be used to build any gate required. The internal states of atomic ions are easily manipulated (depending on species) and systems where controlled unitary operations can be completed are available.

5. *A qubit-specific measurement capability.* State readout is available through optical means both destructively, and now non-destructively for trapped ion crystals.

6. *The ability to interconvert stationary and flying qubits.* Atomic ion qubits as discussed can work as a stationary qubit, which can emit a flying qubit in the form of a photon. This photon carries information encoded into its polarization state. By introducing a cavity around the trapped ion, the photon's 'emission trajectory' is now enhanced along the cavity axis for detection or further transmission.

7. *The ability faithfully to transmit flying qubits between specified locations.* Once a photon is output into the cavity mode and then exits the cavity, this photon can be coupled into an optical fiber

for long distance communications to a similar system designed to receieve the qubit.

An ion-cavity system presents the ideal solution, combining highly localised, well defined ions with long interrogation periods, with the transmittive qualities of a strongly coupled atom-photon system.

Chapter 2

Ion Trapping

Trapped ions are highly localised and interact minimally with the environment as they are isolated by strong electric fields generated by a trapping potential. These properties make them ideal for a range of experiments investigating quantum mechanical aspects of light matter interaction, such as encoding information in quantum processes[22] and high precision measurements, such as high resolution spectroscopy and for atomic clocks[23]. The most commonly used varities of trap system are the Penning[24] and Paul[25] traps. The general geometrical configuration of both types of traps are the same. In the Penning trap, a confining potential is produced by a combination of static electric and magnetic fields, while the Paul trap operates by applying an oscillating electric field to create a time-averaged potential minimum in which ions are trapped. In this thesis we are only concerned with the latter design, the linear Paul trap, which was derived from the quadropole mass spectrometer and uses oscillating electric fields at radiofrequencies to 'trap' ions.

2.1 Linear Paul Trap

Application of an external multipole static electric field is insufficient to trap ions. From Gauss' law[26] the divergence of the electric field, E is given by

$$\vec{\nabla} \cdot \vec{E} = \frac{\rho}{\epsilon_0} \tag{2.1}$$

where ρ is the charge density and ϵ_0 is the permitivity of free space. In a vacuum, the charge density and thus electric field divergence is zero, as per equation 2.1. Therefore in this externally applied field case, the net field passing through any region within the 'trapping' potential is always zero - every field line entering the trapping region also must leave because there is no charge to act as a field 'sink,' as shown in figure 2.1. The potential V is described by Poisson's equation

$$\nabla^2 V = \frac{\rho}{\epsilon_0} \tag{2.2}$$

which in a vacuum reduces to Laplace's equation,

$$\nabla^2 V = 0. \tag{2.3}$$

Harmonic solutions to Laplace's equations for a three-dimensional system have the form

$$V(x, y, z) = V_0(\alpha x^2 + \beta y^2 + \gamma z^2) \tag{2.4}$$

where V_0 is the potential amplitude, and $\alpha, \beta \text{and} \gamma$ are coeffecients

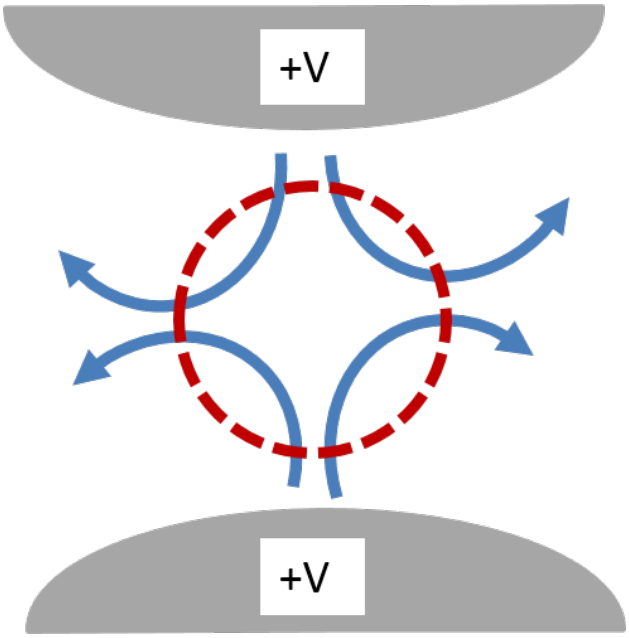

Figure 2.1: Simple illustration of the field divergence in a vacuum with two electrodes at a potential of +V. The dashed red line indicates the potential surface around the geometric center. The blue arrows indicate the field lines passing through the region.

that determine the direction and amplitude of the potential along each axis. The constraint of Laplace's equation means that

$$\alpha + \beta + \gamma = 0 \tag{2.5}$$

which, for example, can be obtained if $\alpha = 1, \beta = -1, \text{and} \gamma = 0$. This simplifies to a two-dimensional problem where the externally applied field produces a saddle-potential which is neutral along one axis, confining along one other but the third axis is *anti-confining*.[27] This saddle-potential has no global minima to trap an ion in all three

dimensions.[1] However if the field is dynamic and allowed to oscillate at

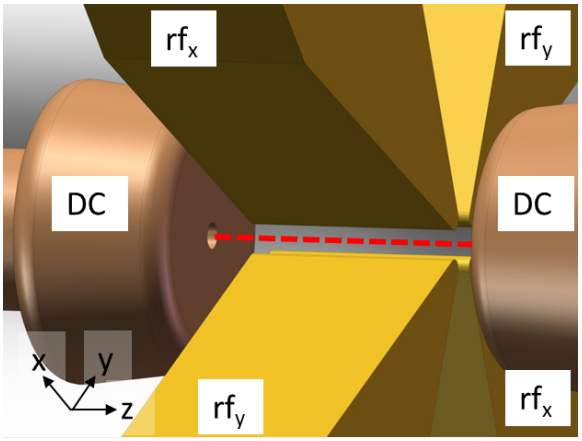

Figure 2.2: A 3-D model of the linear Paul trap electode setup to be used. The four radial-electodes marked rf$_{x/y}$ are connected diagonally in order to form the saddle potential required for trapping in the x-y plane by applying $\pm V(t)$. The two electodes marked DC along the trap axis are held at a non-varying potential to trap and manipulate ions along the z-axis. The dashed line indicates the trapping axis.

a rate fast enough to switch the confining and anti-confining axes before a trapped ion can escape, a time-averaged potential well is formed, referred to as the pseudo-potential. This is realised by applying an RF potential, $V(t)$, to one diagonal pair of radial electrodes, a figure of which is presented in figure 2.2. The other diagonal pair is supplied $-V(t)$. The radial electrode potential has an amplitude of

$$V(t) = V_{RF}\cos(\Omega t) \tag{2.6}$$

where t is time and V_{RF} is a sinusoidally varied potential at fre-

[1] This inability to trap an ion sample with a static field is known as Earnshaw's Theorem.

quency Ω. The radial trapping potential generated by the RF electrodes is then

$$V(x,y,t) = -V_{RF}\cos(\Omega t)\frac{x^2-y^2}{2r_0^2} \tag{2.7}$$

where r_0 is defined by the geometry of the system. For trapping along the z-axis a separate harmonic DC potential is supplied to the axial electrodes of V_{DC}. This produces an axial confinement of

$$\phi(z) = \frac{U_{DC}}{2z_0}(z^2)\eta \tag{2.8}$$

where z_0, is the inter-electrode distance along the trap axis, and η is a geometric factor accounting for the geometry of the electrodes. The total radial trapping potential from all DC and RF electrodes contributions is therefore

$$\phi(x,y,t) = -V_{RF}\cos(\Omega t)\frac{x^2-y^2}{2r_0^2} - \frac{1}{2}\eta V_{DC}\frac{x^2+y^2}{z_0^2}. \tag{2.9}$$

An ion placed in this field with mass m, and charge e, will obey the following equations of motion along the x and y axes,

$$\ddot{x} + \frac{Q}{m}\frac{\delta\phi(x,y,t)}{\delta x} = 0 \tag{2.10}$$

$$\ddot{y} - \frac{Q}{m}\frac{\delta\phi(x,y,t)}{\delta y} = 0 \tag{2.11}$$

where the ion will experience an oscillation in the x-y plane, and maintain a steady velocity along the z-axis. These can be written in

the form of two Mathieu differential equations with the substitutions

$$a = \frac{4eV_{DC}}{mr_0^2\Omega^2} \tag{2.12}$$

$$q = \frac{2eV_{RF}}{mr_0^2\Omega^2} \tag{2.13}$$

$$\zeta = \Omega t/2 \tag{2.14}$$

which when substituted into equations 2.10 and2.11 become

$$\frac{d^2x}{d\zeta^2} + (a - 2q\cos(2\zeta)x = 0 \tag{2.15}$$

$$\frac{d^2y}{d\zeta^2} - (a - 2q\cos(2\zeta)y = 0 \tag{2.16}$$

which have the form of the cannonical Mathieu equation[27]

$$\frac{d^2u}{d\zeta^2} + (a - 2q\cos(2\zeta)u = 0 \tag{2.17}$$

which have known stable and unstable solutions depending on the a and q parameters. In the context of ion trapping, a stable solution refers to the ion's motion being bounded at all times, i.e. trapped. Figure 2.3 shows the stability region for small a and q values for a linear paul trap.

In the approximation that $|q|, |a| \ll 1$ the solutions of 2.17 and 2.16 can be simplfied to

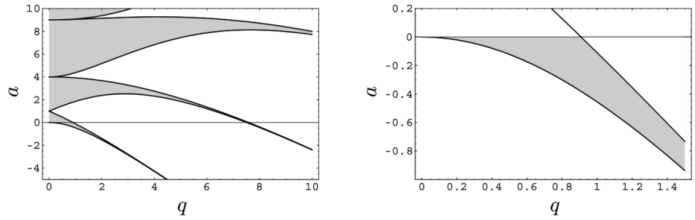

Figure 2.3: Highlighted (grey) stable solutions of the Mathieu equations. The left figure shows stable solutions to equations 2.17. The right figure shows the relevant a and q space for a linear Paul trap.[28]

$$x(t) = x_0(1 - q\cos(\Omega t))\cos(\omega_r t) \tag{2.18}$$

$$y(t) = y_0(1 - q\cos(\Omega t))\cos(\omega_r t) \tag{2.19}$$

which highlights an additional oscillating term at frequency ω_r which is the radial secular frequency given by

$$\omega_r = \frac{\Omega}{2}\sqrt{q^2/2 \pm a}. \tag{2.20}$$

The equation of motion for the axial direction from the harmonic potential 2.8 is given by

$$\ddot{z} + \frac{2e\eta}{mz_0^2}V_{DC}z = 0 \tag{2.21}$$

which describes a simple harmonic oscillation along the trap axis, with solution

$$z(t) = z_0\cos(\omega_z t) \tag{2.22}$$

where ω_z is the axial secular frequency given by

$$\omega_z = \sqrt{\frac{2e\eta V_{DC}}{mz_0^2}} \tag{2.23}$$

Finally, equations 2.18, 2.19 and 2.22 can be averaged and approximated to one time-averaged harmonic pseudo-potential in all three dimensions

$$\Phi(x, y, z) = \frac{1}{2}(\omega_r^2 r^2 + \omega_z^2 z^2) \tag{2.24}$$

with $r^2 = x^2 + y^2$.

Equations 2.18 and 2.19 describe the ion's oscillation in the radial plane as a summation of two sinusoidal motions overlapped. The term being driven by the external trapping field at a rate Ω is much faster, but typically lower amplitude than the secular frequency since $q \ll 1$, and is referred to as micromotion. An example of this motion overlaid on the slower secular motion is shown in figure 2.4.

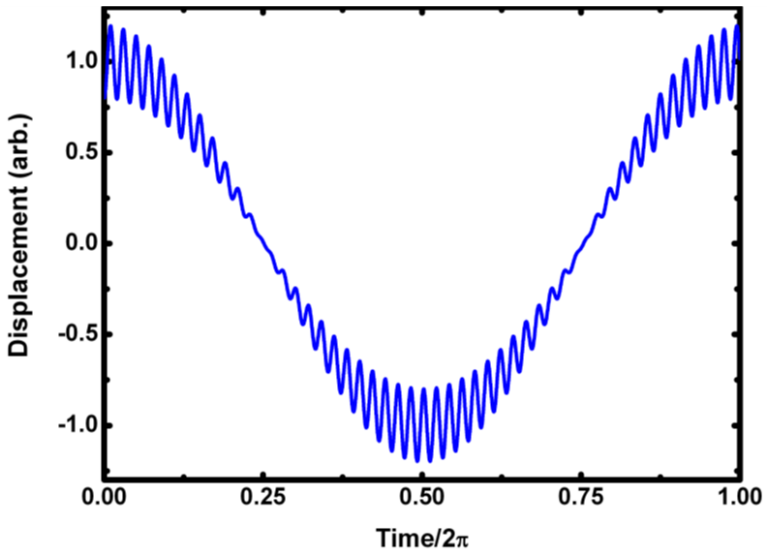

Figure 2.4: Graph of an ion's displacement during one cycle of the driving trapping potential. The secular oscillation amplitude is normalised to 1 unit, $q = 0.2$ and $\Omega = 50 \cdot \omega_r$ [29]

Chapter 3

Laser Cooling

Once confined by the electric trapping potential of the trap, further techniques are required localise the ions into the center of the trap to be overlapped with the cavity mode. Doppler laser cooling is one mechanism for cooling a trapped atomic ion's translational motion. It is based on the Doppler-shifted-absorption and emission of photons by an ion in a laser field. The process can be understood from the interaction of the ion with the light field described by the Hamiltonian,

$$H = H_{\text{atom}} + H_{\text{laser}}. \tag{3.1}$$

The Hamiltonian of a two-level atom with excited state $|e\rangle$ and ground state $|g\rangle$ is

$$H_{\text{atom}} = \hbar\omega_g |g\rangle \langle g| + \hbar\omega_e |e\rangle \langle e| \tag{3.2}$$

and the laser interaction Hamiltonian is given by

$$H_{\text{laser}} = -(\sigma_+ + \sigma_-)\mu_{ge}E, \tag{3.3}$$

where μ_{ge} is the transition dipole moment, $\sigma_+ = |g\rangle \langle e| e^{i\omega_{ge}t}$, $\sigma_- = |e\rangle \langle g| e^{i\omega_{ge}t}$, $\omega_{ge} = \omega e - \omega g$ and E is the electric field of the laser light:

$$E = \frac{1}{2}E_0(e^{-i\omega_L t} + e^{i\omega_L t}) \tag{3.4}$$

where ω_L is the angular frequency of the laser light. The Rabi frequency, Ω of the atom in the light field is given by

$$\Omega = \frac{\mu_{ge}E_0}{\hbar}. \tag{3.5}$$

Substituting equations 3.4 and 3.5 into equation 3.3 gives

$$H_{\text{laser}} = -\frac{\hbar\Omega}{2}(\sigma_+ + \sigma_-)(\mu_{ge})(e^{-i\omega_L t} + e^{i\omega_L t}). \tag{3.6}$$

Using the rotating wave approximation, this becomes

$$H_{\text{laser}} = -\frac{\hbar\Omega}{2}(\sigma_+ e^{-i\Delta t} + \sigma_- e^{i\Delta_L t}). \tag{3.7}$$

where $\Delta = \omega_L - \omega_{ge}$ is the detuning of the laser field frequency from the atomic resonance frequency. The spontaneous emission of the system can be included using the density matrix, ρ:

$$\rho = \begin{bmatrix} \|\mathrm{C}_1\|^2 & \mathrm{C}_1 C_2^* \\ \mathrm{C}_2 C_1^* & \|\mathrm{C}_2\|^2 \end{bmatrix}$$

The time evolution of the system is given by the master equation,

$$\frac{d\rho}{dt} = \frac{1}{i\hbar}[H, \rho] + \Lambda\rho \tag{3.8}$$

where

$$\Lambda\rho = \frac{-\Gamma}{2}(\sigma_+\sigma_-\rho - 2\sigma_-\rho\sigma_+ + \rho\sigma_+\sigma_-) \tag{3.9}$$

and Γ is the spontaneous decay rate, $\Gamma = \frac{\omega_{ge}^3 \mu_{ge}^2}{\pi\epsilon_0\hbar c^3}$. The time evolution of each element of the density matrix is given by the optical Bloch equations:

$$\frac{d\rho_{gg}}{dt} = -\Gamma\rho_{gg} + \frac{i\Omega}{2}(\bar{\rho}_{eg} - \bar{\rho}_{ge}), \tag{3.10}$$

$$\frac{d\bar{\rho}_{ge}}{dt} = \left(i\delta - \frac{\Gamma}{2}\right)\bar{\rho}_{ge}\frac{i\Omega}{2}(\rho_{ee} - \bar{\rho}_{gg}), \tag{3.11}$$

$$\frac{d\rho_{ee}}{dt} = -\frac{d\rho_{gg}}{dt}, \tag{3.12}$$

where $\bar{\rho} = e^{i\omega_L t}\rho_{ge}$ and $\delta = \omega_L - \omega_{ge}$. Since the population is conserved, the system reaches a steady state excited population of[21]

$$\rho_{ee} = \frac{s_0/2}{1 + s_0 + (2\delta/\Gamma)^2}, \tag{3.13}$$

where $s_0 = 2\Omega^2/\Gamma^2$ is the saturation parameter. The scattering rate of the atom in a the laser field is given by the product of the

excited state population and the spontaneous decay rate, which in that saturated case is

$$\gamma_{\text{scatter}} = \Gamma\rho_{ee} = \Gamma\rho ee = \frac{\Gamma s_0/2}{1 + s_0 + (2\delta/\Gamma)^2}. \tag{3.14}$$

The absorption of a photon by the atom imparts a momentum 'kick.' The force experienced by the atom is given by the momentum transfer from each photon interaction, $\hbar\vec{k}$ so the total force is $\gamma_{\text{scatter}}\hbar\vec{k}$. An atom absorbing a photon from the laser beam experiences a radiation pressure from this momentum along the laser axis. The motion of the ion at velocity along the laser axis is $v_k = \vec{v} \cdot \vec{k}$. The induced motion from the radiation pressure, results in a shift of the laser detuning to $\delta + v_k k$. Combining this with equation 3.13 and 3.14 the force on an ion at velocity v_k is

$$\vec{F} = \hbar\vec{k}\frac{\Gamma s_0/2}{1 + s_0 + (2(\delta + v_k k/\Gamma)^2}. \tag{3.15}$$

For small velocities, the force can be approximated by a Taylor expansion around $v_k = 0$:

$$\vec{F}(v_k) = \frac{\hbar\vec{k}\Gamma s_0/2}{1 + s_0 + (2(\delta/\Gamma)^2} - \frac{4\hbar|\vec{k}|\delta}{\Gamma} \cdot \frac{s_0\vec{k}}{(1 + s_0 + (2(\delta/\Gamma)^2)^2} \tag{3.16}$$

which shows for small v_k the total force experienced by the ion is made up of a constant light pressure in the direction of the laser, as well as a force dependant on the collinear velocity of the ion with respect to the laser beam. For a detuning of $\delta < 0$ the force opposes the motion of the

atom. By applying a second, counterpropagating laser with the same intensity and detuning, the ion experiences a restoring force around $v_k = 0$. This application of a velocity dependant restoring force is Doppler cooling. Cooling in this way we can achieve cooled ions down to the temperature of the Doppler limit, T_{Doppler}, given by

$$T_{\text{Doppler}} = \frac{\hbar\Gamma}{2k_B}, \tag{3.17}$$

where k_B is the Boltzmann constant. Aligning the beam to cross the ion's path with a component in all 3 dimensions allows cooling of the motion with a single laser.

3.1 Level Scheme and Cooling of Calcium 40 Ions

Ionised ^{40}Ca is used for these ion trapping experiments for its ideal charge-to-mass ratio, lack of a hyperfine structure and singly ionised state with only a single electron remaining in the outer shell, as well as a closed level structure for continuous laser cooling with only 3 lasers. The calcium is introduced to the trapping region as a beam of neutral atomic calcium emitted by a tantalum tube which is resistively heated, described further in section 7.3. A two-step ionisation scheme is used to produce ions, by first applying a resonant laser on the $4S_0$ to $4P_1$ transition at 422.79167nm. A second, non-resonant 375nm beam is also applied to excite the electron in the $4P_1$ out of the atom.

For $^{40}Ca^+$, the simplest closed level scheme available is the 3-level Λ system, as in figure 3.1. The cooling transition is the $4S_{1/2} \rightarrow 4P_{1/2}$ transition which is addressed using a laser at 397nm. The $4P_{1/2}$ state

then relaxes into either the $4S_{1/2}$ or $3D_{3/2}$ level. An additional 'repump' laser addressing the $3D_{3/2} \rightarrow 4P_{1/2}$ transition is now required to prevent optical pumping into the $3D_{3/2}$ level [46]. This is provided by the 866nm laser with detuning from $4P_{1/2}$ of Δ_R. Population transfer between the $3D_{3/2}$ and $4S_{1/2}$ levels via spontaneous decay can be ignored since they are dipole-forbidden and thus heavily suppressed, occurring with rates of less than 1/s [49].

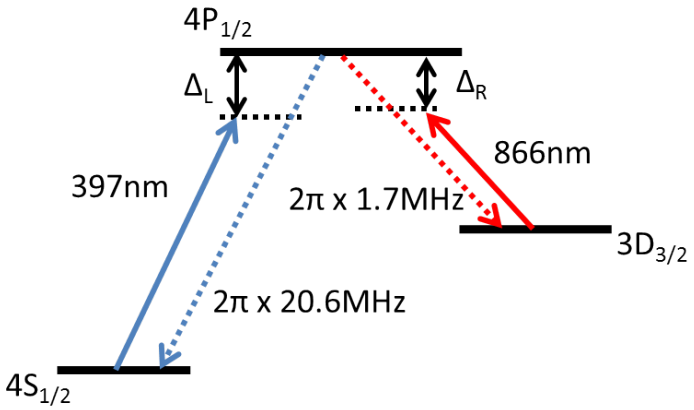

Figure 3.1: 3-level Λ cooling scheme for $^{40}Ca^{+}$. Dashed lines indicate spontaneous emissions

However, this scheme suffers from coherent population trapping between the $4S_{1/2}$ and $3D_{3/2}$ states when the detunings of the cooling and repump lasers are equal. In practice this depopulates the $4P_{1/2}$ state, decreasing cooling effeciency and broadens the transition. Instead, we make use of a cooling technique over 5 levels, as shown in figure 3.2. The replacement of the 866nm repumper with an 850nm laser transfers population to the $4P_{3/2}$ level, preventing the coherent coupling of the

$4S_{1/2}$ and $3D_{3/2}$ levels, and still maintaining a fast relaxation process back to the $4S_{1/2}$ at $2\pi\times21.5$MHz. An additional decay channel is opened between the $4P_{3/2}$ and $3D_{5/2}$ levels, but applying a second repump laser at 854nm prevents population buildup in that state. With no electromagnetically induced transpareny, the system behaves as a two level system capable of cooling Calcium-40 ions to the Doppler cooling limit.

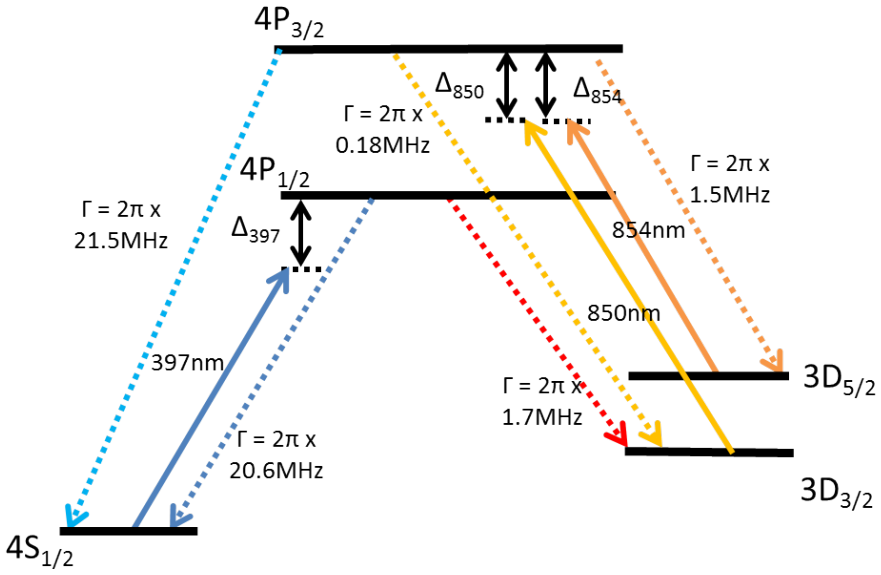

Figure 3.2: $^{40}Ca^{+}$ full cooling scheme, including cooling and rempump lasers. Dashed lines indicate spontaneous emissions, with labelled frequencies being the decay rates. Spontaneous decays between the $3D_{3/2}$ and $3D_{5/2}$ are not shown, as they are strongly suppressed to less than $2\pi\times1$Hz [47].

Chapter 4

Cavity Quantum Electrodynamics

Cavity quantum electrodynamics (commonly shortened to cQED) describes the interaction between an atom or molecule within a cavity. The effect was initially discovered by E. Purcell in 1946 with the enhancement of nuclear magnetic transitions in solid paraffin coupling to an external electric field[30]. This chapter will focus on the cause of this enhancement as well as the potential advantages in optical atom-light interactions.

4.1 Fabry Pérot Cavities

A Fabry Pérot cavity consists of two reflective surfaces facing one another with radius, R, and separated by a distance L. Figure 4.1 shows a schematic of this setup. The light field is subject to the boundary conditions inflicted by the mirrors in a way that the electric field must

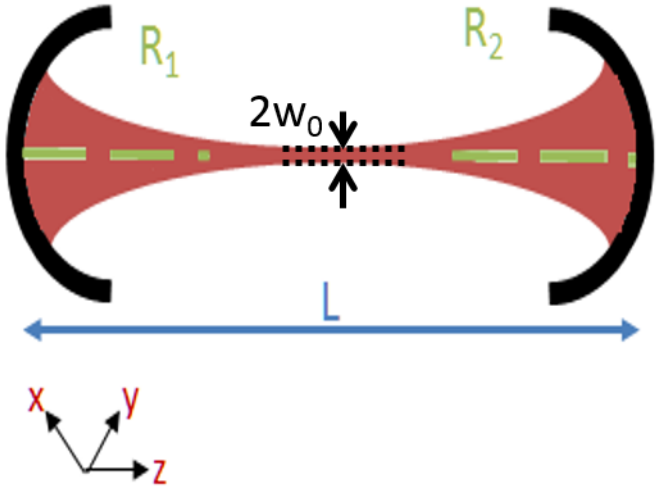

Figure 4.1: Simple FPC schematic with length L, mirrors of radius of curvatures R_1, R_2, and cavity mode with minimum diameter $2w_0$ shown in red.

be zero[26], quantising the field into discrete modes. A standing-wave builds up in the cavity when the cavity length is a half-integral, n, multiple of the wavelength, λ, or:

$$L = n\frac{\lambda}{2} \tag{4.1}$$

The spatial distribution of the electric component of the light field can be written in terms of a longitudinal mode along the cavity axis, $\Phi(x, y, z)$ and two transverse modes, $\Psi_n(x, z)$ and $\Psi_m(y, z)$,

$$E_{nm} = E_0\Psi_n(x, z)\Psi_m(y, z)\Phi(x, y, z) \tag{4.2}$$

where the indices m and n refer to the order of the Transverse

ElectroMagnetic (TEM) modes, and E_0 is the amplitude of the electric field. The distribution of the transverse modes for x-y symmetry are given by

$$\Psi_{m,n}(x,y,z) = \sqrt{\frac{w_0}{w(z)}} H_m\left(\frac{\sqrt{2}(x)}{w(z)}\right) H_n\left(\frac{\sqrt{2}(y)}{w(z)}\right) e^{-\frac{x^2+y^2}{w^2}} \tag{4.3}$$

where $H_{m,n}$ are the Hermite polynomials,[31], w_0 is the waist minimum and $w(z)$ is the waist a position z away from the minimum. The propogation of the beam profile from the minimum waist, w_0 is given by

$$w(z) = w_0\sqrt{1+\left(\frac{z}{z_R}\right)^2} \tag{4.4}$$

where z_R is the Rayleigh range,

$$z_R = \frac{\pi w_0^2}{\lambda} \tag{4.5}$$

and defines the distance along the propogation axis from the minimum waist at which the cross-sectional area of the beam is doubled. Figure 4.2 shows the first twelve Hermite-Gaussian mode profiles.

The first Hermite polynomial, $H_0 = 1$, describes the TEM_{00} mode, which provides the smallest waist and highest intensity at the center of the cavity, which can be represented as a Gaussian profile of the form:

$$\Psi_{00}(x,y,z) = \sqrt{\frac{w_0}{w(z)}} e^{-\frac{x^2+y^2}{w^2}} \tag{4.6}$$

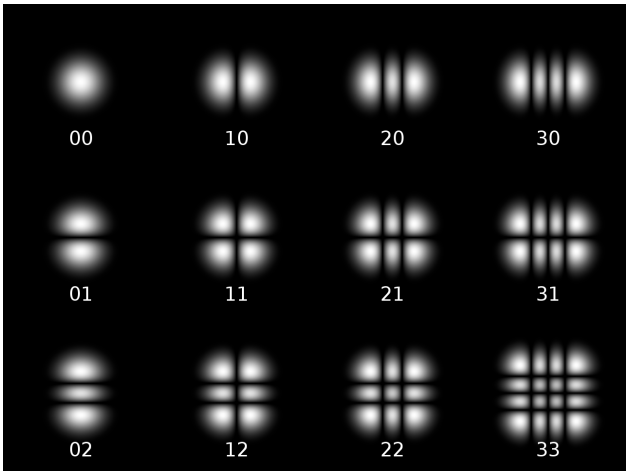

Figure 4.2: First twelve Hermite-Gaussian modes, from TEM_{00} to TEM_{33}[32]

Meanwhile, the longitudinal mode function is given by[31]:

$$\Phi(x, y, z) = \sin\left(kz - (1 + n + m)\arctan\left(\frac{z}{z_R}\right) + \frac{k(x^2 + y^2)}{2R(z)}\right), \tag{4.7}$$

$$k = 2\pi/\lambda, \tag{4.8}$$

$$R(z) = (1 + \left(\frac{z_R}{z}\right)^2) \tag{4.9}$$

where k is the wavenumber, and $R(z)$ is the radius of curvature of the wavefront. The sinusoidal nature of the longitudinal profile is given by the standing wave pattern of the light within the cavity. The first term denoted by this quantity is for a typical plane wave with wavevector k travelling along axis z, second term represents the phase deviation from this plane, and the third term describes the expansion

of the beam waist as it travels from the point of minimum waist. The resonance condition for a stable cavity mode is fulfilled when the phase gained by the light field is an integer multiple of 2π. These resonant frequencies are given by[31]:

$$\nu_{nmq} = \nu_{\mathrm{FSR}} \left(q + \frac{1}{\pi}(1 + n + m) \arccos\left(1 - \frac{L}{R_i}\right)\right) \tag{4.10}$$

where q is the longitudinal mode number of the mode present in the cavity. The frequency spacing between the group of resonances for one longitudinal mode and the next is named the Free Spectral Range (FSR) of the cavity and is given by:

$$\nu_{FSR} = \frac{c}{2L}. \tag{4.11}$$

4.2 Cavity Stability

The stability and waist of the cavity field are defined by its geometry, specifically the ratio of the cavity length, L, and the radius of the curvature of the two mirrors, R_1 and R_2. By using ray matrix transfer analysis on the light path through the cavity, one can define the stability criteria,[34]

$$0 \leq \left(1 - \frac{L}{R_1}\right)\left(1 - \frac{L}{R_2}\right) \leq 1, \tag{4.12}$$

where it is useful to define the dimensionless quantities g_1 and g_2:

$$g_1 = 1 - \frac{L}{R_1}, \tag{4.13}$$

$$g_2 = 1 - \frac{L}{R_2} \tag{4.14}$$

The stability region is shown in figure 4.3. Four cavity configurations are marked and shown inset. Both the stability and shape of the cavity mode are important for cQED, as will be discussed in section 4.6. The concentric cavity has the smallest waist as each mirror focuses to the midpoint of the cavity, but lies on the edge of the stability region. The hemispherical cavity waist is also small, but the minimum waist is positioned on the face of one of the mirrors. The plane-parallel case is highly prone to instability, and has a large mode volume, and finally the confocal cavity has a centrally positioned minimum waist position, but the waist is larger as each mirror's focus is onto the opposing mirror.

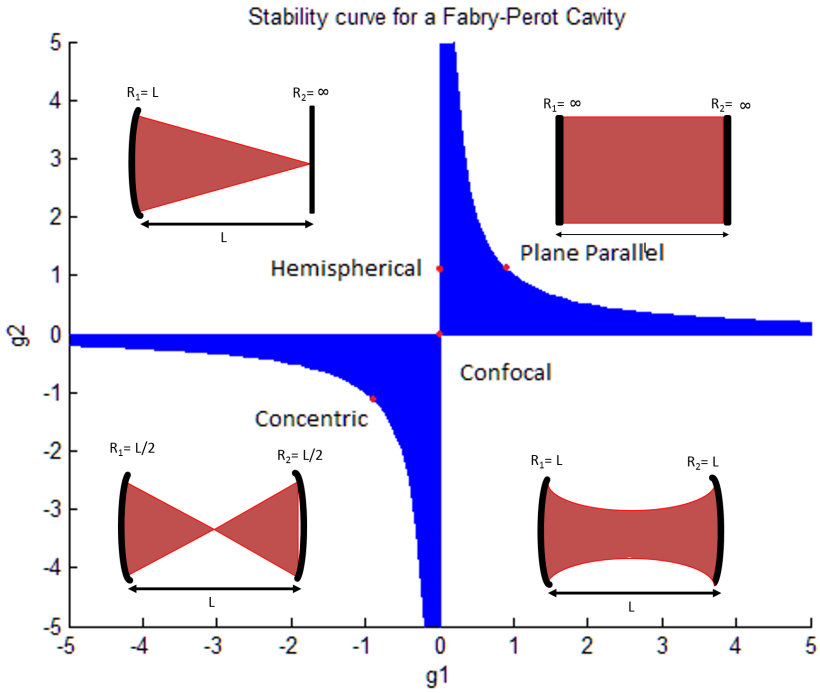

Figure 4.3: Graph of g_1 against g_2, the shaded region contains stable geometrical configurations for a Fabry-Pérot cavity. The four marked locations correspond to the concentric condition, $g_1, g_2 = -1$, the confocal condition, $g_1, g_2 = 0$, the plane-parallel condition, $g_1, g_2 = 1$ and the hemispherical condition, $g1 =_0, g2 =_1$. Inset: Four cavity configurations. Top-right: Plane-parallel, both mirrors are flat. Top-left: Hemispherical, one mirror is flat, while the other is curved to focus onto the opposing mirror. Bottom-left: Concentric, both mirrors are curved, and focus at the midpoint between the mirrors. Bottom-right: Confocal, both mirrors are curved and focused onto the opposing mirror.

4.3 Cavity Finesse

The reflectivity of the mirrors used in an optical cavity dictates the lifetime of a photon remaining between the mirrors, reflecting back and

forth, until it decays into free space or is absorbed by the mirror substrate. This is typically characterised by the FWHM of the resonance peak of the cavity, $\delta\nu$, and comparing it to the FSR of the cavity. This is called the Finesse, $\mathcal{F}$,

$$\mathcal{F} = \frac{\nu_{\mathrm{FSR}}}{\delta\nu} \tag{4.15}$$

and gives a measure of the resolution of the spectrum a given cavity will be able to display, shown pictorally in figure 4.4. The relationship between the FWHM of the cavity, and the cavity decay rate, κ, is:

$$\kappa = \frac{2\pi\delta\nu}{2} \tag{4.16}$$

and thus the relation between cavity decay rate and finesse:

$$\mathcal{F} = \frac{\pi\nu_{\mathrm{FSR}}}{\kappa}. \tag{4.17}$$

The finesse is defined entirely on the optical quality of the cavity mirrors, and can be expressed as a function of the losses at the interface with the cavity mirrors:

$$\mathcal{F} = \frac{2\pi}{L_{\mathrm{TOTAL}}}. \tag{4.18}$$

where L_{TOTAL} is the contribution of losses from transmission out of the cavity, scattering out of the cavity mode, and absorptive losses at the mirror interface. From equations 4.17 and 4.18 the finesse provides a method of measuring the cavity lifetime, as a function of the total cavity losses.

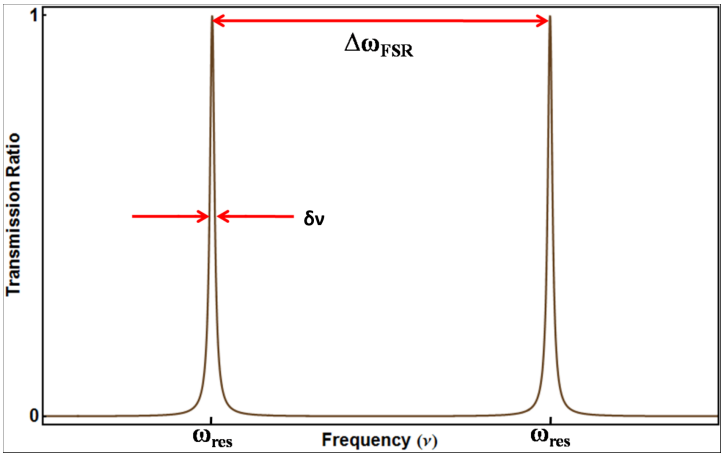

Figure 4.4: Simulated cavity transmission[33]. The resonant cavity frequency, ω_{res}, is repeated each free spectral range, $\Delta\omega_{\mathrm{FSR}}$. The finesse is the ratio of the two values, as in equation refeq$_finesse$

$$\kappa = \frac{\pi}{\mathcal{F}} = \frac{L_{TOTAL}}{2} \tag{4.19}$$

4.4 Atom-Cavity Interaction

In cQED, a quantised light field behaves as an oscillator, with Hamiltonian,

$$\hat{H}_{cavity} = (\hat{a}^{\dagger}\hat{a} + \frac{1}{2})\hbar\omega \tag{4.20}$$

where the $\hat{a}^{\dagger}$ and $\hat{a}$ operators have been introduced which correspond to the annihilation and creation operators respectiely. Similarly, the 'number operator' is defined as[36]

$$\hat{n} = \hat{a}^{\dagger}\hat{a} \tag{4.21}$$

so named for its eigenstates being the number of photons, present within a mode, known as Fock States[1], $|n\rangle$. A Fock State of $|0\rangle$ corresponds to the light field's ground state containing only vacuum, no photons. The energy eigenvalues are then given by the cavity Hamiltonian are given by

$$E_n = (n + \frac{1}{2})\hbar\omega. \tag{4.22}$$

The energy of the vacuum state is non-zero as can be seen from equation 4.22, it retains an offset of $\hbar\omega/2$.

A hypothetical two-level atomic system[2] has two energy eigenstates, an upper 'excited' state $|e\rangle$ with energy $\hbar\omega_e$ and a lower 'ground' state $|g\rangle$ with energy $\hbar\omega_g$. The Hamiltonian for this two-level system is

$$\hat{H}_{atom} = \hbar\omega_g |g\rangle \langle g| + \hbar\omega_e |e\rangle \langle e| .$$

By placing the two-level atomic system within an optical cavity supporting only a single field mode of angular frequency $\omega = w_e - w_g$, the atomic system and light field are in resonance. The coupling of a two level system to a cavity light field is described by the Jaynes-Cumming Hamiltonian[38][39]. Assuming no other losses occur, the complete Hamiltonian for the atom-cavity system is now

$$\hat{H}_{\text{total}} = \hat{H}_{\text{atom}} + \hat{H}_{\text{cavity}} + \hat{H}_{\text{interaction}} \tag{4.24}$$

[1] Also number states

[2] Or a deliberately engineered multi-state atomic system, manipulated to emulate a two-level system.

where $\hat{H}_{interaction}$ is the interaction Hamiltonian between the atom and the cavity field. The form of the interaction term can be developed by considering the possible physical processes that can occur. Considering the system is deliberately under a resonant condition, the atom can absorb a photon from the cavity field, and be excited from its ground state to its excited state, and is described by the $|e\rangle \langle g| \hat{a}$ operation. Equally, the reverse process can occur where the atom emits a photon into the cavity field and drops from its excited state down to the ground state, described by the $\hat{a}^\dagger |g\rangle \langle e|$ operation. The interaction Hamiltonian then looks like[37]

$$\hat{H}_{\text{interaction}} = \hbar g(|e\rangle \langle g| \hat{a} + \hat{a}^\dagger |g\rangle \langle e|) \tag{4.25}$$

where g is a coupling constant between the cavity field and the atom. The total Hamiltonian of the system, named the Jaynes-Cummings Hamiltonian[38] is thus given by

$$\hat{H}_{JC} = \hbar\omega_g |g\rangle \langle g| + \hbar\omega_e |e\rangle \langle e| + (\hat{a}^\dagger \hat{a} + \frac{1}{2})\hbar\omega + \hbar g(|e\rangle \langle g| \hat{a} + \hat{a}^\dagger |g\rangle \langle e|) \tag{4.26}$$

and the coupling constant g is given for a TEM_{ij} mode of the cavity with the cross section of the atomic interaction:

$$g = \sqrt{\frac{\mu_{ge}^2 \omega}{2\hbar\epsilon_0 V}} \Psi_{ij} \tag{4.27}$$

where μ_{ge} is the dipole matrix element of the atomic transition, and V is the volume of the cavity mode at the atom's location.

4.5 Cavity-Coupling Regimes

The previous section describes a cavity-atom coupled system in the absence of any losses. However, the stationary state of the excited atom does have a finite lifetime as it couples to the infinite-continuum of modes of the vacuum field, leading to spontaneous emission outside of the cavity, at a rate of Γ. Additionally, the lifetime of the photon with the cavity has a finite lifetime, as discussed in secton 4.16, given by the decay rate defined by the mirror qualities. The ratio of these rates defines whether the cavity is said to be in the 'strong,' 'bad,' or 'weak' coupling regimes.

In the 'strong coupling' regime, $g \gg \kappa, \Gamma$, meaning that photon emission into the cavity and re-absorption from the cavity is fully coherent. This coherent energy exchange between atom and cavity manifests as the Vacuum Rabi oscillation. This oscillation occurs at the Rabi frequency of the atom-cavity system, defined as $\Omega_C = 2g\sqrt{n+1}$. After an average time of $2\pi/\kappa$ the photon will be transmitted through the cavity mirrors and into the surrouning environment - *but crucially along the cavity axis.* This enables guiding of the emitted photon into a trap of similar design, where the reversibility of the first system is reproduced. Two systems communicating in this way form the basis of a distributed quantum network.[9] The rigorous definition of the strong coupling regime is given by $C>1$, where C is called the cooperativity, given by

$$C = \frac{g^2}{\kappa\Gamma}. \tag{4.28}$$

In the 'bad cavity' regime, the decay rate of the photon out of the cavity is greater than the cavity coupling and spontaneous decay rates, $\kappa \gg g \gg \Gamma$ which dampening any Rabi oscillation between cavity and atom, and no Rabi splitting is observable. However, since the photon emission is still highly directional due to the high cavity coupling factor, this condition has applications in cavity-induced enhancement of spontaneous emission using the Purcell effect[44].

Finally, in the 'weak' regime, the cavity coupling factor is less than both the spontaneous decay rate and cavity decay rate, $g \ll \kappa, \Gamma$.

To fulfill the criteria of the strong regime, for a given atomic transition with spontaneous decay rate Γ, the constraints are only on the quality of the mirrors and cavity parameters. The decay rate can be reduced by application of a high quality coating to the mirror surfaces to increase reflectivity and reduce losses. From equation 4.27, the cavity coupling factor is inversely proportional to the cavity mode volume, so decreasing the cavity mode by adjusting the cavity geometry is a route to improve g. Finally, the number of ions, N, increases the coupling to the cavity by a factor of $\sqrt{N}$. Strong coupling has been achieved experimentally with neutral atoms,[45] but not yet with ionised atoms.

4.6 Cavity-Coupling Simulations

The requirements for a strongly coupled atom-cavity interaction are detailed in the previous section 4.5. Using an atomic ion qubit of$^{40}Ca^{+}$, the $4P_{1/2} \rightarrow 3D_{3/2}$ transition is used for the cavity interaction, and while the spontaneous decay rate of this transition is 1.7MHz, the $4P_{1/2}$

level also decays rapidly to the $4S_{1/2}$ ground state at 20.6MHz, as shown in figure 4.5. This immediately imposes a limit that for strong coupling in this system, $g \gg 20.6\text{MHz}$, assuming a perfectly positioned ion with the maximum intensity of the TEM_{00} mode. As stated, the coupling

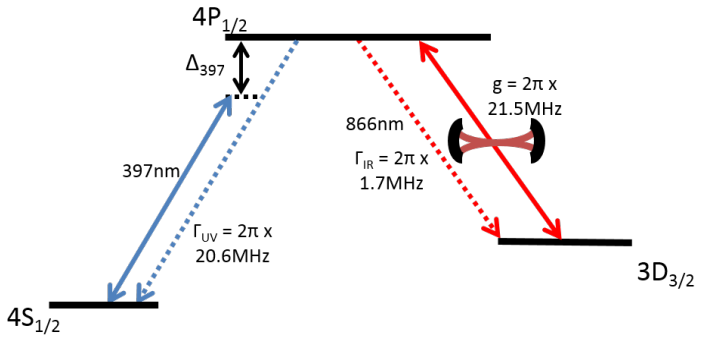

Figure 4.5: Illustration of the intended atom-cavity interaction scheme. The $4P_{1/2} \rightarrow 3D_{3/2}$ transition marked g is into the cavity, while the decays into the $3\text{D}_{3/2}$ marked Γ_{IR} and $4\text{S}_{1/2} marked \Gamma_{UV}$ indicate spontaneous emission into free space. The 397nm transition is used for cooling.

factor depends on the volume of the cavity mode. The cavity volume is

$$V = \frac{\pi}{2} L_c w_0^2 \tag{4.29}$$

where the waist is defined by the cavity length and mirror curvatures, given in terms of g_1 and g_2 here:[40]

$$w_0 = \sqrt{\frac{L_c \lambda}{\pi}} \sqrt{\frac{g_1 g_2 (1 - g_1 g_2)}{(g_1 + g_2 - 2 g_1 g_2)^2}} \tag{4.30}$$

Written in terms of the spontaneous decay rate, Γ_{IR}, the coupling factor becomes[41]

$$g = \sqrt{\frac{3c\lambda_{IR}^2\Gamma_{IR}}{8\pi L_c w^2}} \tag{4.31}$$

Commercially available mirrors typically have a minimum curvature of 5-10mm. Figure 4.6 shows a graph of the coupling strength for an atom located at the minimum waist position of a symmetric cavity with 1cm radius of curvature mirrors, as the cavity length is extended. The maximum coupling is eviedently for very short cavity lengths. Unfortunately, this geometry is prohibited in ion-trap systems due to the perturbance of the trapping potential with the mirror surfaces so close to the trapping region. At the concentric condition, when $R_1 = R_2 = L/2$, at 2cm, and is 4.9MHz, however this is close to the edge of the stability region and difficult to align precisely at the point of maximum coupling. An 8mm cavity has been succesfully implemented with an ion trap in the weakly-coupling regime with $g = 2\pi \times 0.9$MHz[42] with 1cm mirrors. This can be improved by using highly curved mirrors in a short cavity, implemented by using the end-facets of optical fibers as the mirror surface, as discussed in the next section.

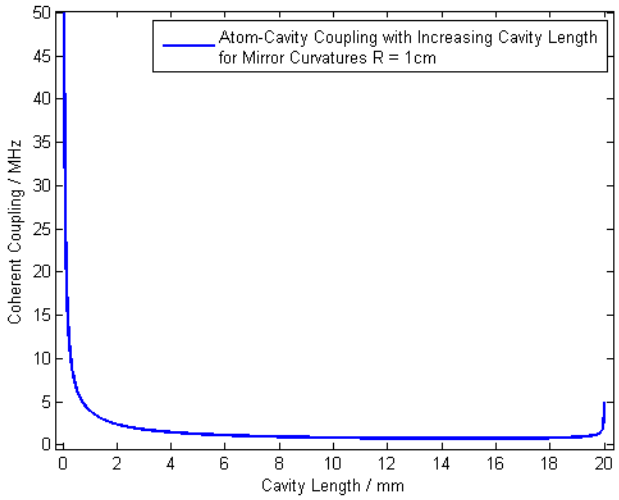

Figure 4.6: The change in coherent coupling between atom and cavity g, as the cavity length is extended for mirrors of a fixed curvature of 1cm. The highest coupling is in the very short cavity regime, which is not practical for integration for ion traps. The highest coupling achievable in an ion trap with these mirrors would be 4.9MHz at the limit of cavity stability at 2cm.

Chapter 5

Preparation of Fibres for use in Optical Cavities

Fibre-based Fabry-Perot Cavities (FFPCs) are of increasing interest for cavity QED experiments for their potential to create high finesse cavities with a small mode volume. Use of a CO_2 laser to machine the facet of the fibre creates a low roughness surface, capable of reaching finesses in excess of 100,000 [20]. In previous studies, fibres were machined from a single ablation pulse[20][62][63] producing concave structures with an elliptical shape. This can lead to FFPCs exhibiting birefringence[20] which inhibits their usage in applications where superpositions of light polarizations are exploited[64][65]. Furthermore, high intensity single-pulse ablation usually produces structures with a small radius of curvature and a small indentation which limits the cavity length due to clipping losses at the edge of the indentation. Even though in many applications short cavities are advantageous, in

some cases cavities with a length of several hundreds of mm are required. Among these applications is the coupling of atomic ions to a fiber cavity[14]. Due to the strong disturbance of the trapping electric potential by the presence of the fibers, trapping of ions in the close vicinity of a fiber mirror is challenging and hence relatively long cavity lengths are desirable. Unfortunately the small indentations created by single-pulse ablation limit the stability region of the cavity. In order to extend the cavity stability, we implemented a novel technique of CO_2 laser machining which involves applying a series of CO_2 laser pulses while rotating the fibre facet in order to produce a larger diameter mirror surface with good symmetry. We have used this method to produce and test fibre mirrors with a range of radii of curvatures from 100μm to 700μm, with cavity finesses of 40,000-60,000 over a large cavity length range. The fibres we use are Oxford Electronics HPSIR 200CB and IVG fibre Cu800-200[66]. Their core and cladding diameters are 200 and 214μm for multimode fibres respectively, and 6 and 200μm for singlemode fibres. All the fibres are coated with a copper layer of 34μm for multimode or 25μm for singlemode.

5.1 Optical Setup

To shape the end facet of an optical fibre by thermal ablation, we employ a CO_2 laser[1] in quasi-continuous wave operation. A schematic of the optical setup is shown in figure 5.1. The Polarisation Dependant Mirror (PDM) and Quarter-Wave Retarder (QWR) work together as an

[1]SYNRAD 48-1 Water Cooled 10W

optical isolator to protect the laser[2]. Lens L1 focuses the beam onto a mechanical shutter which is used to control the machining pulses. The rise and fall time of the shutter is approximately 1ms. When the pulse is 'off' the shutter is closed and the beam is redirected to a beam dump where the power is measured. Lens L2 forms a telescopic lens setup with L1 and is mounted on a linear stage to adjust the expansion of the beam. Lens L3 focuses the beam onto the fibre facet. This final lens is mounted using a magnetically coupled kinematic base[3], allowing routine interchangeability with other optics without causing disturbance to the beam alignment.

[2]The laser output is vertically polarised, which is reflected by the PDM, while horizontal polarisation is absorbed. The Quarter Wave Retarder (QWR) then circularly polarises the light. Any backscatter is polarisation shifted again, now to horizontal polarisation. This is then absorbed by the PDM, preventing backscatter from harming the laser.

[3]Available from Thorlabs, part number KB1X1

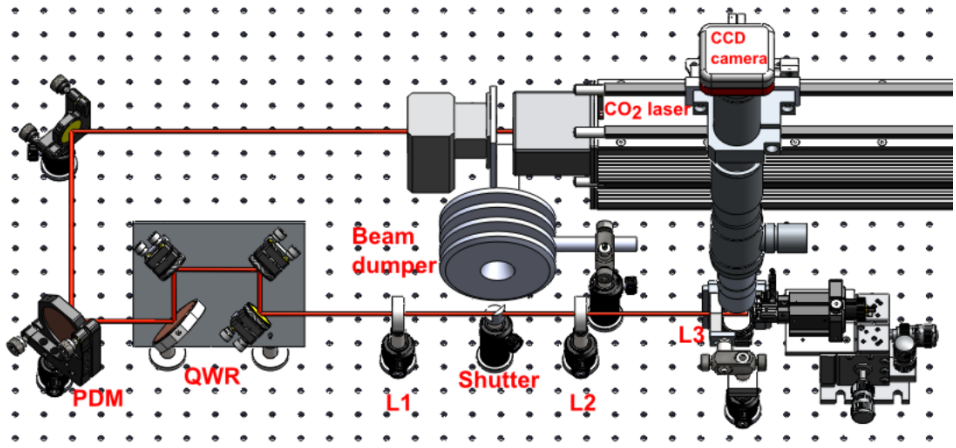

Figure 5.1: Schematic of the optical setup for CO_2 laser machining, the red line represents the path of the CO_2 beam for an open shutter. The Polarisation Dependant Mirror (PDM) and Quarter Wave Retarder (QWR) act as an optical isolator as explained in the text. L1 and L2 are lenses forming a telescopic setup with the minimum waist located at the shutter. L2 can be translated along the beam axis to alter the spot size of the machining pulse, which is focused onto the fibre by lens L3.

A vertically mounted microscope is employed to analyse the fiber surface. Replacing the magnetically mounted lens with a 45-degree angled mirror enables basic optical inspection, and a beam splitter cube facilitates a more detailed view by white light interferometry. In this way it is possible to assess the quality of a machined surface in situ and continue with laser machining until the desired surface parameters are reached.

The fibre is clamped in a v-groove as part of a rotation stage[4], the rotation of which is controlled by a stepper motor to provide reproducible rotation. In order to align the position of the mounted fiber

[4]Newport 466A-717

with the laser beam, the rotation stage is mounted on a 3-axis linear translation stage. Due to imperfection in matching the two axes of the fiber rotor and laser beam, the fiber precesses around the beam by a small amount as it is rotated. This precession can be reduced to a radius of approximately 10μm by careful alignment, but this still has a non-negligible impact on the surface symmetry. As such, we realigned the fibres with the microscope after every rotation.

5.1.1 Machining Laser Alignment

To align the fibre to the laser focus, we first make some test pulses aimed at a window mounted in the fibre rotator. We then use the 45-degree angled mirror to inspect the window surface, and move the microscope to focus on the position of the resultant crater. By doing this, the microscope and machining laser focii are overlapped. Placing the fibre into the rotator and moving it into the microscope focus, now ensures the machining laser's focus is aligned with the fiber facet.

5.2 Machining Process

The fibre is placed into the v-groove of the fibre rotator and held in position by magnetic clamps. The laser is then pulsed off with a q-switch while the mechanical shutter opens. The laser is then turned back on for the duration of the machining pulse, and the q-switch used to switch it off while the mechnical shutter closes. The pulse length can be adjusted to millisecond precision. Laser parameters such as intensity, beam waist and the duration of the pulse all contribute to

the thermal ablation process. The shape is monitored after each pulse by optical inspection, and the fibre rotated after every pulse by a a 45° angle to maintain good rotational symmetry regardless of beam shape. Figure 5.2 shows how these techniques have a large impact on the resulting surface structure, with figure 5.2b depicting an ideal machined surface.

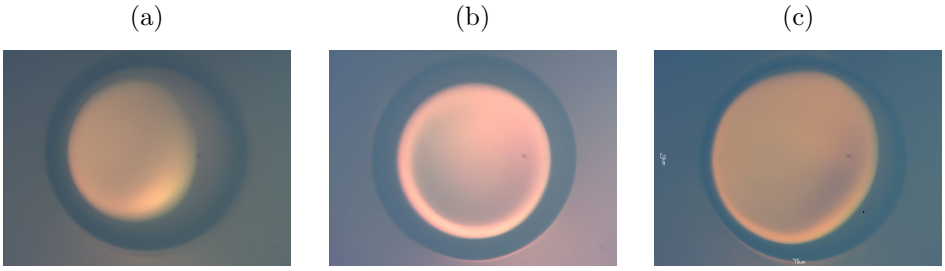

Figure 5.2: Comparison of three separate fiber machining techniques. **a** Produced by one laser pulse with beam waist 107μm at 1.2W laser power for a 2s pulse. The long pulse length has ablated too much of the fiber for it to be useful. **b** Produced by 44 laser pulses at 2.0W, with a beam waist of 116μm and duration of 65ms. The fiber is rotated after every shot by 45°. **c** Produced by 200 laser pulses at 2.0W with a duration of 60ms and beam waist of 102μm. This fiber was not rotated between pulses, and has a clear asymmetry as a result.

Typical laser parameters for machining a curved fibre are a power of 2.0W with a 50-80ms long pulse and a beam waist of 100-120μm. In addition to fibres with with curved surfaces, we have produced fibres with flat surfaces by applying 3-10 pulses with a large beam waist of approximately 120μm. These pulses are usually enough to polish the fibre facet of the microfractures present on the surface after a cleave without curving the surface of the fibre. The output light field from an optical fibre is divergent, and since there is no method with these fibres

for mode matching the input light field to the cavity field, there is poor coupling efficiency at longer cavity lengths for plane-parallel, concentric and confocal cavities. Flat fibre facets are of interest for constructing a cavity in the hemispherical regime between a single mode input fibre and multimode output fibre. The hemispherical regime is the only cavity with the potential for high mode matching effeciency at long cavity lengths due to the intrinsic matching of the divergence of the output singlemode fibre to a hemispherical cavity mode.

5.3 Surface Inspection by Interferometry

We use white light interferometry to measure the curvature of a machined fiber with respect to a flat reference plate. For this we employ the magnetic mount described in 5.1. We place a beam splitter cube on the magnetic mount, and introduce the white light from a halogen lamp along the same direction as the laser by inserting an extra mirror on the beam path while blocking the laser, as shown in figure 5.3. The white light source is introduced using a halogen lamp along the laser axis while the laser is blocked. The produced interference pattern provides insight into the surface shape, as shown in figure 5.4b. The interference pattern is analyzed by a MATLAB program inspects the number of interference fringes to calculate the radius of curvature and reconstruct the 3-dimensional fibre surface. The central region of the indentation is well approximated by a Gaussian profile as shown in 5.4c. The diameter of the depression defined by the full width (1/e) of the Gaussian fit is 137μm. Due to the rotation of the fibre during

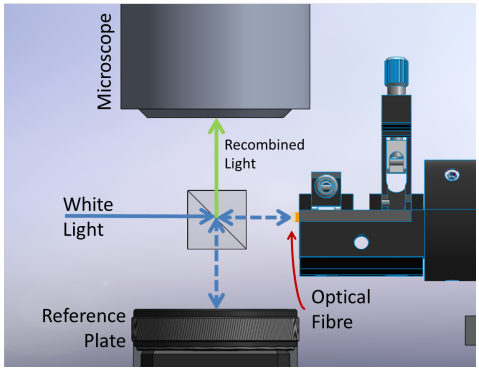

Figure 5.3: Interferometry setup for detailed inspection of a machined fibre.

machining, the surface symmetry around the center shown in figure 5.4c has an ellipticity of less than 2%.

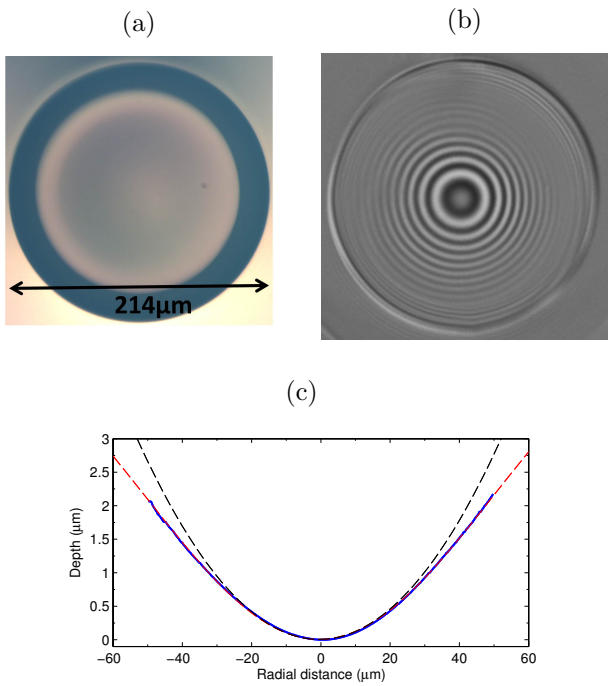

Figure 5.4: **a** An optical image of a curved fiber. **b** Interference image of the same curved fiber using white light interferometry. Here only the red layer of the color image is extracted and presented in black and white.**c** A reconstructed cross section of the curved fiber obtained from the inteference image, b. The blue curve is the experimentally reconstructed fiber surface. The red dashed curve is a fit with the Gaussian function. The black dashed curve is a circle having the same local radius of curvature (457.4 μm) at the bottom.

5.4 Finesse Measurements Using Prepared Fibres

After a batch of 48 fibres were machined, they were sent to be coated with a high reflective coating by AT-Films[5] The coating is at maximum reflectivity at 866nm, with approximately 30ppm transmission.

[5] Advanced Thin Films, 5733 Central Avenue Boulder, Colorado USA

Two fibres are placed face-to-face to form the cavity as shown in figure 5.5a and 866nm light is transmitted through the input fibre, while the other (output) fibre is connected to an avalance photodector (APD). The cavity length is then scanned to find a resonance using a piezoelectric actuator. An example of a cavity resonance is shown in 5.5b, and the accompanying sidebands are a result of a modulation applied to the laser to provide a frequency reference. The frequency modulation we use to measure the FWHM of the cavity resonance, which in turn can be used with the cavity length, L_c to calculate the finesse, using

$$\mathcal{F} = \frac{c}{2L_c\Delta}, \tag{5.1}$$

where Δ is the cavity linewidth. The finesse is also related to the transmissivity of the cavity mirrors, T and absorption and scattering losses, L by

$$\mathcal{F} = \frac{2\pi}{T + L}, \tag{5.2}$$

which is related to the cavity decay rate by equation 4.17 as discussed in section 4.3, and hence a high finesse is needed to be in the strong coupling regime.

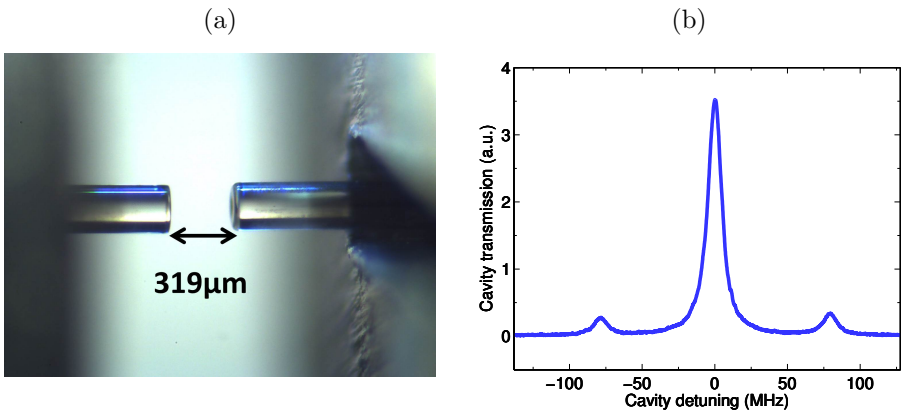

Figure 5.5: **a** Microscope photo of a fiber cavity. **b** Transmission signal as the fiber cavity is scanned over resonance. The x-axis is calibrated to a detuned frequency with respect to the center of resonance by using the side band peaks at ±79 MHz.

The behaviour of the cavity finesse over increasing cavity length has been investigated. Firstly, the cavity finesse was found to fall sharply after a certain cavity length was reached [62]. This cutoff point was found to be explained well by the clipping loss model which assumes that on each reflection, a small fraction of the initial intensity is lost as it falls outside of the spherical mirror surface and subsequently out of the cavity. The fractional loss, L_{clip} is given by[62]

$$L_{\text{clip}} = 1 - \frac{\int_0^{r}{}_{\text{clip}} I(r) r dr}{\int_0^{\infty} I(r) r dr}$$

$$= \exp(\text{-}2\text{r}_{\text{clip}}^2/w^2),$$

where I(r) is the intensity distribution of the cavity mode on the mirror as a function of the radial distance r and w is the mode waist on the mirror. Equation 5.4 assumes the cavity mode is the Gaussian TEM_{00} for spherical mirror cavities. From figure 5.4c we know this is a close approximation for our mirrors over small radii. The results for our cavities depend on the type of fibre mirrors used, differing greatly between a multimode-multimode pairing (MM-MM), singlemode-multimode (SM-MM) or singlemode-singlemode (SM-SM). Figure 5.6 shows a sample of finesse measurements made for MM-MM cavities, which fit well tp the clipping loss model. The large error bars are mostly due to the fluctuation of the observed resonance peak as the input light travels through a multimode fibre. From the fit, we have found that there is a residual 35ppm loss per mirror, possibly caused by imperfections in the reflective coating, perhaps reducible by annealing the fibres in oxygen[20].

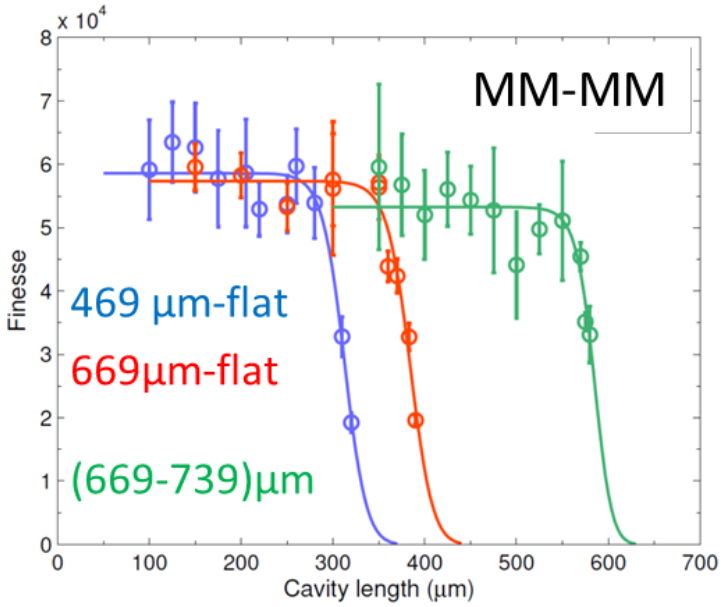

Figure 5.6: Finesse measurements for three different optical cavities using different pairs of fibres.[68] The solid line is fit according to the clipping loss model. The inset numbers refer to radius of curvature of the cavity mirrors.

Figure 5.7 shows the finesse measurements for SM-MM and SM-SM cavities. Here, the singlemode fibre cavity finesses decrease at a shorter length, but the finesse degrades at a reduced rate compared to the clipping loss model, as such the fitted line is only for eye-guiding. While finesses are only slightly less than those measured in the multi-mode cavities, the cavity length for which it is stable is generally much shorter.

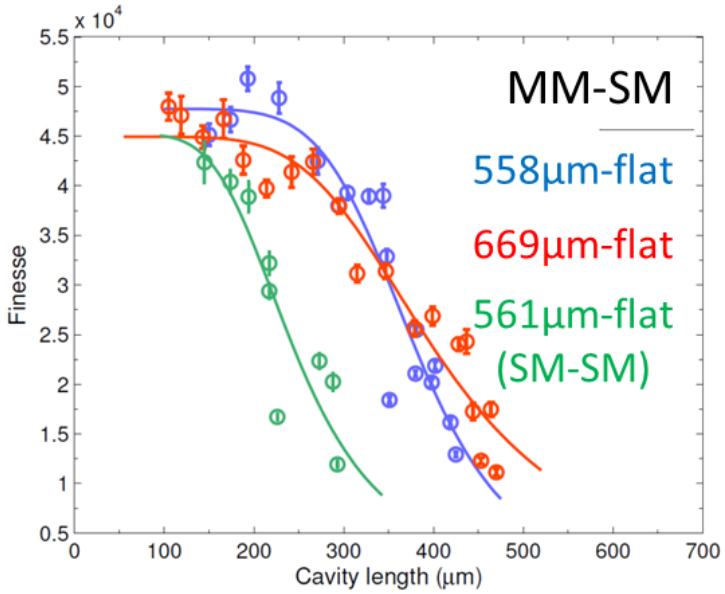

Figure 5.7: Finesse measurements for three different optical cavities using different pairs of singlemode and multimode fibres. The solid line does not accord to any model[68].

The internal structure of an optical fibre consists of the core, which transmits the light, and the cladding which is a protecting layer around the core. For a multimode fibre, the step-index core is large in radius, with a thin cladding layer. On the other hand a singlemode fibre has a narrow core, and a thick cladding. For our MM fibres the core is 200μm in diameter, while in SM fibres it is 6μm. While machining with the CO_2 laser, the core of the singlemode fibre becomes very visible, and appears to form a ridge around its edge, as shown in figures 5.8a and 5.8b.

(a)

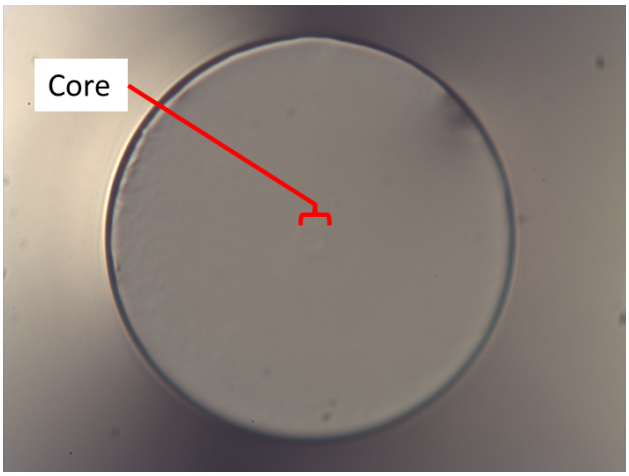

(b)

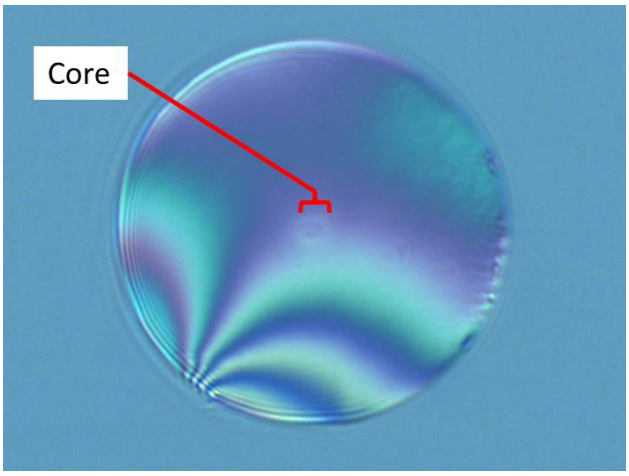

Figure 5.8: (**a**) Optical image of a partially machined single mode fibre. The core is visible at the centre as a circle surrunded by a ridge structure. (**b**) Image of the same fibre produced by interference, showing the core ridge more clearly.

This ridge is a large defect in the center of the fibre mirror, and is likely to be at least part of the cause of the reduced finesse and stability

of the cavities with singlemode fibres. We found machining parameters for which the ridge seemed to be removed, which were with a power of 2.0W at a waist of 137$\pm$2μm with an average pulse length of 56$\pm$1ms for 3-5 pulses. Optically, and using the interference imaging setup, it appeared that the ridge was removed.

We have since used an atomic force microscope (AFM)[6] to check with higher resolution, and in recent results it appears that the core ridge is not entirely gone, but deeply suppressed, having a height of around 10nm remaining, the images of which are shown in figures 5.9a,5.9b and 5.9c.

[6]Burleigh Aris 300 personal Atomic Force Mircoscope

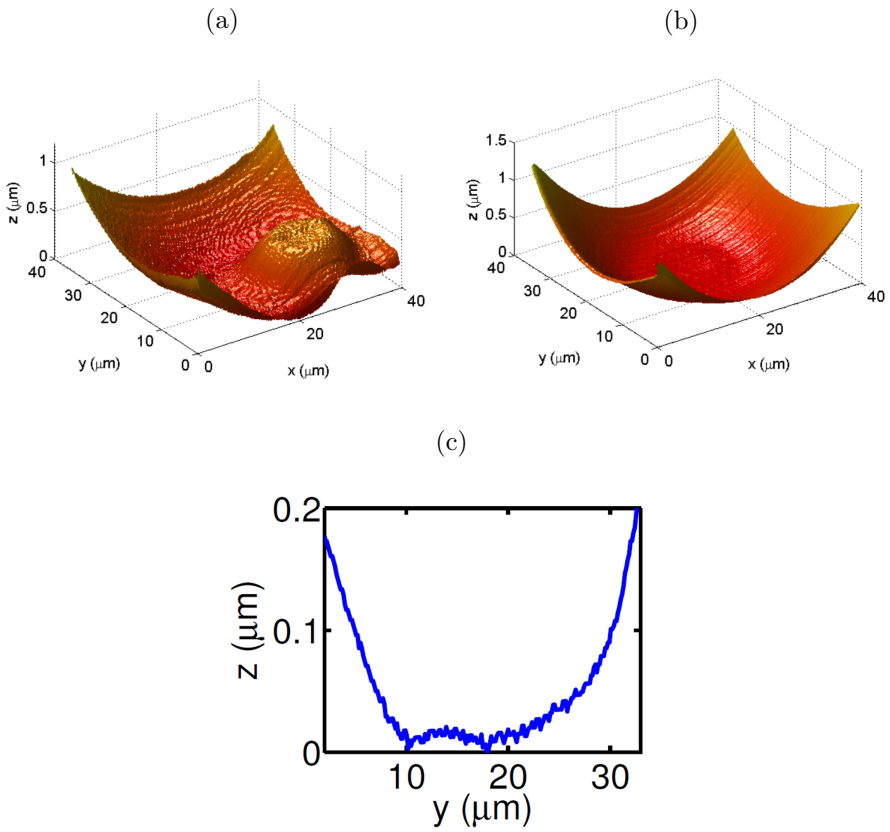

Figure 5.9: (**a**) AFM image of the central 37.5μm The ridge is visible to the right. (**b**) AFM image ofthe fibre after an attempt to the remove the core ridge with further laser pulses. Here the ridge appears almost totally removed. (**c**) Detailed cross section of figure (b) across the y-axis at x = 20μm that shows a slightly raised section at the center of approximately 10nm.

The emergence consistently seems to be interface of the core and cladding materials with slightly differing thermal properties. This behaviour is also visible in results found when attempting to machine polarisation maintaining fibres, which show pronounced ridges around the stress-rods which run down the fibre, in addition to showing deep

curvature within the stress rods, while no general curvature of the fibre, as shown in figure 5.10.

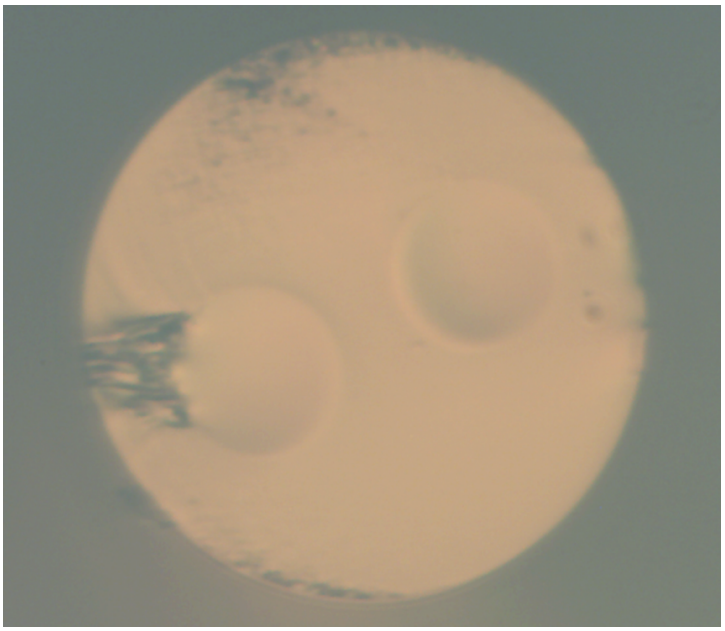

Figure 5.10: Result of an attempted machining of a polarisation maintaining fibre. The laser is focused at the centre with a beam waist of approximately 100μm. The outcome structure appears to be as a result of higher thermal ablation rates of the fibre stress rods than the rest of the fibre core and cladding.

5.5 Birefringence

As mentioned at the beginning of section 5, previous studies have found a significant birefringence in the resonance of the cavity mode[20][62]. We measured the dependance of the cavity linewidth on the input polarization using the fundamental cavity mode of a MM-SM cavity with radius of curvature of 558μm for the multimode, and a flat singlemode

at 270μm (fig 5.11a). Since the input fibre is a flat singlemode, the mode matching between the input mode and the cavity TEM_{00} is expected to be dominant and it is reasonable to assume the largest peak in scan 5.11b corresponds to the TEM_{00} mode. There is no apparent splitting of the resonance peaks of the cavity's fundamental mode(Figure 5.11c) or higher order modes(Figure 5.11d) which would otherwise suggest birefringence.

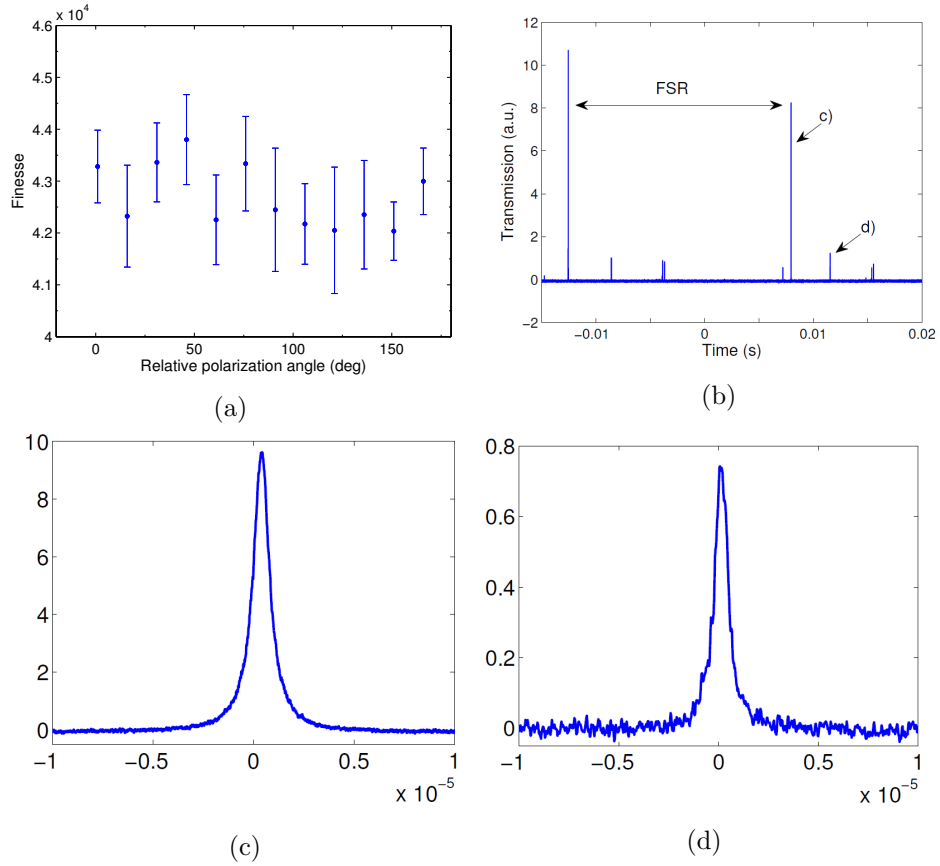

Figure 5.11: (**a**)Polarization dependence of the linewidth (measured FWHM). The error bars represent one standard deviation. (**b**) A typical transmisson profile of the cavity when as its length is scanned over time. (**c**),(**d**) Close-up views of the scan profile for the fundamental and next higher mode respectively, a indicated in b

To obtain an upper limit for the variation of the cavity linewidth due to the input polarization, we take the difference between the highest and lowest points within the error bars in figure 5.11a. This corresponds to a change of the linewidth of 1.16MHz, with the mean value being 13.0MHz [19]. In order to reproduce this change of linewidth solely by a splitting of the polarization modes, the splitting in frequency needs

to be 3.84MHz. This was determined by fitting a single Lorentzian function fo a simulated double-peaked Lorentzian profile with a given peak sepration. Note that this value is an overestimation of the bire-finrgence as the errors in 5.11a also include the technical and statistical noise in the measurements. The frequency splitting of the orthogonal polarization modes in an elliptical mirror cavity is given by[67]

$$\Delta\nu = \frac{\lambda\nu}{\mathrm{FSR}(2\pi)^2}\frac{R_i - R_j}{R_i R_j}, \tag{5.3}$$

where R_i and R_j are the radii of curvature along the principal axes to get the elliptic paraboloidal shape of the surface. Using the mirror parameters from 5.11a we obtain $\Delta\nu = 2.36$MHz which is close to the aforementioned value and significantly below the cavity linewidth.

Chapter 6

Microtrap Design

This chaper describes the requirements and considerations in order to achieve a system in which there exists strong coupling between an atomic stationary qubit and a photonic flying qubit.

6.1 Trap Geometry

6.1.1 Trap-Cavity Alignment

By incorporating a cavity into an ion trap, one must find a way to accomodate it without adversely affecting the capability of the trap to hold ions. There are broadly two ways in which to do this, by aligning the cavity collinear to the trap axis, or by having the cavity aligned radially, perpendicular to the trap axis.

Due to the relatively large distance between adjacent ions within an ion trap, in the perpendicular case, less ions are well overlapped with the cavity field. Assuming the cavity field is Gaussian around the point

of minimum waist, and that the waist minimum is directly overlapped with the ions, the coherent coupling to the light field is

$$g(r) = g_0 e^{-2^2/w_0^2}. \tag{6.1}$$

For the perpendicular case, two issues are apparent. The inter-ion separation within the trap reduces the number of ions available to couple to the cavity mode. Typical estimations for inter-ion spacing is around 5μm. Furthermore, due to the Gaussian shape of the field, only two ions will ever be available to couple equally, which is a necessity for ensuring the atomic qubits remain identical, as shown in figure 6.1. If spaced symmetrically around the beam centre, the expected coupling is 91% of the maximum coupling g_0 at the center of the mode.

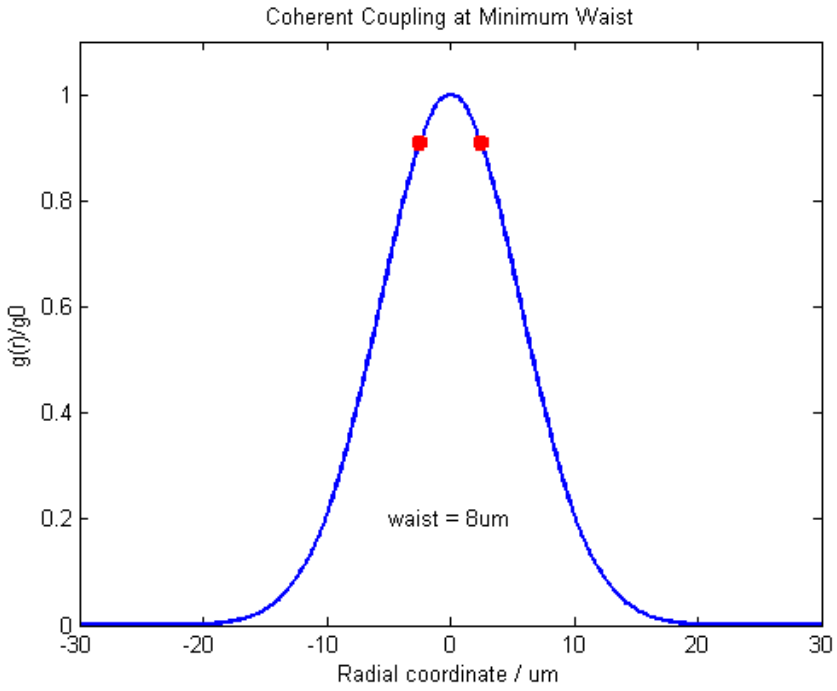

Figure 6.1: Coherent coupling to a cavity field for a minimum expected cavity waist of 8μm. The two red marks indicate idealised positions of two ions for equal coupling to the cavity mode.

For the collinear case, the number of ions that can couple to the cavity field is limited by the length of the trap (and thus number of ions present within the string), and the divergence of the cavity waist. As seen from the measurements taken in section 5, the fibre cavity can be no longer than 300-400μm before the cavity mode loses stability. This constrains the length of the trap significantly, but not to an insurmountable degree. For 866nm light focused to a waist of 8μm, the Rayleigh range of the field is 230μm, much longer than the expected trapping region. Figure 6.2 shows how the coherent coupling decreases through a 300μm long region. Below the red dashed line in figure 6.2

has less than 10% deviation from the maximum coupling strength, for a perfect trap. A single pair of ions coupled around the cavity center would experience a coupling difference of less than 0.16%,an improvement of two orders of magnitude on the perpendicular arrangement. However, the true coherent coupling value depends on the standing wave structure within the cavity [70].

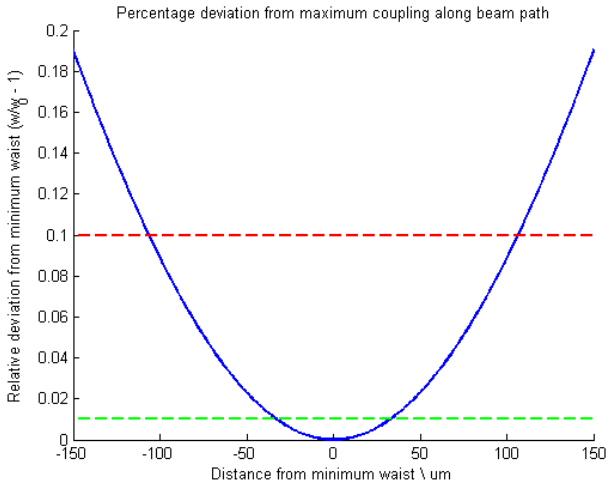

Figure 6.2: The relative deviation between the minimum waist. The red dashed line indicates the 10% deviation mark extending over 200μm. The green dashed line indicates the 1% deviation regime extending over 60μm.

6.1.2 Trap Size

Taking the decision to align the cavity along the trap axis now decides the overall size of the trap. As discussed in the previous sections on the stability and coupling strengths of fibre Fabry-Pérot cavities, (in 5) the total length of the trap along its axis must be sub-millimeter in scale. To stably trap an ion string in a linear trap, the trap length must be much larger than the radial electrode distance. Previous succesful

designs featuring a cavity or other optic along the trap axis [41], [59] house the optical surfaces within the axial electrodes at the end of the trap supplying the DC trapping potential. An example of an existing, larger system is shown in figure 6.3. Despite the difference in scale, a comparable mounting structure is achieveable using stainless steel needles. There are steel tubings commercially available[1] with a 300μm inner diameter and 450μm outer diameter which can house the fibres.

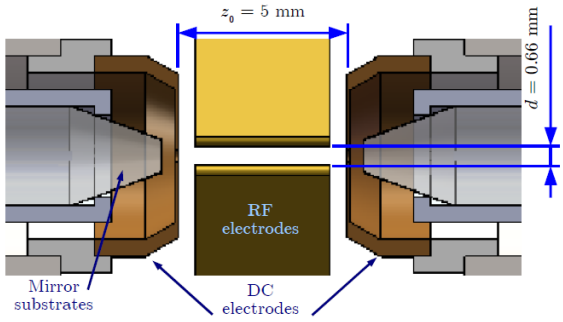

Figure 6.3: Solidworks model of the cavity-trap from [69] used in [70]

The close proximity of the RF-electrodes requires them to deviate from the ideal hyperbolic shape. A pointed, blade-like shape can produce a trapping potential around the central region between the electrodes, which is adequate for the case of well localised, laser cooled ions. The trapping potential is sensitive to the the tips of the blades, which must be very sharp and free from deformations. This leads to two approaches to this design, a 'sandwich' styled trap where the blades are in parallel pairs or a cross-shaped design where the blades are angled. Consider that line-of-sight access is required for the trapping and

[1] Coopers Needle Works Limited, 261 - 265 Aston Lane, Birmingham, West Midlands, B20 3HS, England, +44 (0)121 356 4719

ionisation lasers, as well as for optical inspection with a camera and PMT, and finally a path available for the atomic Calcium beam to feed into the trap. Since the trap axis is accomodating the cavity, only the radial axes are left to accomodate these vital components. The sandwich trap design prohibits the optical access along the axis parallel to the trap electrodes - leaving only the side access. The angled electrode trap has the advantage of allowing optical access into the trap from all radial directions, easily accomodating each component. A potential-map of a bladed RF configuration is shown in figure 6.4a, produced by finite-element analysis. The plotted pseudo-potential is calculated from the magnitude of the electric field, using

$$\Phi_{\text{pseudo}} = \frac{e}{4m_{Ca}\Omega^2}|\vec{E}^2| \tag{6.2}$$

where e denotes the elementary charge, m_{Ca} is the mass of calcium-40 and Ω is the angular frequency of the driving RF field. An RF blade separation of 50μm with an RF driving frequency of 20MHz at 10V is estimated to produce a trap depth of 650meV. An RF electrode blade length of 300μm completes the geometry to form a linear Paul trapping field. A radial view of the pseudo-potential produced by the RF viewed is shown in figure 6.4b.

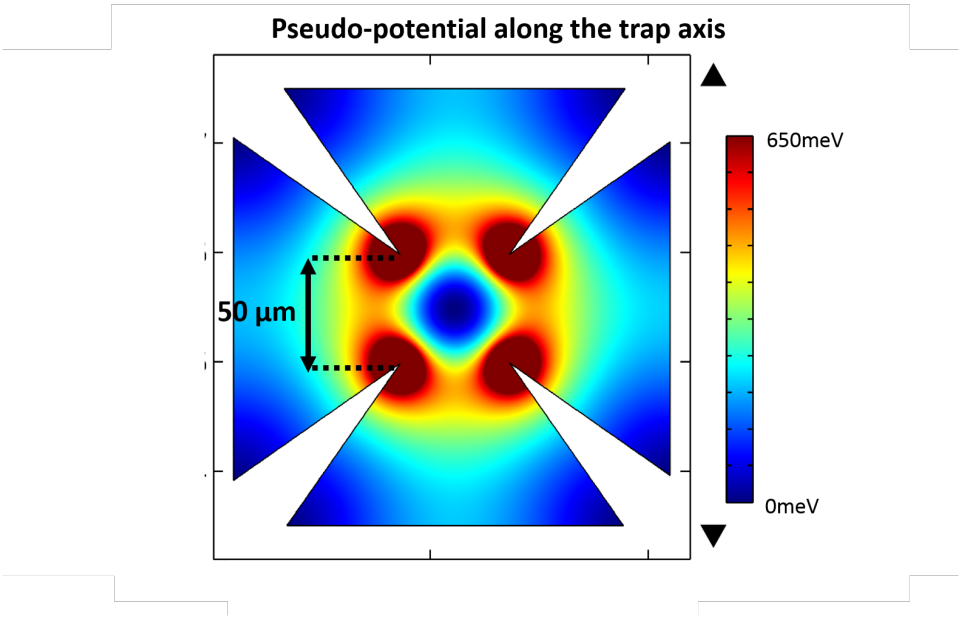

(a)

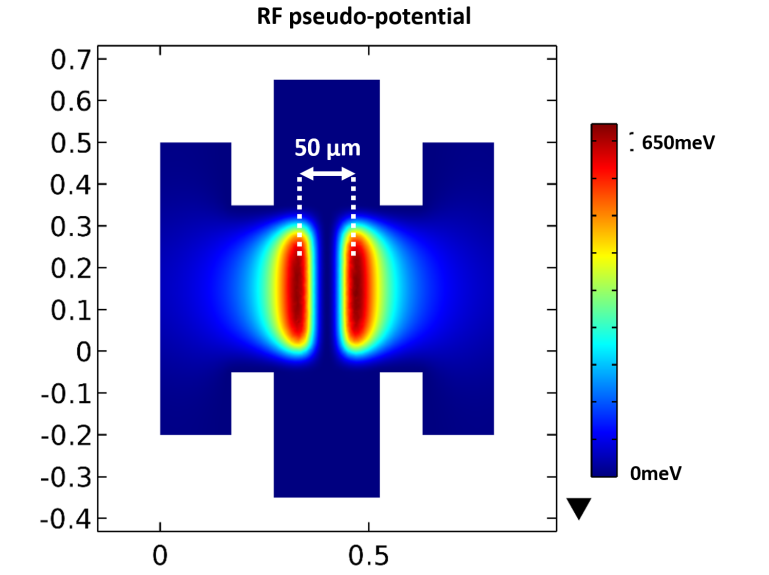

(b)

Figure 6.4: (**a**)RF pseudo-potential of the trap, viewed along trap axis. (**b**) RF pseudo-potential of the trap, viewed radially.

The simple geometry of this setup combined with the DC-electrodes is shown in figure 6.5.

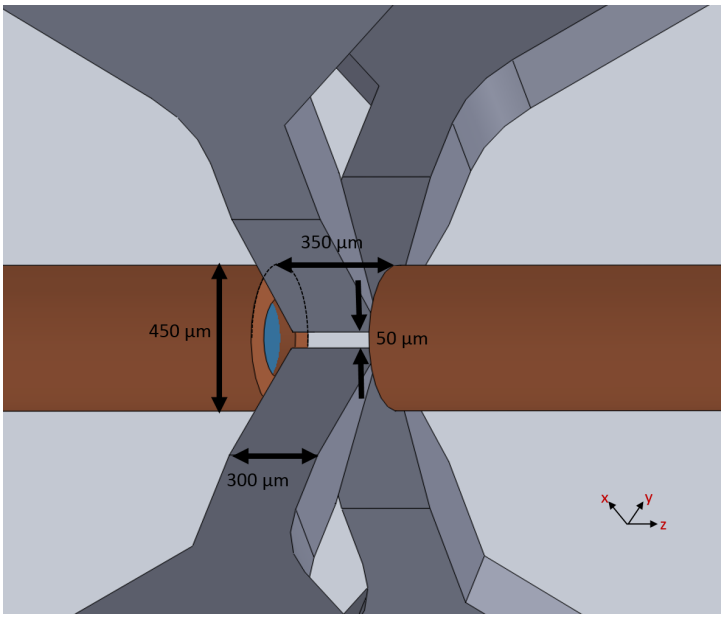

Figure 6.5: 3D drawing of the trapping region of the microtrap. The grey blades show the positioning of the rf-electrodes providing radial confinement in the XY plane. The copper-coloured cylinders along the z axis are the DC electrodes for axial confinement. The blue face within the electrode marks the location of one of the fibre mirrors while the other is hidden by the opposing DC electrode.

6.2 RF Structure

The rf-electrodes are mounted on two separate mounts, two on the upper and two on the lower. These are then bolted to a third holding side wall for support, as shown in figure 6.6a. This requires precision assembly to be a two step process, beginning with alignment of each

pair of electrodes on their respective mounts, followed by attachment to the side wall to align the pairs together. The side wall must be thick enough to flex a minimal amount.

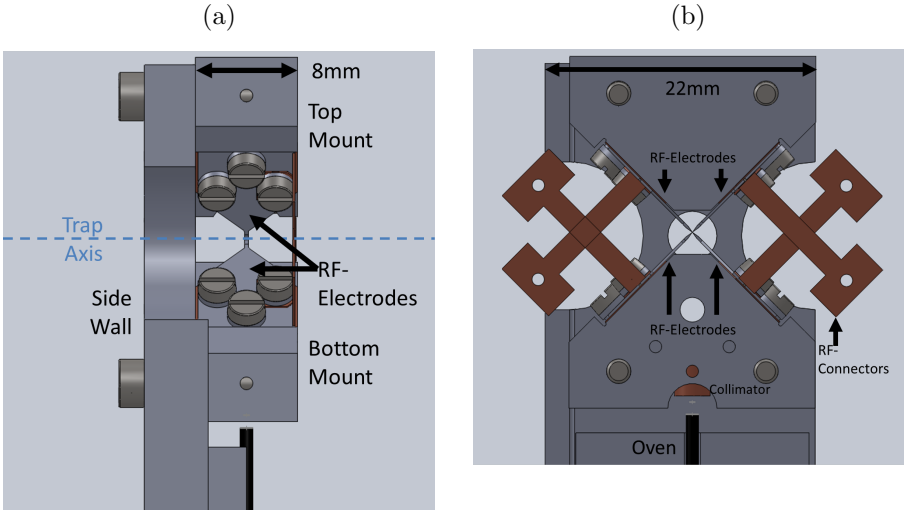

Figure 6.6: (**a**) Radial view of trapping structure. The dashed line indicates the trap axis along which the DC electrodes and cavity will be aligned. (**b**) View of trapping structure along the trap axis. The 4 rf-electrodes are isolated from the (grounded) trap structure as discussed in the text. Their power supply is connected via the copper-coloured rf-connectors labelled.

The trapping structure is kept grounded and isolated from the rf-electrodes by kapton sheets placed between them and the bottom or top mount to which they are attached. We use a small copper connector in electrical contact with the electrode (but shielded from the bolt screws using a ceramic washer) to connect the rf-power, as shown in figure 6.6b. The advantage of this is the risk of damaging or misaligning the rf-electrodes by soldering or spot welding is removed. The copper connector has enough flexibility to be moved away from the trap center

and laser line of sight.

6.3 Experimental Cavity

The benefits and limitations of fibre-based Fabry-Pérot cavities have been well discussed throughout this thesis. Our single-mode fibre cavities are unstable at cavity lengths longer than about 250μm, which is too short to utilise in an ion trap without perturbing the trapping potential. However, a combination of single-mode fibre for one mirror and multimode fibre for the other does enable longer cavities to be stable. A single mode fibre with radius of curvature 447μm and a multimode fibre with radius of curvature 490μm are to be used. The implementation of one of our singlemode fibres limits the finesse of a stable cavity to 33,000, as measured in figure 6.7a. The possible coupling over this stable cavity range is shown in figure 6.7b.

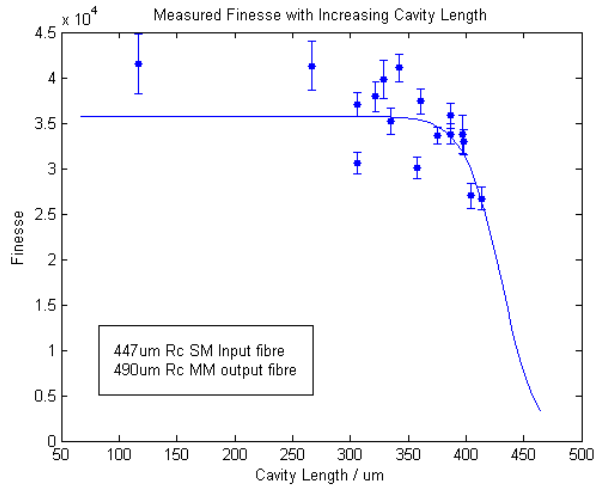

(a)

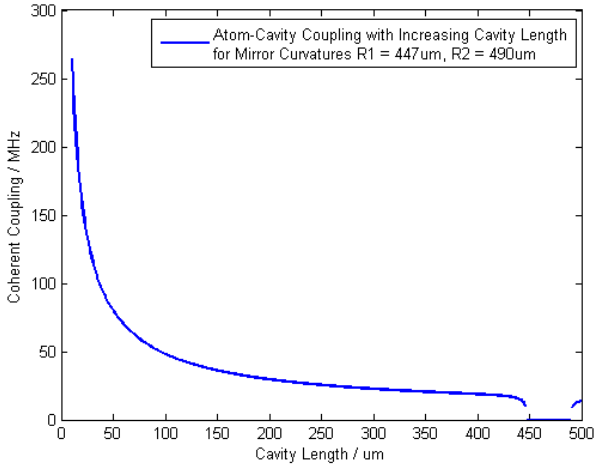

(b)

Figure 6.7: **(a)** Finesse of the experimental cavity fibres as the cavity length is increased. The fitted line is to the clipping loss model described in section 5.4 **(b)** Coherent coupling g, as cavity length is increased.

The cavity mirrors are to be recessed within the electrodes by 15μm on each side. This is to protect the mirror surface from degradation arising from the atomic beam, as well as protecting the trapping po-

tential from perturbations due to patch potentials arising from charges accumulating on the dielectric mirror surface [58][59][72]. Simulations using finite element modelling software suggest the trap depth is not directly improved by recessing the fibre, but do not account for charge accumulation [73]. Since the upper bound on the cavity length is defined by the edge of this cavity's stability with these mirrors of 380μm, the DC electrode distance is fixed to no more than 350μm apart. The expected coupling for a single ion to the 380μm cavity with this pair of mirrors is 2π x 19.4MHz and the cavity linewidth is expected to be 2π x 11.9MHz resulting in a single ion cooperativity of C=1.5.

6.3.1 Cavity Alignment

The testing setup described in section 5.4 for measuring the finesse of the test cavities formed with our machined fibres covers all degrees of freedom for cavity alignment. However, placing the same components into vacuum is not an acceptable plan of action - optical stages are not vacuum compatible, and quite large, not ideal for a vacuum chamber where optical access is important. While monolithic cavity mountings are possible with fiber-based cavities [71], they are only passively stabilised to a fixed cavity length. To adequately lock the cavity it requires active stabilisation via the means of a fast-response piezo. Since a monolithic design is prohibited, it also requires a mechanism to control the alignment in-situ in the event of misalignment which must be UHV compatible. We incorporate two means to do this, the first is in providing an aluminium flexure stage that can provide up to 300μm of motion for the coarse alignment, and is controlled via 4 grub screws,

two for each axis. One fibre is mounted atop this structure and has this travel range in both radial directions. The flexure stage is shown schematically in figure 6.8a and as part of the three-dimensional model in figure 6.8b. The second control method is for fine alignment, for which we use a further two piezos. These are long-travel piezo stacks, one for each axis. In total each has 10μm of travel along each axis. Importantly, these allow fine adjustments to the cavity alignment once the system is closed and in vacuum conditions, to protect against any loss of cavity signal due to small-scale misalignments, for instance from thermal expansion when activating the Calcium oven and from baking the system to reach UHV pressures. A solidworks drawing of the model is shown in figure 6.9.

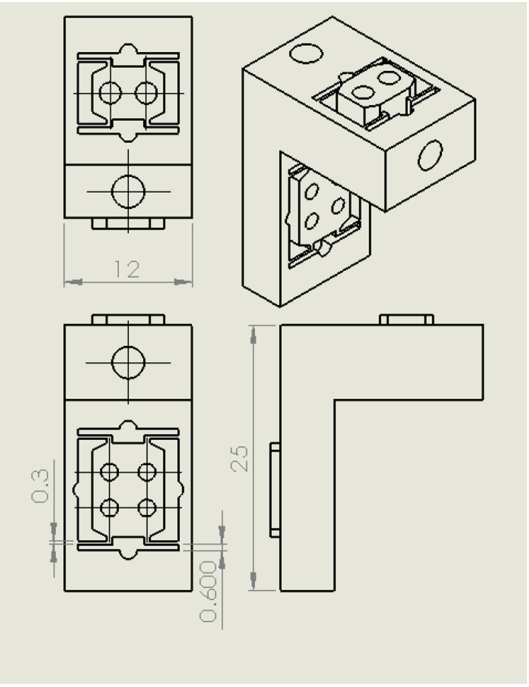

(a)

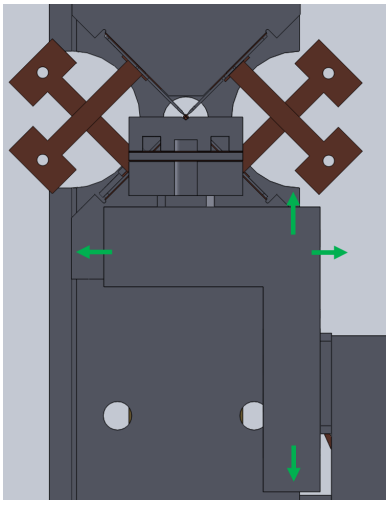

(b)

Figure 6.8: Figure 6.8a shows a schematic of the aluminium flexure stage used for coarse alignment of one of the cavity fibres. It was cut using wire erosion to remove the inner sections to leave the thin flexure arms of 0.3mm in width. Figure 6.8b shows the trap viewed along the trapping axis, where the flexure stage can be seen from the side. The green arrows mark where each motion occurs. Four fine-threaded M3 grub screws are cut to 4.5mm in length to adjust the motion, two per axis. The short length allows them to be almost entirely recessed within the stage structure.

Finally we need some control for overlapping the cavity mode maximally with the ion's location. In the existing larger ion-cavity designs, the trapping region is so large compared to the waist of the cavity field, that application of a DC-offset on the RF electrodes is sufficient to maximise the overlap between ion and cavity field. However in the case of this smaller system, the cavity field is on a similar size scale as

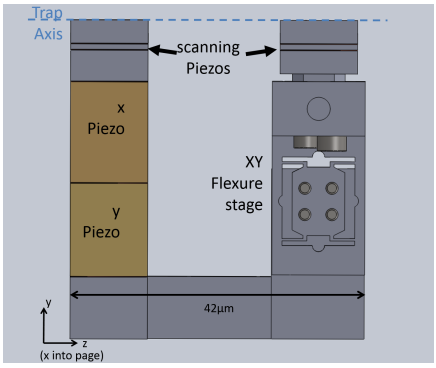

Figure 6.9: Radial view of the DC electrode mounting structure. The dashed line indicates the trapping axis. The radial electrode structure rests between the two DC electrode mounting blocks. The XY flexure stage allows coarse alignment within 300μm in the X and Y axes and XY piexos allow fine alignment within 10μm. The scanning piezos are for scanning the cavity length

the RF electrode separation[2] and so corrections to the position must be made by mechanically moving the cavity with respect to the RF electrodes. To achieve this we add a three-dimensional piezo stage to translate the RF electrode's position by 38μm in each direction to overlap in vacuum. The total RF and combined DC solidworks assembly is shown in figure 6.10

6.4 Vacuum System

While the trap setup is small at only $\sim$ 4cm across, the vacuum chamber must be significantly larger to accomodate the large bending radius of the fibres for long-term storage, which is 40mm. On the other hand,

[2]Recall the RF separation is 50μm and the minimum cavity diameter is approximately 8μm.

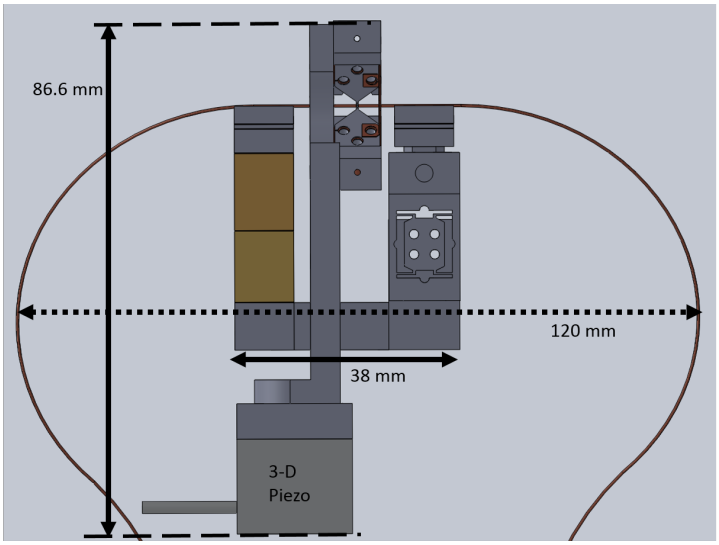

Figure 6.10: Radial view of RF and DC mounting structures together. They are not bolted directly to one another to allow relative motion of the RF electrodes to overlap the trapping potential with the cavity field through use of the 3-D piezo shown at the base.

in order to have a tight enough laser focus to pass through the centre of the trap, we require a lens close to the trap centre. To satisfy these conditions we have opted for a rectangular chamber with a wide hollowed center to allow for the fibres to curve out along the long axis, and the short axis is perpendicular to the trap axis, such that the distance between trap center and window is minimal, as shown in figures 6.11a and 6.11b.

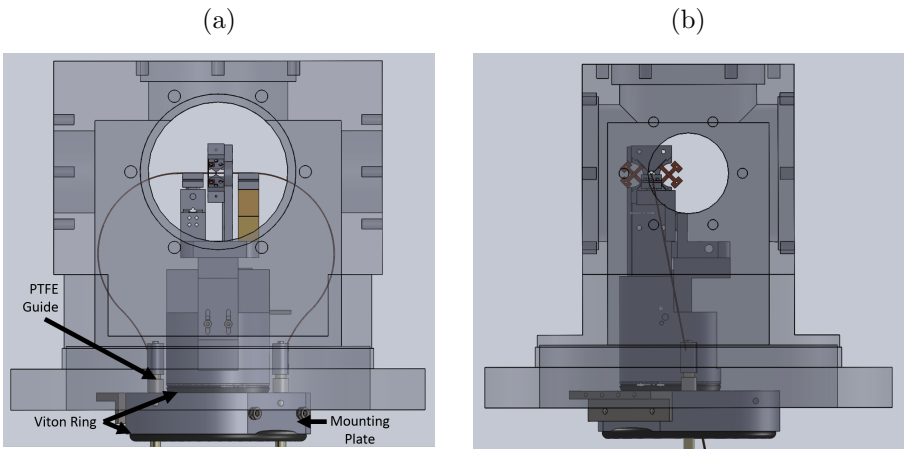

Figure 6.11: Image of the trap within the rectangular chamber, made transparent for clarity. Image (**a**) is viewed from the long-edged side and (**b**) from the short edged side.

The fibres are to be guided around the chamber without touching the internal wall by the use of a guiding PTFE rod with a groove cut to seat the fibre and a tension-relieving clamp at the top edge. The PTFE rods are held by a grub screw in the bottom mounting plate at the bottom of the figure. The vacuum-compatible Viton rings provide vibrational isolation from the remainder of the vacuum system and lab.

This structure is to be placed upon a mount across the opening of a CF160 cross, which has two M4 screws bolted pointing upward which pass through the structure which will prevent the trap falling sideways inside the chamber. The complete lower vacuum system design is shown in figure 6.12

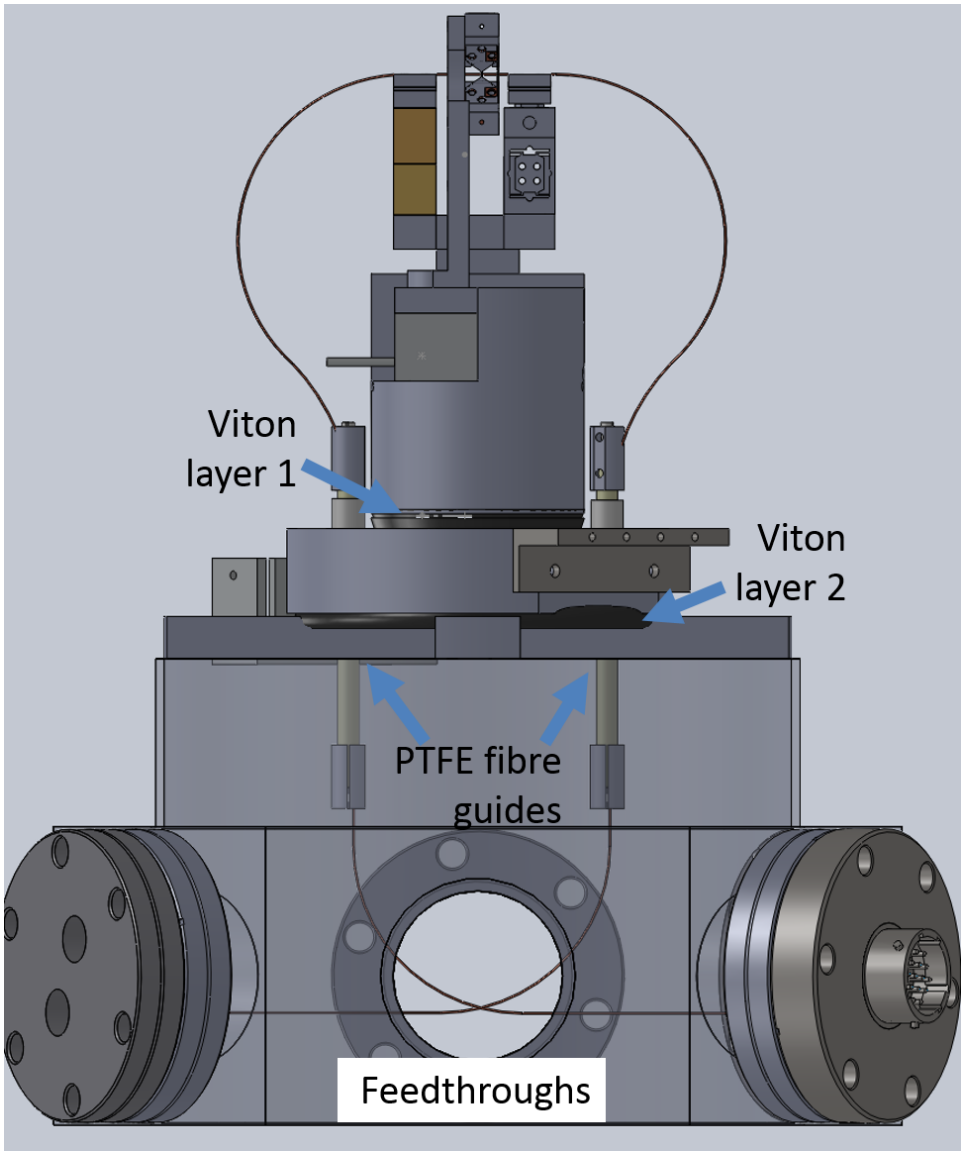

Figure 6.12: Main components of the lower vacuum system. The UHV compatible-viton layers provide vibration isolation from the rest of the table. The PTFE fibre guides are also intended to reduce transfer of noise into the fibre by alternative clamping means. The wires from the feedthroughs are not shown.

Chapter 7

Assembly

7.1 RF Trapping Electrodes

For the rf-component of the ion trap, the radial electrodes must be 50μm apart to support a stable trapping potential. Due to this small scale, defects present on the electrodes are to be strongly avoided in order to prevent degradation of the trapping potential. As discussed in section 6.1.2, we are using blade-like electrodes for maximum optical access, which have a polished, fine tip which is free from any defects. As the rf-blades are to be cut to only $\sim$ 300μm wide axially, we use a hard metal, tungsten carbide, to make them from. The tungsten carbide blades are available to purchase commercially from American Cutting Edge[1] with a thickness of 218μm and length of 38mm. These are too thin and brittle to be machined mechanically, so we use the non-contact process of wire erosion to machine the blade shape. An

[1] American Cutting Edge, 480 Congress Park Dr.Centerville, OH 45459, 888.252.3372

example of the blade quality before wire erosion is shown in figures 7.1a and 7.1b.

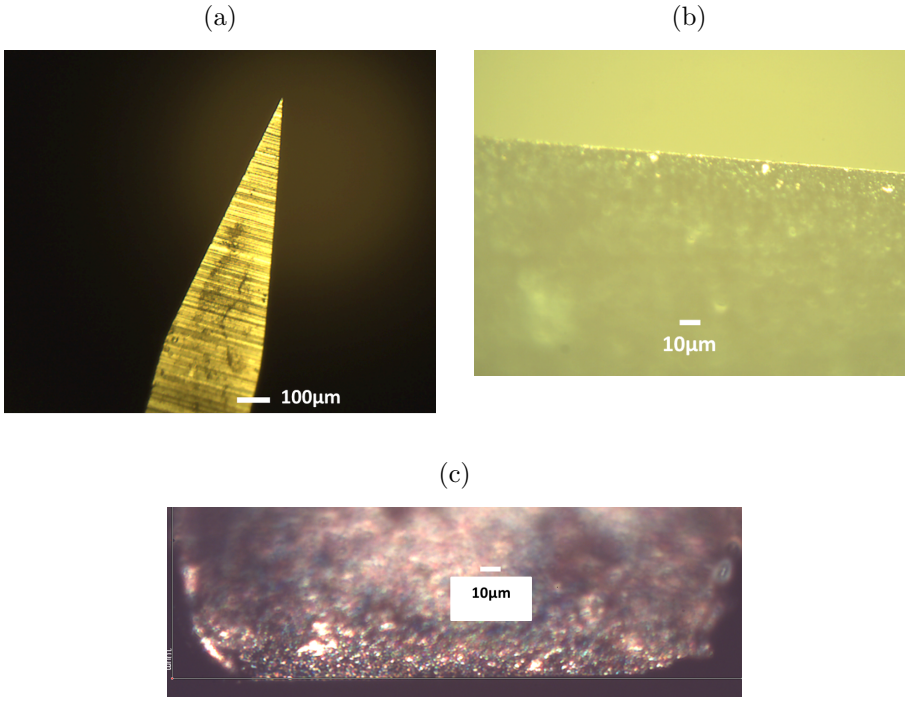

Figure 7.1: **a** Microscope photo of the side profile of one of the blades before wire erosion. **b** Microscope photo of the blade tip on the long-side of the blade. The tip is free of defects above 1m in size.**c** Microscope photo of an initial attempt at cutting an electrode by wire erosion. The 277μm blade has been blunted.

The first wire erosion attempts caused significant damage to the blade surface, shown in figure 7.1c. It appers that while the wire is brought towards the electrode surface, the initial sparks leap over a wide area of the exposed tip, causing significant erosion where none was intended. After these initial unacceptable attempts, the cutting method was adapted to a 'hammerhead' shape. These were in general

much more succesful, and we have a roughly 50% success rate in the cut electrode having the correct shape, dimension and blade quality. Of the remaining 50%, some are only hindered by the hammerhead shape leaving the blade tip too wide. For this, we used fibre polishing paper to carefully polish away the wide edges, with some success, shown in figure 7.2c.

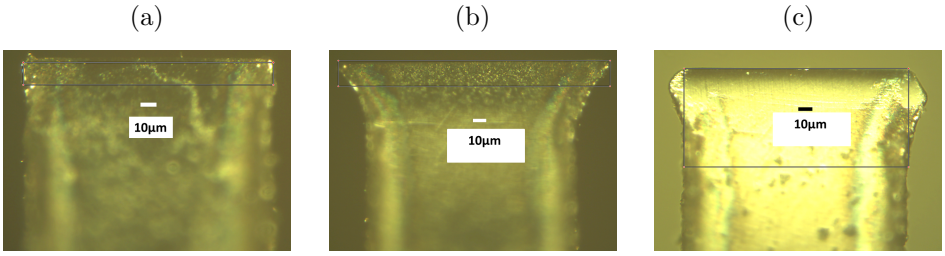

Figure 7.2: **a** Profile of blade cut by wire erosion to 298μm width. Blade tip still in good condition after adjusting cutting method. **b** 'Hammerhead' shaped blade from wire erosion cutting too wide at the tip. The tip length is 392μm, too long for use without polishing. **c** Shows the same electrode as b but after polishing with polishing paper. The new blade length of 305μm is short enough for usage, and the surface appears in good condition.

Figure 7.3a shows the setup we used for aligning the electrode pairs. We inspect the blade tips using the microscope to the upper left of the image. The delicate and fragile quality of the blades led us to align each pair of blades individually. In 7.3a, we are aligning the bottom pair. The blades are positioned according to the separation of their tips and are translated by loosening two of the screws and gently pushing the electrode from the blunt rear section with a fine tipped screwdriver. Once the positions are correct, the bolts are gently tightened again while correcting for misalignment of the applied stress.

We use modified M1.6 bolts which have the thread removed for 1mm beneath the head to maximise the clearance from the electrode itself, as shown in the lower part of figure 7.3b. This is necessary to avoid connecting the electrode to ground, as well as allowing it freedom to move into position. We check for an electrical connection between electrode and mounting structure regularly throughout the process, and reposition the electrode in the event of a short circuit. After they are aligned to the $50\mu m$ target, the bottom mount structure is removed from the side wall[2] and the top pair is imaged by attaching the top mount to the side wall, in the bottom mount's place. This is simply for ease of access to the screws holding the electrode in place, as shown in figure 7.3b. We then repeat this process for the upper pair.

[2]As shown in figure 6.6a from section 6.2

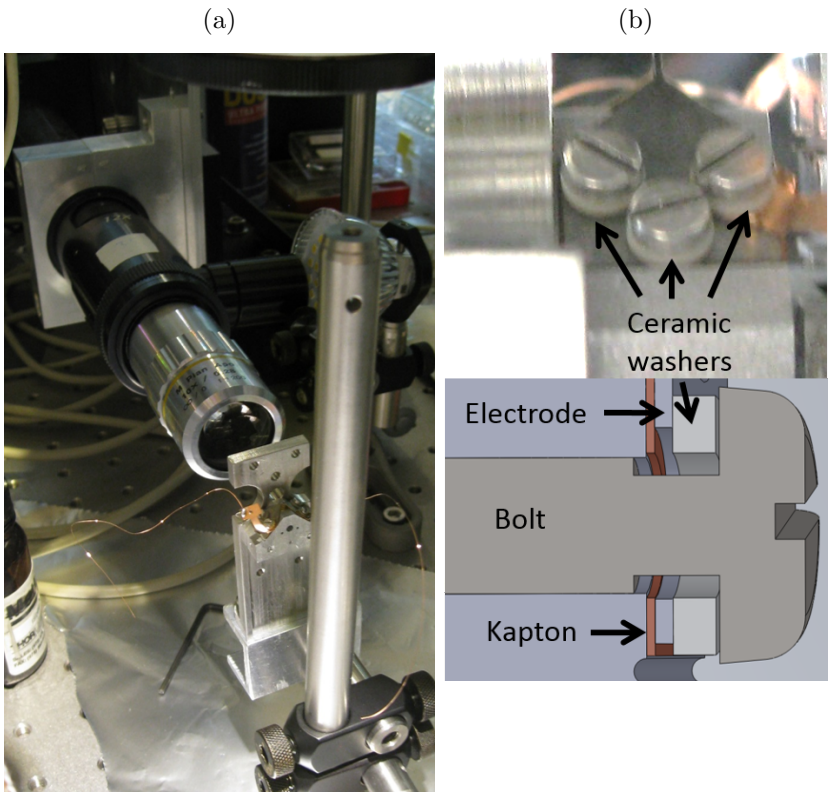

Figure 7.3: **7.3a** Image of the setup for aligning each pair of electrodes. A 600X microscope is used from the side while aligning[3] . **7.3b** Upper: Radial view of one blade. The three screws holding each electrode in place are electrically isolated by the labelled ceramic washers. Lower: Cut-through of the solidworks model of the trap. The removed section of thread near the head of the bolt and ceramic washer prevent the RF electrode and bolt coming into contact. A Kapton sheet between the electrode and mount completes the isolation.

The microscope view of the initial RF-electrode alignment process is shown in figure 7.5a. When both upper and lower pairs of electrodes are aligned, the setup is rotated such that the side wall is now horizontal, as shown in figure 7.4. The lower mount is bolted back into position, and

the upper mount is slowly bolted into the upper position, while using the slack on the through-holes in the side mount to keep the blades well separated. A microscope above the horizontal setup is used to carefully bring the electrodes together to form the 50μm separated blade tips. The microscope from the side is used to ensure the electrodes are in the same plane.

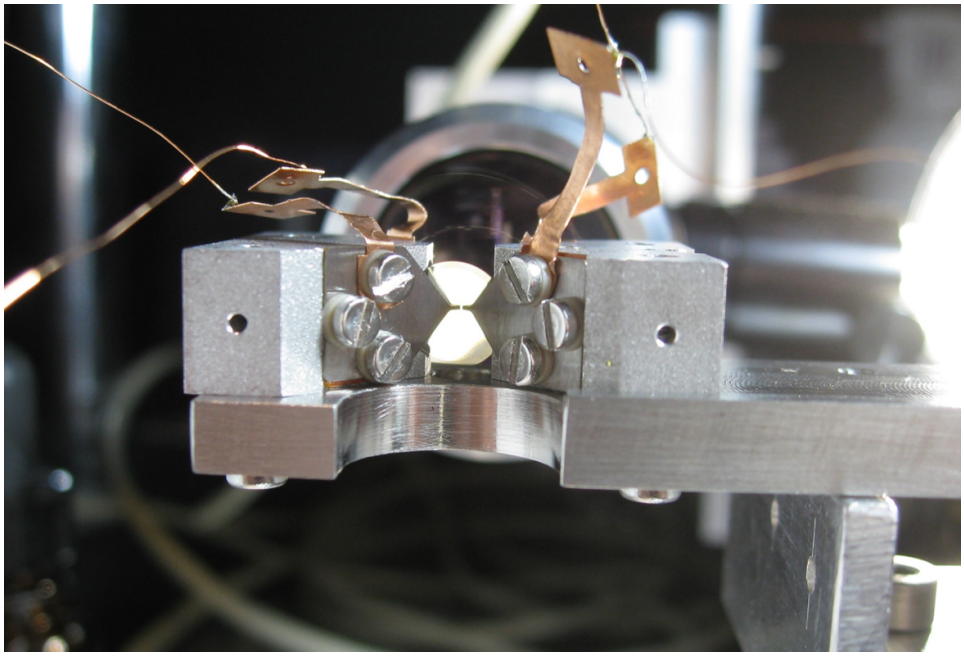

Figure 7.4: Image of the setup for aligning the four electrodes together. The blade tips are viewed with a 200X microscope from above[4].

(a) (b)

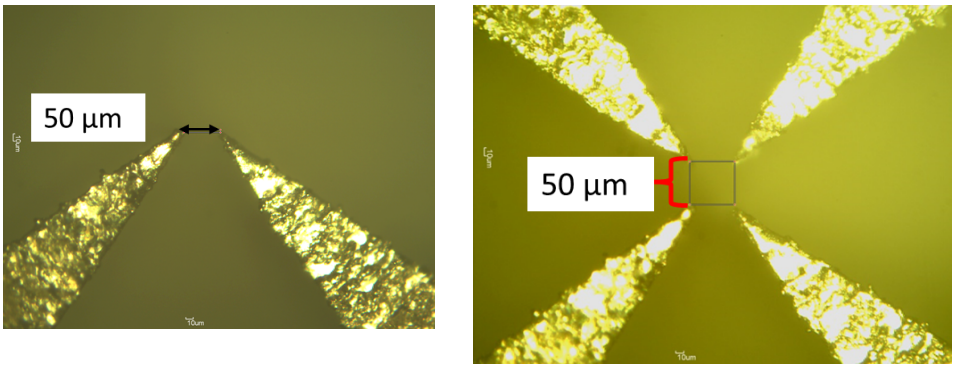

Figure 7.5: (**a**) Microscope image of the top pair of electrodes aligned on the top mount. Their height and width separation are measured from this view, and a second camera above measures the offset of the blades along this viewing axis. (**b**) Microscope view of all four electrodes aligned together. The left two are the top pair of electrodes from a and the bottom pair are on the right.

To finally confirm the electrode positions, the structure is rotated again to be vertical, and reimaged on the higher magnification microscope. Figure 7.5b shows the two pairs of electrodes aligned to the correct separation.

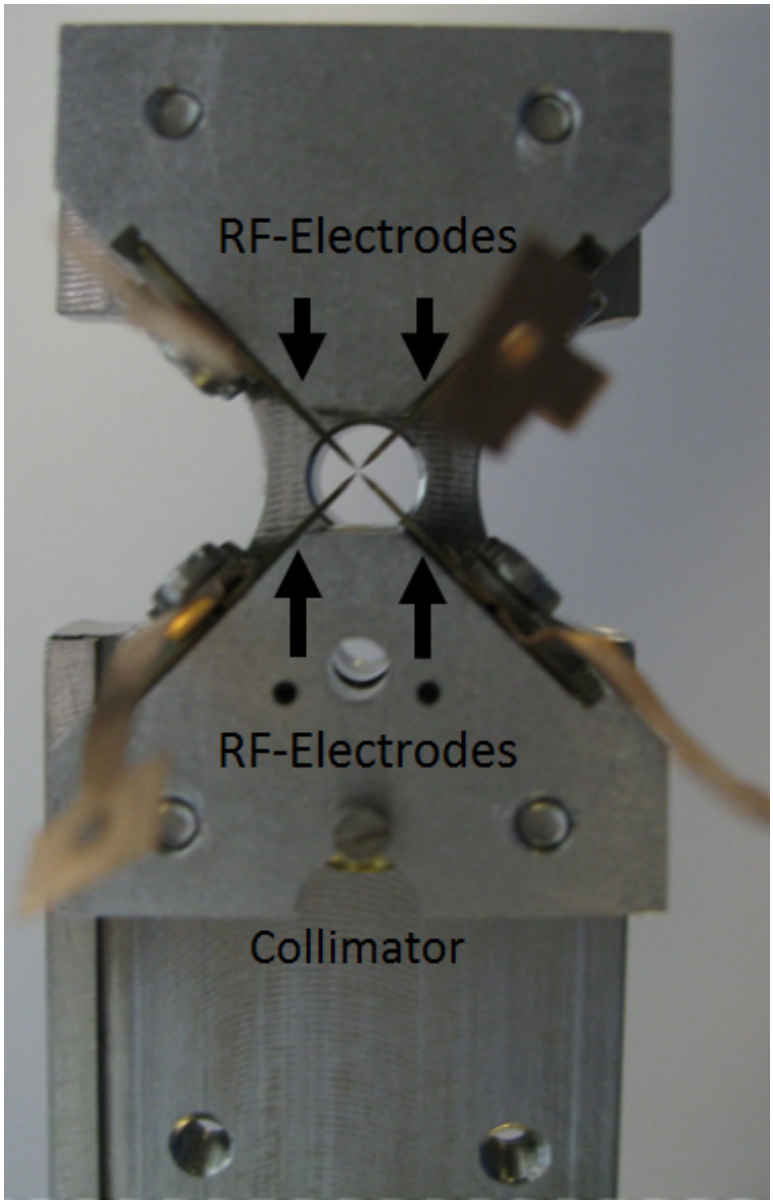

Figure 7.6: The assembled rf-structure, as seen along the future trapping axis. The electrodes and copper connectors are each isolated from one another and from the main body.

7.2 Cavity Assembly

7.2.1 The Cavity Mount

The fibre and DC electrode mounting stage as described in section 6.3.1 was created in two stages. First, each piezo required gluing into position, so we created a set-square cut from PTFE to act as a guide for the assembly, shown in figure 7.7a. We use the two-component epoxy STYCAST 2850FT with catalyst 23LV[75] for its vacuum compatible properties. The glue is degassed for 10 minutes at 10^{-3}mbar to remove air bubbles from the mixture, then applied. At the end of the piezos we include a Kapton layer to insulate the them from eachother. The 1μm range scanning piezo[5] is soldered to a copper wire with diameter 0.2mm (figure 7.7b) before gluing. The glued piezo-stack featuring the X[6] and Y[7] axis alignment piezos is shown in figure 7.7c.

[5] NOLIAC CSAP03[76]
[6] Physik Instrumente P-141.10 PICMA-Shear actuator, 10μm travel range. [77]
[7] Physik Instrumente P-888.30 PICMA Piezo actuator, 11μm travel range. [78]

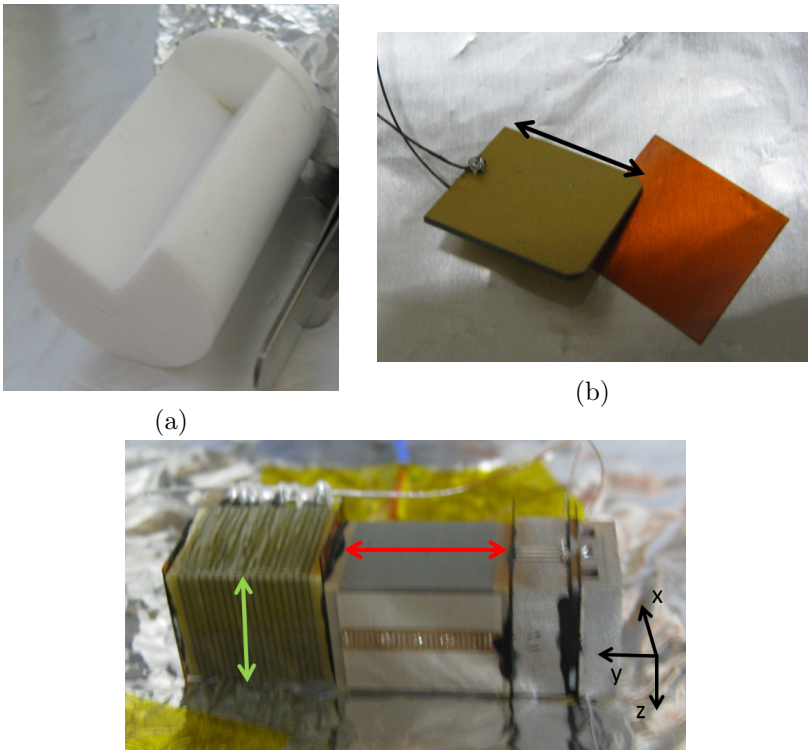

(a) (b) (c)

Figure 7.7: (**a**) The PTFE set-square used for guiding the assembly of the piezo-stack. The stack was clamped into the 90 degree groove for 24 hours while the glue cured. (**b**) The 1μm piezo for scanning and locking of the cavity. The black arrow highlights the axis of travel. (**c**) View of the assembled piezo-stack. The red arrow marks the travel on the piezo in the Y axis. The green arrow marks the direction of travel in the X axis. Each piezo is isolated from the stainless steel frame and eachother by 125μm KAPTON sheeting.

Secondly, we glued the other v-groove to a second 1μm scanning piezo using the same method, and then used a transitioning aluminium block to bolt it to the flexure stage machined using wire erosion as shown in section 6.8a. The v-groove atop the piezo-stack and the v-groove above the flexure stage are both then attached to a base plate,

as shown in figure 7.8. This stage is then used for coarsely aligning the cavity using the flexure stage prior to insertion into the full system.

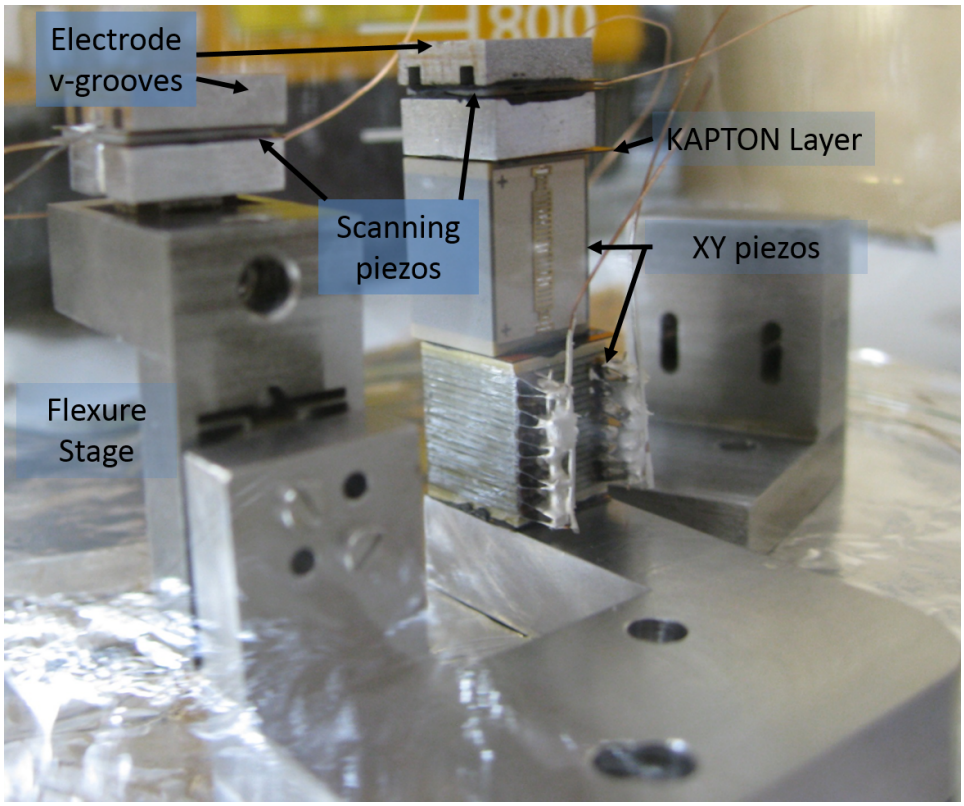

Figure 7.8: Assembled DC electrode mounting structure.

7.2.2 Cavity Fibre - Electrode Insertion

The DC cylindrical electrodes are stainless steel tubes available commercially from Coopers Needle Works,[8] with an inner diameter (ID) of 254±40μm and an outer diameter (OD) of 457±40μm. The large machining uncertainty on the ID means every electrode requires checking

[8]Coopers Needle Works Limited, 261 - 265 Aston Lane, Birmingham, West Midlands, B20 3HS, England, +44 (0)121 356 4719

before attempted use with a live fibre, to prevent it getting stuck and damaged. These are cut to the correct length and polished.

For the cavity fibres, these are first glued into the DC electrodes without connectorisation. The long distance between the DC mounts and the trap region means the DC electrode lengths are 16mm and 20mm in length (discrepancy due to asymmetry of radial mount), across which distance there is always a slight bend or 'sway' of the fibre due to the copper coating which is difficult to correct for. Inserting the cavity fibre into the DC electrode therefore requires a specific process to avoid damaging or dirtying the end facet. Insertion with the front facet first is succesful by microstage if the tube is very short, and the bend of the fibre not pronounced. It is possible to travel at least 6mm without the fibre groping the inside wall of the electrode, and using a camera focused on the end facet to centerise the electrode at each incremental movement down the tube. However, for longer electrodes, the fibre sway causes it to be much harder to predict and correct for the position of the fibre in the electrode, especially because the electrode is too long for a good image of the end facet to be formed on an end-facing microsope. Instead, we use the unpolished and unconnectorised end of the cavity fibre to insert into the end of the DC electrode. The setup for this is shown in figure 7.9. First, the DC electrode is polished with fibre-polishing paper [9] to produce an even finish, as shown in figure 7.10a, and clamped into a static mount. Then the fibre is inserted and pulled through until approximately 3cm are left exposed as shown in figure 7.10b. We use a camera to focus on the tip of the electrode, and

[9] Thorlabs LF1D - 6" x 6" Diamond Lapping (Polishing) Sheets, 1 m Grit

can see that the electrode is covered in copper shards and scrapings at this stage, which must be removed before the end facet is moved closer. Figure 7.10c shows some remaining dirt with the fibre in focus. To do this some optic tissue with a small amount of alcohol is used to clean away the detritus. Now more carefully, the remainder of the fibre is drawn into the tube, until only a few millimeters are exposed. A final clean away of detritus, this time ideally with a dry tissue to avoid dirt being carried with alcohol via the capillary effect onto the end facet, is applied, and now the fiber is securely clamped to a translation stage along the axis of the electrode. The fibre is slowly withdrawn entirely into the tube, watching on the microscope to be sure there is no dirt near the tip. Once it is far enough inside to be invisible on the microscope, the tube tip is wiped once more with a dry optical fibre cloth to remove any detritus. The cleaned electrode with fibre in the same focal plane is shown in figure 7.10d.

Now the fibre protuded again out of the tube by a few millimeters, and a pair of fine tweezers used to grasp the fiber on the copper section and gently tilt the fibre to be concentric with the electrode. Once this is set, the fibre is withdrawn into a position where it is flush with the end of the tube. At this point we add a micrometer gauge to measure the recession of the fibre inside the tube, which we set to 15 μm. Once in position, STYCAST glue is mixed, degassed, and applied at the rear end of the electrode, where it has contact with the fibre. Figure 7.10e shows the singlemode experimental fibre recessed and glued into position in a near-concentric alignment. The high viscosity of properly mixed STYCAST ensures no glue travels up and covers the end facet.

Due to the lack of glue near the tip, fibres can move around near the electrode opening and lose concentricity. For one fibre, we had a sample of tubes wire eroded so only the initial millimeter of tube is completely circular. The remainder forms a half cylinder. In this way we can place glue the entire way down the fibre, preventing this lack of concentricity and still without damaging the fibre tip.

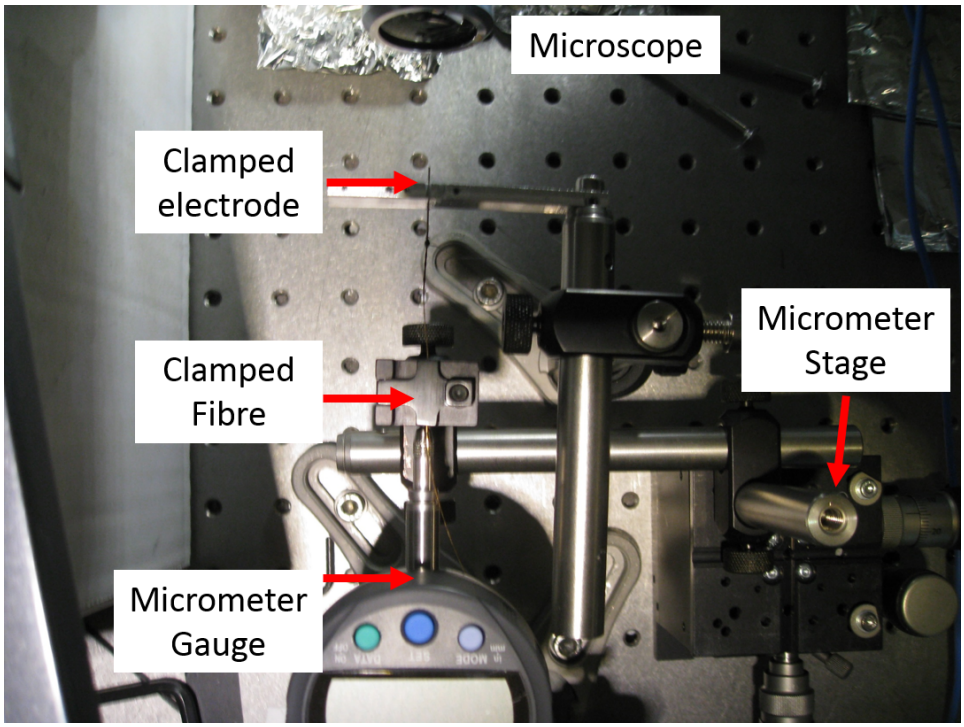

Figure 7.9: Setup for inserting the experimental fibres into DC electrodes for the trap. The electrode is held in a fixed position, while the fibre is clamped to a stage to allow it to be moved through the electrode with care.

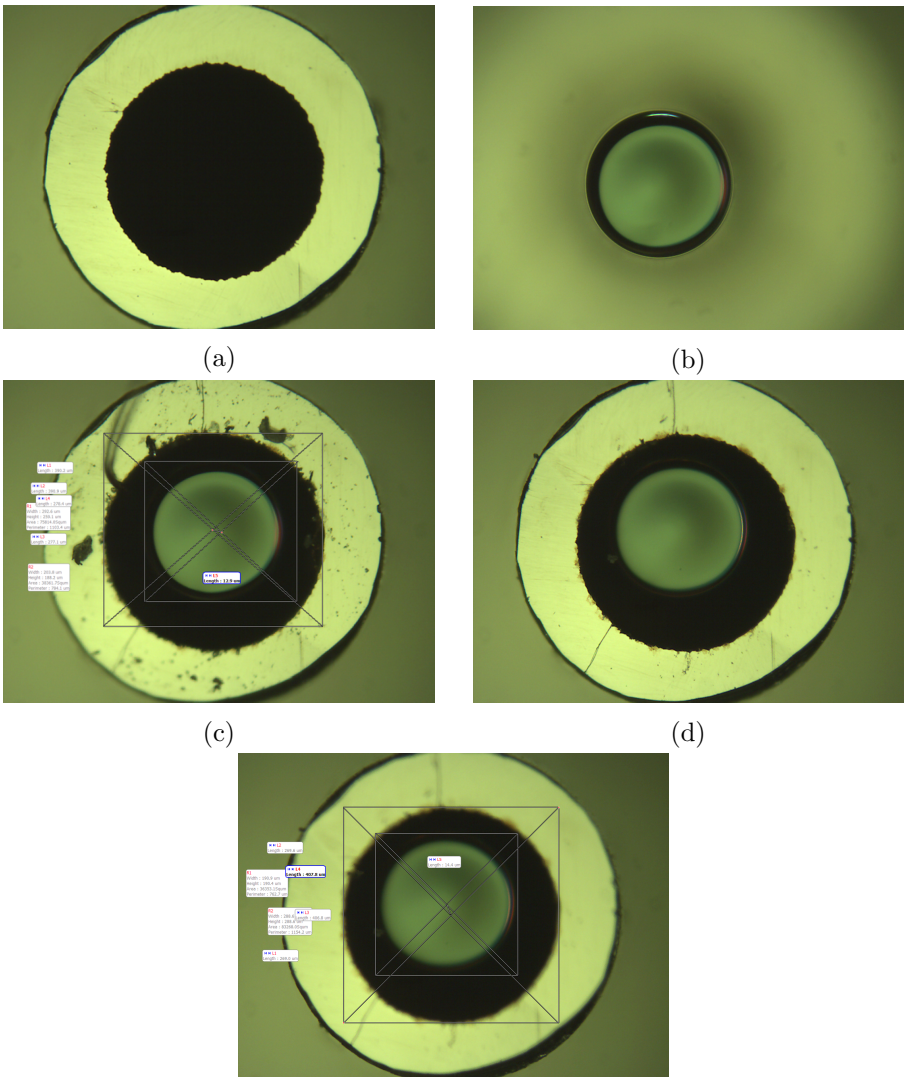

Figure 7.10: (**a**) Polished tip of DC electrode before fiber insertion. (**b**) Exposed fibre tip out of electrode. The electrode can be seen out of focus in the background. (**c**) The fibre brought into the focal plane of the electrode tip. Leftover copper shards and detritus are observable on the electrode surface. (**d**) The fibre and electrode surfaces after the fibre is recessed deep inside for a final cleaning of the electrode tip. Care is taken not to flush dirt into the electrode and onto the fibre. (**e**) Final image of the fibre recessed into the electrode by 15μm and near concentric with the electrode, and glued at the opposite electrode end.

7.2.3 Setting the Electrodes

To clamp the cavity fibres and electrodes into the v-groove, we use a vacuum compatible PTFE sheet which is screwed into the surrounding metal, as shown in figure 7.11a. For setting the cavity length, an external micrometer stage is used to move the electrodes closer together. Once near the desired length, fibre is clamped into place using the PTFE layer and the cavity length is fixed. Then the cavity alignment is tested by using a combination of the flexure and piezo stages. While testing in the absence of the RF, it is useful to begin with a very short cavity which is slowly extended, as is typical with FFPC finesse measurements. The cavity alignment is iteratively adjusted up to the target of 350μm separation between DC electrodes, for a cavity of 380μm. Figure 7.11b shows the setup outside of the vacuum system where we make the initial coarse adjustments to the flexure stage. The cavity length is adjusted using the clamps to the left and right of the image while we inspect the horizontal displacement from above using one microscope, and the vertical displacement using a second microscope from the side.

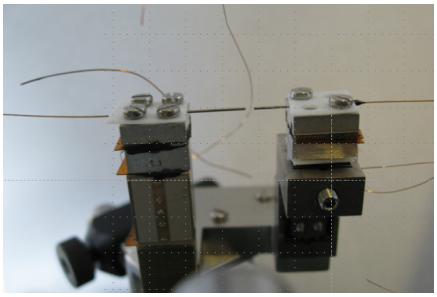

(a)
(b)

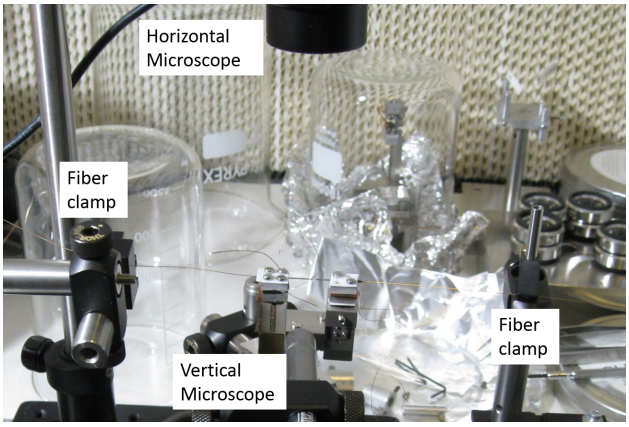

Figure 7.11: (**a**) Close view of the DC electrode-cavity setup test alignment. (**a**) The entire setup for testing the cavity. The positions of the fibres are monitored from above and the side with two microscopes, while we measure the cavity transmission of 866nm light.

7.2.4 Experimental Cavity Finesse

Scanning the cavity in the method described in section 7.2.3 provided a result as shown in figure 7.12. At 380μm the cavity maintains a finesse of around 33,000. The fitted line is to the same clipping loss model as described in section 5.4. We obtain a clipping radius of 27$\pm$3μm, and residual losses from scatter and absorption of 115$\pm$6ppm using the

transmission of 30ppm as a fitting parameter.

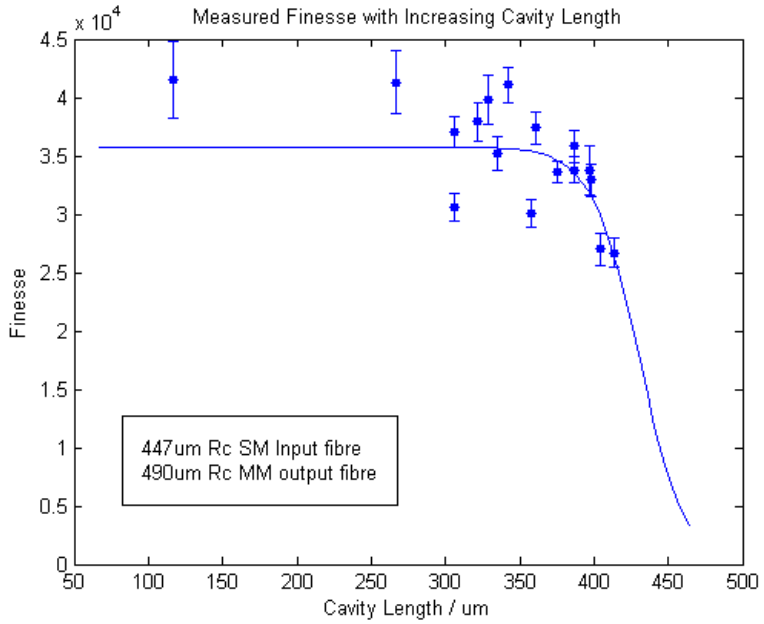

Figure 7.12: Finesse of the experimental cavity. Data is fitted to the clipping loss model. Each data point represents an average from 10 measurements of the cavity transmission peak as detected on an APD.

The fibres were then removed until the RF and DC components were finally joined together in the vacuum system. Figure 7.13 shows the RF and DC mounts assembled with the fibres back in their v-grooves. We again tested the cavity while aligning the RF and DC relative positions to one another.

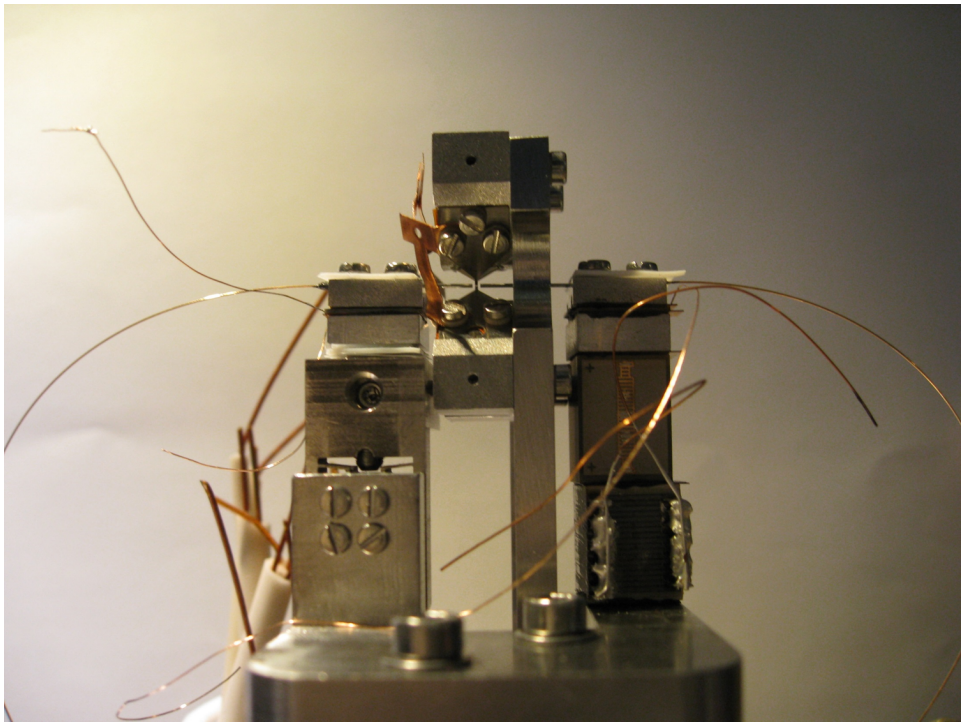

Figure 7.13: The assembled trapping structure, with experimental fibres being guided in a wide arc down to the lower vacuum system to meet the feedthrough to atmosphere.

Figure 7.14a shows a magnified image of the RF and DC electrodes as we bring the DC electrodes back into alignment around the RF. This is done slowly to prevent the RF and DC electrodes touching and scratching the polished surfaces of the electrodes, or worse the recessed cavity mirrors. Once the DC electrode spacing is set to the same 350μm separation, as in figure 7.14b we again scan the cavity while manually scanning with the X and Y piezos on the DC piezo stack to find a cavity resonance. Finally the 3D piezo is used to move the RF mount relative to the cavity, to overlap the cavity mode with the spacing of

the electrodes.

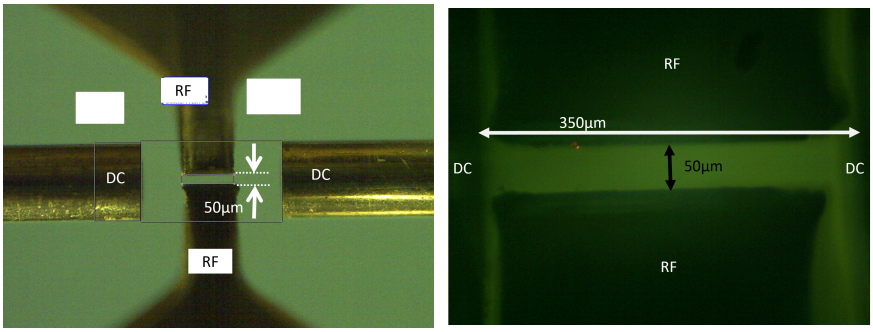

(a) (b)

Figure 7.14: (**a**) Magnified image from the side of the trap. Here the DC electrodes are being brought closer together by an external stage, the separation here is 820μm. (**b**) Higher magnification image of the RF and DC electrodes from above. Here they have the correct spacing and estimated correct alignment for the cavity to be passing through the RF. The cavity is now tested again at this stage.

Due to the small rf electrode distance, the alignment of the cavity axis with the trap axis is crucial to avoid clipping of the cavity mode by the rf electrodes. The finesse measured with 866nm through the cavity drops to $2,000 \pm 1,000$. To estimate the effect of this alignment we simulated the behaviour of the cavity finesse to take into account additional clipping losses from the RF electrodes blocking the cavity mode. We assume the cavity mode is overlapped perfectly with the goemetric RF center, but that there is an angle between the cavity and trap axis, as shown in figure 7.15a. We can estimate the reduced clipping radius arising from this angle using the geometry shown in figure 7.15b.

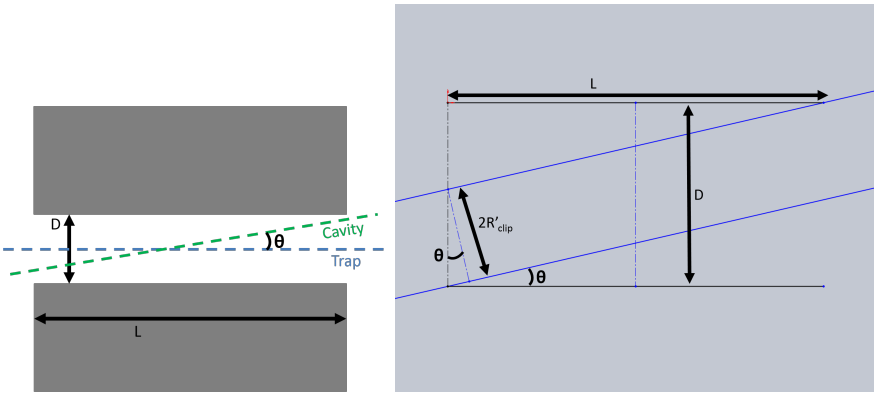

(a) (b)

Figure 7.15: (**a**) Image of potential angle misalignment between cavity and trap axes. D, L and θ denote the spacing of the RF electrodes, length of the RF electrodes and the offset angle. (**b**) Detailed schematic of the geometry. The diagonal blue lines indicate a simple cylindrical model of the cavity mode passing between the electrodes marked in black. The maximum allowable mode diameter is $2R'_{clip}$ due to occlusion by the electrodes. θ is the offset angle

From this geometry we can calculate the new clipping radius, R'_{clip} using

$$R'_{clip} = \frac{1}{2}(D\cos(\theta) - L\sin(\theta)) \tag{7.1}$$

A simulation of the modified clipping radius of the experimental cavity at a length of 380μm as the angle offset increases is used to recalculate the finesse as shown in figure 7.16.

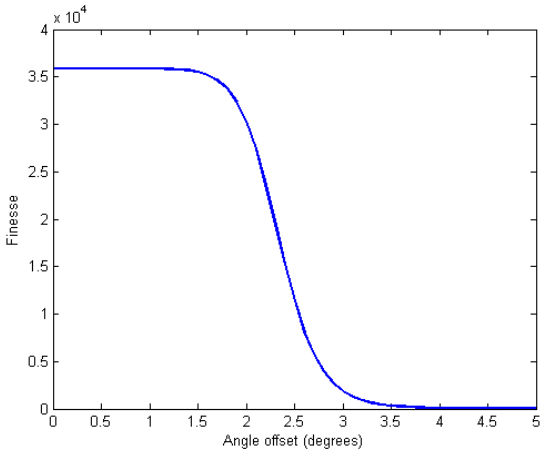

Figure 7.16: The outcome finesse, based on the fitting parameters from 7.12 with the additional losses included as the angle offset increases.

Evidently even a small angle offset of 3 degrees can reduce the cavity finesse to a fraction of its original value. Due to the recession of the fibres in the long electrodes, we do not know exactly how large this angle offset is, but can infer that it is no more than 3°. This model assumes the cavity is still passing through the geometrical center of the RF. To confirm this, we cut a narrow blade of Kapton sheeting and inserted it radially between the RF electrodes into the cavity mode.

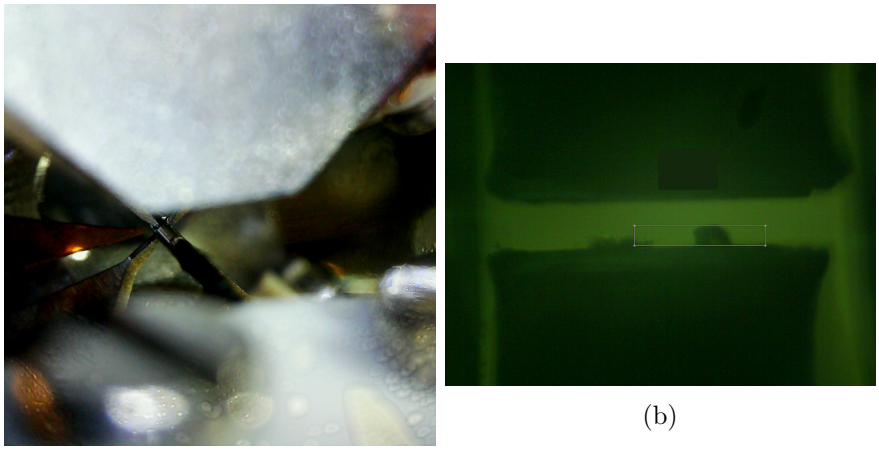

(a) (b)

(c)

Figure 7.17: (**a**) Kapton sheet inserted on the left (in orange). (**b**), (**c**) Top and side views respectively of the Kapton blade entering the RF gap. This position marks the point that the 866nm signal is entirely blocked.

As we pass the Kapton sheet through, we observe a different behaviour in the transmission for different wavelengths fed into the cavity. For 866nm light for which the cavity has the highest reflectivity[10], the signal is very sensitive. The Kapton sheet only penetrates 18μm before the transmission peak is no longer visible. For 787nm light, for

[10]Reflectivity = 99.997%

which the cavity is less reflective[11] the transmission peak is less sensitive, and remains for the full distance we can fit the Kapton sheet, at 30μm. Finally we used some 698nm light which is almost transparent to the coating. In this case there is no transmission peak, but a level background is detected as the fibres are effectively butt-coupled. Figure 7.18 shows a summary of the transmission signals from the cavity with and without the Kapton sheet present.

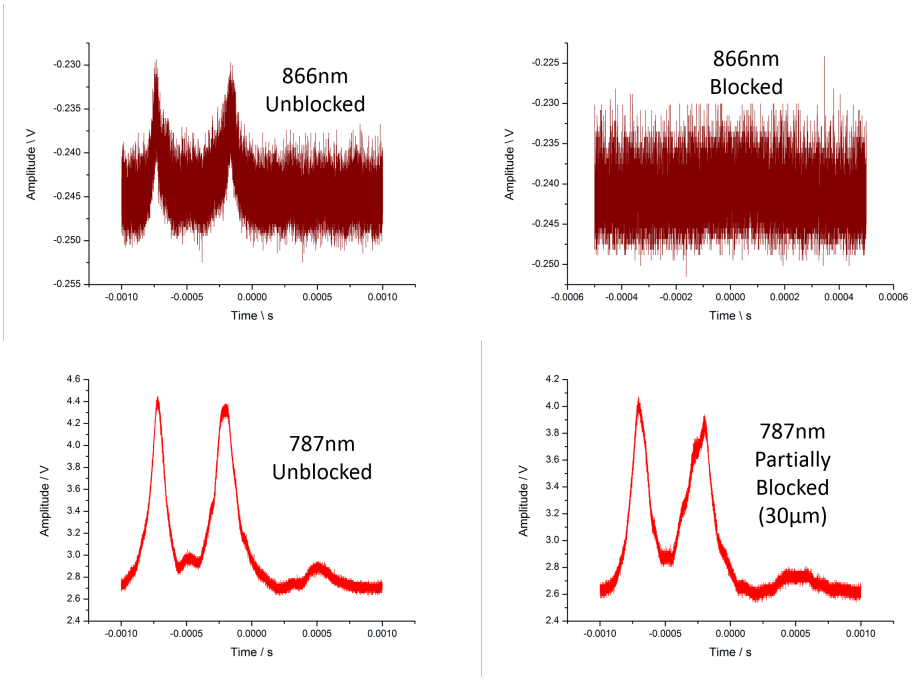

Figure 7.18: The left column shows the transmission signal as detected by an APD for the cavity with 866nm and 787nm light coupled in. The right column shows the same, but with a Kapton blade inserted to block part of the cavity mode.

This result implies that the Kapton blade is causing additional losses within the cavity. The high reflective for 866nm light causes

[11] Reflectivity $\approx$ 99.9

high sensitivity to additional losses from clipping as the cavity field cannot build up to transmit through the high reflective coating. The impact on the 787nm light is less pronounced, but present. The 698nm remains at the same background level as the transmission is not the result of a cavity effect. Partially blocking the cavity mode has no effect as the majority of the output multimode fiber core is still unblocked for light to be coupled in to. This strongly implies the cavity mode is overlapped with the geometrical RF center.

7.3 Oven Mounting and Collimation

To produce the atomic calcium to be ionised within the trap, we use a ≈15mm tantalum tube which we seal at one end and fill with grated pure calcium. This is connected to a a high current source which heats the tube, creating an effusive beam of calcium atoms. These are directed in the direction of the opening of the tube. Filling the trap center with too much calcium is detrimental to the performance of the trap as patch potential can form from calcium deposits, as well as lowering the cavity mirror quality. Therefore we use two 200μm collimation holes in the lower RF mount, as shown in the cut-through in figure 7.19. When aligning the RF electrodes, we used a fibre-coupled laser to check the RF electrodes were well situated above the collimation holes.

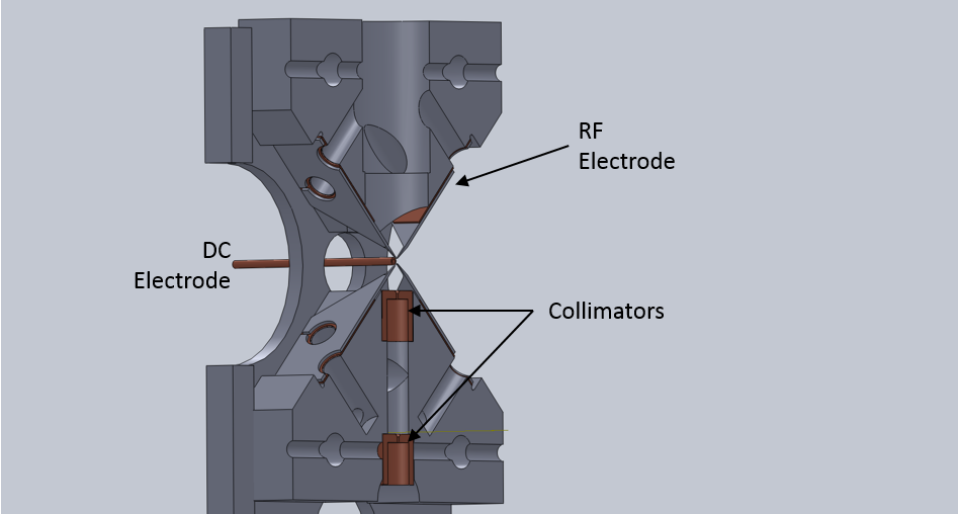

Figure 7.19: Cut-through image from solidworks model of the RF mount, highlighting the locations of the oven collimators. The oven is placed below the collimators in the image.

The oven is filled with pure calcium which will rapidly oxidise when exposed to atmosphere, so preparing it was the final task before closing the vacuum system and starting to pump. We created a stainless steel 'counterweight' to stabilise the wires coming directly from the feedthrough, and then connected the oven to this, as shown in figure 7.20 This enabled us to align the oven with the collimation hole successfully. There is no clamping of the oven into position to reduce thermal expansion of the trap structure via conduction.

7.4 UHV Considerations

The entire trap will be operated under Ultra High Vacuum conditions (UHV, 10^{-10}mbar) and as such suitable considerations must be made. As is typical for an ion trap under UHV, the system is placed in a stain-

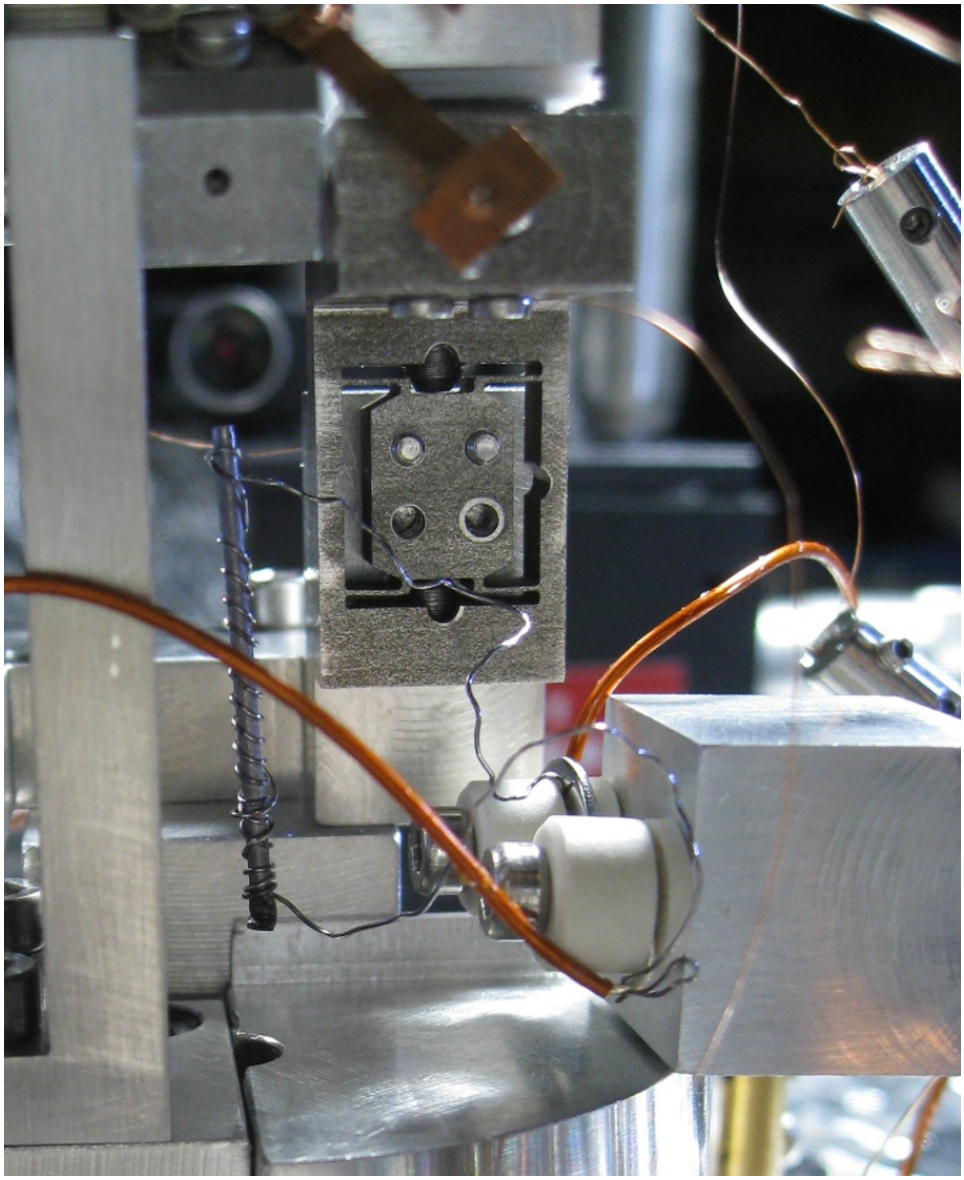

Figure 7.20: Test mounting of the oven using the weighted block to hold it in place. The block is prevented from a short circuit by the ceramic washers.

less steel vacuum chamber which is sealed mostly with copper gaskets with the of the radial chamber windows which are indium sealed to allow large of the optical access. Several of the components including the piezos require gluing into the structure as they lack any other mounting mechanism. For this we use a vacuum compatible epoxy [12] which is degasssed prior to application to prevent forming microcavities of trapped air leading to 'virtual leaks' once the system is closed. This degassing process involves pumping the glue down to roughing pressures of aroud 10^{-3}mbar for ten minutes, or until the glue stops visibly bubbling. The STYCAST glue is curable at room temperature making it suitable for temperature sensitive applications such as on the piezos. At room temperature this curing time is approximately 24 hours for a correct ratio of the two-part epoxy mix.

The number of required electrical connections is quite large, 4 wires carrying rf are required for each rf electrode, and each piezo requires a live and ground connection for each degree of freedom, then the DC electrodes each need a live connection, and the oven. In total the system needs 18 DC wires. We use a 19-wire KAPTON-coated ribbon from LEWVAC which is terminated on a male connector attached to the mounting plate highlighted in figure 6.11a. The connections to the top half of the trap are terminated in the female part of the connector shown in figure 7.21, and the KAPTON coated kept to only the minimum length required. This way we can group certain wires into specific roles that are close to one another, such as the X and Y translational piezos. In addition, clamping the connector in place prevents the wires

[12] STYCAST 2850FT with catalyst 23LV[75]

in the trap being held under any tension, relieving stress and providing further vibrational isolation. The top ends of these wires are held in barrel connectors, supported by a combination of the ceramic and wire elasticity. From these barrel connectors, fine 125μm wire makes the last 3-5cm travel to the relevant component.

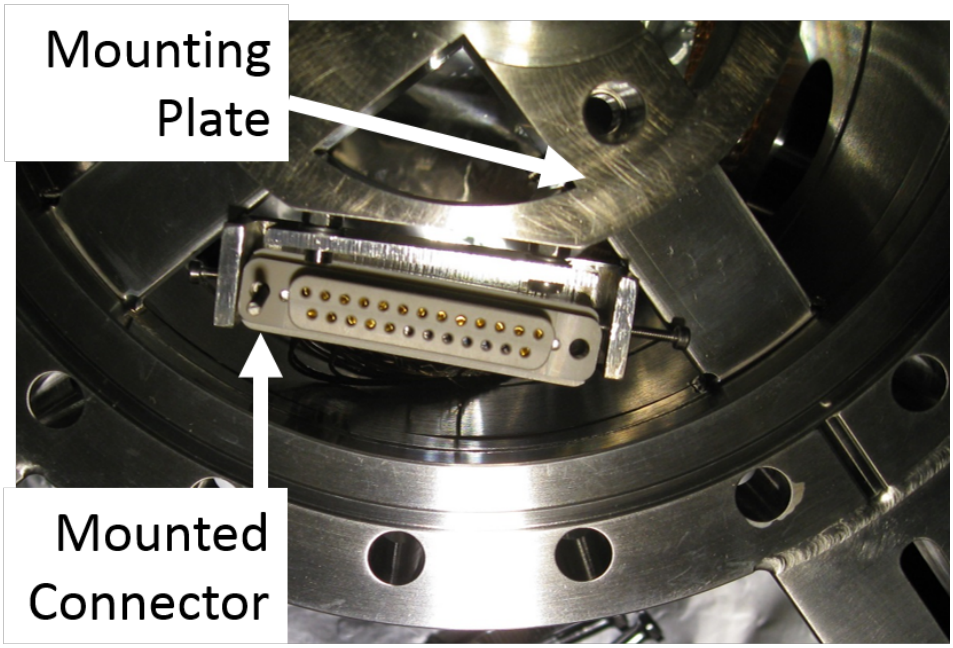

Figure 7.21: Photo of the mounted position of the male connector clamped to the vibrationally isolated mounting plate.

These wires are easily bent out of the way of the side windows. Again, we use a set of barrel connectors to use a fine wire to cover the last distance to the electrodes to minimise vibrations from the stiff rf-wires.

7.4.1 Optical Fibres - From Trap to Atmosphere

Due to the fragile nature of optical fibre, we use an intermediate fibre connector on the atmospheric side of the vacuum system, to an second connection in vacuum which leads up to the cavity itself. We use Thorlabs ceramic mating sleeves[13] on a bare ferrule to retain vacuum compatibility and achieve well coupled light even with APC ferrules on the single mode connection by orienting the ferrules 'manually' without the key. For the intermediate fibres passing from atmospheric to vacuum, we designed a customised flange which is modular in design to allow replacements of individual parts in the case of fibre damage and necessary replacement. The atmospheric end of the fibre is connectorised and threaded into a 300μm hole at the end of a 40mm long, 6mm OD stainless steel tube. This is then fed into a Swagelok fitting welded into a usual blank CF-40 flange to pass the fiber into vacuum. We use a blank CF-40 flange and weld two 6mm-tubing Swagelok sittings into it, which are each then fed one of the 6mm stainless steel tubes. The Swagelok fitting ensures an airtight seal around the tube, and to make the tube itself airtight around the fiber, we backfill the entire tube of 40mm with degassed STYCAST glue. Figure 7.22 shows a cross section of this design. To check the vacuum quality of the weld, we originally placed a Swagelok plug onto the fittings and attached the flange to a turbo pump without the fibres. In this instance the pump rapidly reached its base pressure of 5x10^{-7}mbar without baking and measure the leak rate to be below 1x10^{-12}mbar/l/s.

[13] ADAF1 - Ceramic Split Mating Sleeve for OD 2.5 mm (FC/PC, ST/PC, or SC/PC) Ferrules.

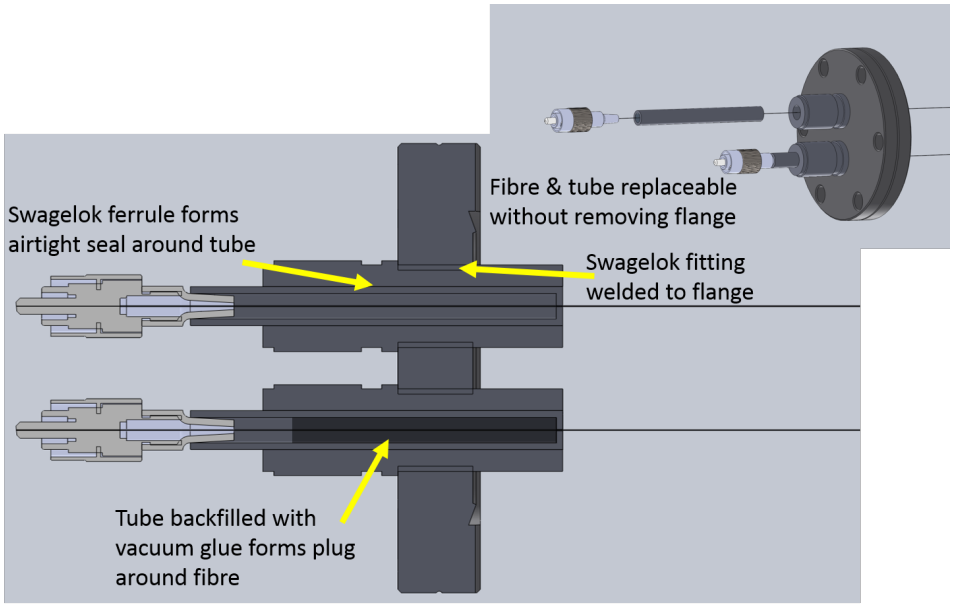

Figure 7.22: Cut-through image of the solidworks model of the feedthrough. Inset: Exploded diagram of each major component. Left is the fibre connector, center is the glue-filled tube, and right is the swagelok-fitted CF-40 flange.

The fibre minimum bend radius is 40mm, for which there is sufficient space either side of the trap within the vacuum chamber to accomodate. The fibres are guided down in a cylindrical PTFE block with a slit cut, down to the feedthrough flange. The PTFE guide is fixed to the chamber frame for stability, and the material was chosen to help damp vibrations coming from the optical bench and being transferred through the fiber and into the cavity, which is also damped as discussed in section 6.4.

Single-mode Cavity Fibre Splicing

We used APC single mode ferrules for the single-mode cavity fibre connector, to diminish any effect of reflections causing drift in the amplitude of the cavity signal. The atmospheric APC connector can be connectorised in the normal fashionThorlabs guide available at [74] Provides an excellent step-by-step procedure. and the vacuum side can be completed by performing the procedure with a bare-APC ferrule[14] with a mating sleeve attached to the back for 'handhold' support. However, APC connectors are not available in the 200μm size range to fit our single mode cavity fibre, so we made the feedthrough with a copper coated 125μm diameter fibre. [15] We used a fibre-splicer[16] to splice the two fibres together. The splice parameters include the voltage, stuffing rate, gap between the fibres before splicing, and the offset of the spark to ensure the larger fibre melts without entirely melting the smaller fibre. Figure 7.23 shows the two fibres spliced before and after splicing. To secure the structural weakness of the splice, we threaded two larger diameter (270μm) bare ferrules connected with mating sleever over one of the fibres before the splice. Once the splice is complete and the transmission checked with 698nm light to be 67% percent transmissive, the protective larger mating sleevers are moved over the splice point and glued into place using Epotek 353ND epoxy[79], which is heat cured in a couple of minutes. This protective assembly is shown in figure 7.24.

[14]Not available commercially - but can be obtained by delicately dismantling a usual APC connector with a dremel.

[15]IVG Cu600 125μm diameter copper coated fibre. [66]

[16]ArcMaster FSM-100M+

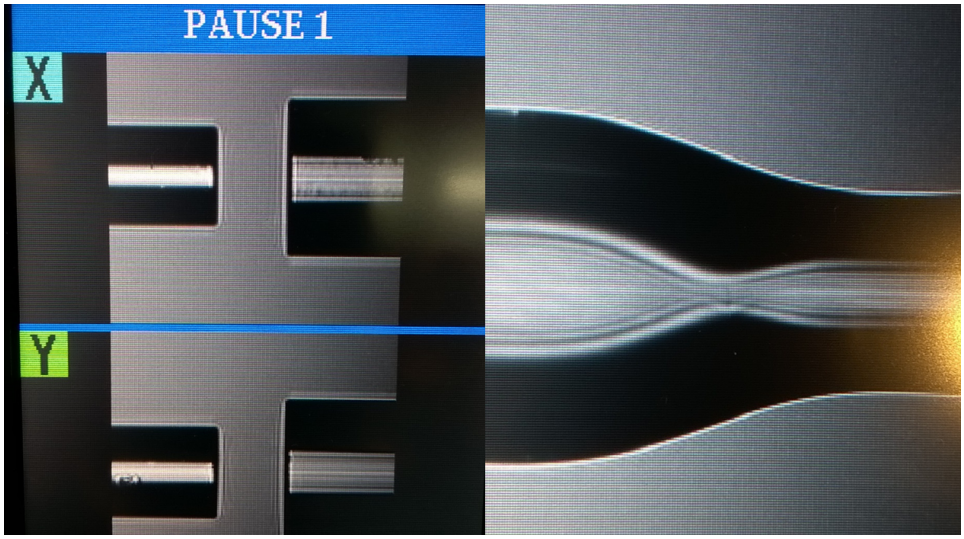

Figure 7.23: Left: Side profiles of the fiber pair before splicing. They are automatically aligned by the splicer. Right: The spliced fibre pair. The white line is a reflection, not the fibre core.

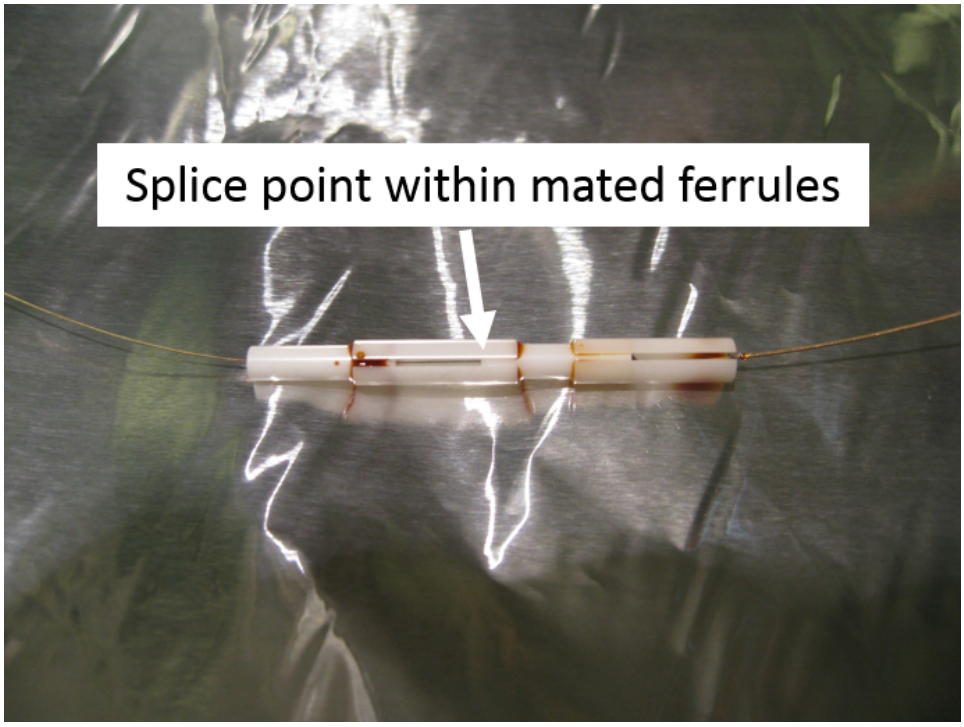

Figure 7.24: The protected fibre splice within ceramic ferrules. The brown marks are remnants of Epotek 353ND epoxy, typically used for fibre connectorisation.

7.4.2 Pumping and Baking

Below the 6-way cross which supports our flange connections for the fibres, DC and RF connections, and ion gauge, we have a bellows and ion pump with sublimation pump. Initially the system is connected to a turbo pump to bring the system pressure down to a point the ion pump can safely operate. The system was leaked tested with helium and found to be leak tight. We baked the system to remove any moisture at temperatures between 200°C and 85°C. The lower temper-

atures were used in the trapping chamber itself due to the low melting points of the indium sealed windows, and temperature sensitivity of the piezo actuators inside. After a baking period of one month, the system pressure pressure settled to 1.5x10^{-6}mbar. The ion and sublimation pumps were fired to remove any adsorbed material, and the pressure continued to decline. After reducing the system back to ambient room temperature and allowing the ion pump to run continuously, the pressure settled to 3.0x10^{-10}mbar.

7.5 Imaging System

Above the trapping region there is an opening in the top mount for optical access for fluorescence detection of the ions. We use a Nikon 5X lens outside of vacuum close to the chamber to collect the maximum available light. While we can use the cavity to detect UV photons, direct line of sight of the trap center is advantageous for knowing the exact number of ions present. The camera system we use to detect the ion fluorescence is an Andor Xyla CMOS. Due to the small size of the trap geometry, there is significant scattering of light from the nearby electrodes. To minimise the scatter we focus the input beams to a waist of 10μ as they pass through the trap center. Figures 7.25a and 7.25b show the scatter of a 423nm beam with and without focusing the laser respectively at 68μW.

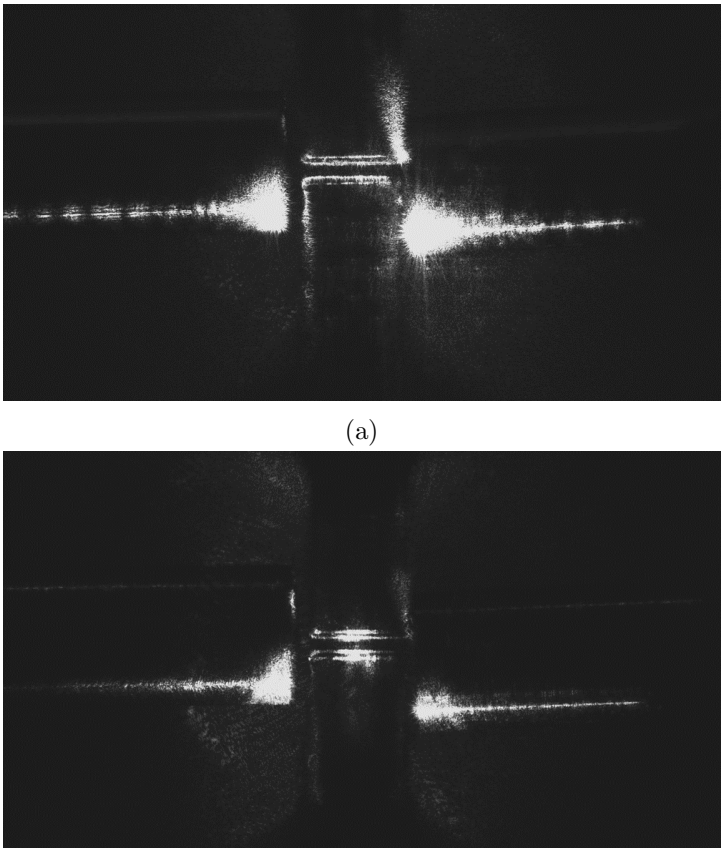

(a)

(b)

Figure 7.25: (**a**) View from above the trap of the magnified electrodes illuminated by 423nm light. A filter has been applied so only 423nm scatter is detected. The white regions have count rates of 1,000-4,000 cps. (**b**) Reduced scatter rate aroud the trap region by focusing the laser to a waist of 10μ. The count rate in the trapping region is 100-140cps.

7.5.1 Beam Path

The lasers are fibre-coupled onto the table, this provides a clean TEM_{00} mode. To minimise the laser waist at the trap center the beam is first brought to a focus using the lens of the fibre collimator, where we place

a 50μm pinhole. The beam expands up to a lens with a 50mm focal length. The trap is situated at this focal point. The lens is mounted on a stage to get the position correct. This setup is shown in figure 7.26.

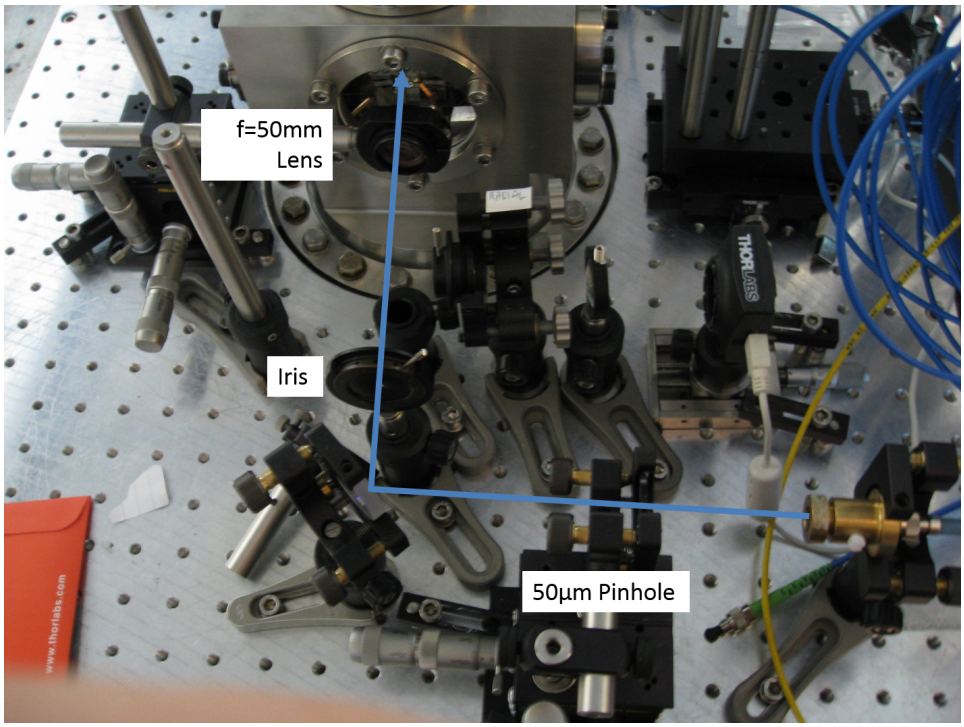

Figure 7.26: Beampath of the 423nm laser for atomic calcium excitation, highlighted in blue.

Chapter 8

Conclusion

The machining technique demonstrated has produced fibres with large radius of curvature, capable of supporting stable FFPCs up to 700μm. The rotation between machining laser pulses has produced mirror surfaces with a low ellipticity, allowing cavities that exhibit a polarisation mode splitting of less than 1.16MHz. The singlemode fibre cavities are limited by an additional structure around the singlemode fibre core, but can still support cavities up to 450μm when coupled with a multimode fibre. The finesse attainable across all the prepared fibres is 40,000-45,000, but which did not improve when annealed in air.

Once the background scatter had been reduced, we attempted to see atomic excitation of the atomic calcium beam passing through the 423nm laser. The atomic transition is at 422.79167nm, which we scanned around by 100Mhz to each side. On the camera, there was no discernible change from the background scatter rate. We also used a PMT with a 423nm filter on the output of the multimode cavity fibre to detect the fluorescence count rate and observed the same result.

The oven was increased in power from 1W up to 6W but no discernible change in count rate appeared. After running at 6W ther was a noticeable shift in the oven position, caused by the heating of the wires. As a result of the lack of guiding ceramic, the oven had listed to one side, and was no longer pointing towards the collimator. On closer inspection, the oven was noticed to shift position for 2.5W of power applied.

The reduction in cavity finesse as a result of the electrodes clipping the cavity mode is difficult to avoid in this system. There is no deterministic way in the current system of adjusting the cavity and trapping axes accurately enough to account for the offset angles. For the current system, this could be partially solved by withdrawing the RF electrodes further away. Using the model presented in section 7.2.4, at 75μm separation, the clipping of the cavity mode does not occur until 4-5°. The existing structure we have at least as good as 3° alignment, for which the finesse would maintain it's maximum value, assuming the cavity mode is well overlapped with the RF center. This does however reduce the trap depth. Similarly the range over which the cavity and RF need scanning increases also, for which an additional flexure stage could be introduced to aid with.

The setup is complete still and under UHV conditions. While the atomic flux passing through the trap is very small due to the oven misalignment, it is possible that if even a small sample of atoms are present, they could be ionised and trapped within the system as it is. Failing that, the trap requires opening to atmosphere and the oven replaced. If this is done, it is possible to retry closing and trapping once

more but keeping the power supplied to the oven below 2.5W. If this succeeds this would allow experimental values of the trap's heating rate and secular frequency to be obtained, while also attempting to couple the ion to the low-finesse cavity mode. For strong coupling experiments, the cavity needs realigning to be precisely overlapped with the RF center, possibly through the use of an additional stage within the system.

The fibre machining process is now being applied to GRIN (GRaded INdex) fibres which can act as a lens for focusing outcoming laser light to increase the modematching of light into the cavity to over 90%. The optimal way to machine these fibres and to confirm their focusing properties after machining are under current investigation.

Bibliography

[1] W. Neuhauser, M. Hohenstatt, P. E. Toschek, and H. Dehmelt. Localized visible ba+ mono-ion oscillator. Phys. Rev. A, 22:11371140, Sep 1980. doi: 10.1103/PhysRevA.22.1137

[2] E. Schrodinger, Are there quantum jumps? part ii, British Journal for the Philosophy of Science, vol. 3, no. 11, pp. 233-242, (1952).

[3] M.T.Bell, T.P.Softley, Ultracold molecules and ultracold chemistry *Molecular Physics: An International Journal at the Interface Between Chemistry and Physics, Vol 107, Issue 2, 2009*

[4] S.Willitsch, M.T.Bell, A.D.Gingell, J.M.Oldham, T.P.Softley, Ion-molecule chemistry at very low temperatures: cold chemical reactions between Coulomb-crystallized ions and velocity-selected neutral molecules *Faraday Discussions, Volume 142, Cold and Ultracold Molecules 12 May 2009*

[5] S.Willitsch, Coulomb-crystallised molecular ions in traps: methods, applications, prospects, *Internation Reviews in Physical Chemistry, Vol 31, Issue 2, 2012*

[6] S.Willitsch, M.T.Bell, A.D.Gingell, T.P.Softley, Chemical applications of laser- and sympathetically-cooled ions in ion traps *Physical Chemistry Chemical Physics vol 10, No. 48, 28 December 2008*

[7] S. Haroche; D. Kleppner (1989). "Cavity Quantum Electrodynamics". Physics Today: 2430. doi:10.1063/1.881201. `https://www.chem.purdue.edu/courses/chm374/Articles%20etc/Haroche89.pdf`

[8] H. J. Kimble, Strong Interactions of Single Atoms and Photons in Cavity QED, Physica Scripta, Volume 1998, T76 (1998)

[9] J. I. Cirac, P. Zoller, H. J. Kimble, and H. Mabuchi. Quantum state transfer and entanglement distribution among distant nodes in a quantum network. Phys. Rev. Lett., 78:32213224, Apr1997. doi: 10.1103/PhysRevLett.78.3221

[10] D. W. Vernooy, V. S. Ilchenko, H. Mabuchi, E. W. Streed, and H. J. Kimble, High-Q measurements of fusedsilica microspheres in the near infrared, Opt. Lett. 23, 247249 (1998)

[11] H. J. Kimble, The Quantum Internet, Nature, 453, 1023-1030 (2008)

[12] D. Armani, T. Kippenberg, S. Spillane, and K. Vahala, Ultra-high-Q toroid microcavity on a chip, Nature 421, 925928 (2003)

[13] J. Thompson, T. Tiecke, N. de Leon, J. Feist, A. Akimov, M. Gullans, A. Zibrov, V. Vuletić, and M. Lukin, Coupling a single

trapped atom to a nanoscale optical cavity, Science 587, 12021205 (2013).

[14] M. Steiner, H. M. Meyer, C. Deutsch, J. Reichel, and M. Köhl, Single ion coupled to an optical fiber cavity, Phys. Rev. Lett. 110, 043003 (2013)

[15] Y. Colombe, T. Steinmetz, G. Dubois, F. Linke, D. Hunger, and J. Reichel, Strong atom-field coupling for Bose-Einstein condensates in an optical cavity on a chip, Nature 450, 272276 (2007).

[16] N. E. Flowers-Jacobs, S.W. Hoch, J. C. Sankey, A. Kashkanova, a. M. Jayich, C. Deutsch, J. Reichel, and J. G. E. Harris, Fiber-cavity-based optomechanical device, Appl. Phys. Lett. 101, 221109 (2012)

[17] K. Ott, S. Garcia, R. Kohlhaas, P. Rosenbusch, J. Reichel. Long high finesse fiber Fabry-Pérot resonators. Proc. SPIE 9634, 24th International Conference on Optical Fibre Sensors, 96341L (28 September 2015); doi: 10.1117/12.2193901

[18] P.W.H.Pinkse, G.Morigi, M.Kowalewski, Cavity cooling of internal and external degrees of freedom of molecules, *International Quantum Electronics Conference. CLEOE-IQEC 2007 17-22 June 2007, Munich*

[19] H. Takahashi, J. Morphew, F.Oruĉević, A. Noguchi, E. Kassa, M. Keller (2015) Novel laser machining of optical fibers for long cavities with low birefringence, Optics Express Vol 22, Issue 25 doi: 10.1364/OE.22.031317, URL:

https://www.osapublishing.org/oe/abstract.cfm?uri=oe-22-25-31317

[20] B.Brandstätter, A.McClung, K.Schüppert B.Casabone, K.Friebe, A.Stute, P.O.Schmidt, C.Deutsch, J.Reichel, R.Blatt, T.E.Northup, Integrated fiber-mirror ion trap for strong ion-cavity coupling, *Review of Scientific Instruments 84, ArXiv: 1311.6961v1, doi: 10.1063/1.4838696, 2013*

[21] F. L. Kien and K. Hakuta. Density operator and applications in nonlinear optics lecture course (2004)

[22] K.R.Brown, A.C.Wilson, Y.Colombe, C.Ospelkaus, A.M.Meier, E.Knill, D.Leibfried, D.J.Wineland, Single-Qubit-Gate Error Below 10^{-4} in a trapped ion. *arXiv: 1104.2552v2 2012*

[23] C.W.Chou, D.B. Hume, J.C.J.Koelemeij, D.J. Wineland, T.Rosenband, Frequency Comparison of Two High-Accuracy Al^+ Optical Clocks. *Physical Review Letters 104, 070802, 2010*

[24] F.M. Penning, The glow discharge at low pressure between coaxial cylinders in an axial magnetic field, Physica, 3, 873 (1936)

[25] W. Paul, H. Steinwedel, Quadropole mass filter, (1953)

[26] D. J. Griffiths, Introduction to Electrodynamics, Pearson Education Inc (1999)

[27] P. Ghosh. Ion Traps. Clarendon Press, 1995.

[28] A. Mortensen. Aspects of Ion Coulomb Crystal based Quantum Memory for Light. PhD thesis, 2005

[29] K. Sheridan. Experimental Techniques for Cold Chemistry and Molecular Spectroscopy in an Ion Trap. PhD thesis, 2012

[30] E, M. Purcell, H, C. Torrey, and R. V. Pound Radiation Laboratory, Massachusetts Institute of Technology, Cambridge, Massachusetts December 24, 1945 http://journals.aps.org/pr/pdf/10.1103/PhysRev.69.37

[31] Kogelnik and T. Li. Laser beams and resonators. Applied Optics, 5(10):15501567, 1966.URL http://www.opticsinfobase.org/abstract.cfm?URI=ao-5-10-1550

[32] Image from Wikimedia Commons: https://commons.wikimedia.org/wiki/File:Hermite-gaussian.png

[33] Image courtesy of A. Sharma, Atom Cavity Interactions with Hot and Cold Atomic Vapors, Ph.D Thesis (2013)

[34] Geoffrey Brooker. Modern Classical Optics (Oxford Master Series in Atomic, Optical and Laser Physics). Oxford University Press, USA, October 2003. ISBN 019859965X. URL http://www.amazon.com

[35] Paul Davies. Quantum Mechanics. Routledge & Kegan Paul, London and New York, 1987.

[36] Rodney Loudon. The Quantum Theory of Light (Oxford Science Publications). Oxford University Press, USA, 3 edition, September 2000. ISBN 0198501765.

[37] A. Kuhn and D. Ljunggren. Cavity-based single-photon sources. Contemporary Physics, 51:289-313, 2010.

[38] E. T. Jaynes and F. W. Cummings. Comparison of quantum and semiclassical radiation theories with application to the beam maser. Proceedings of the IEEE, 51(1):89109, January 1963. ISSN 0018-9219. doi: 10.1109/PROC.1963.1664

[39] Bruce W. Shore and Peter L. Knight. The Jaynes-Cummings Model. Journal of Modern Optics, 40(7):11951238, July 1993.

[40] W. T. Silfvast. Laser Fundamentals 2nd Edition Cambridge University Press 2004

[41] M. Keller , B. Lange , K. Hayasaka , W. Lange & H. Walther (2004), A calcium ion in a cavity as a controlled single-photon source, NJP, URL http://iopscience.iop.org/article/10.1088/1367-2630/6/1/095/meta

[42] M. Keller , B. Lange , K. Hayasaka , W. Lange & H. Walther (2007) Stable long-term coupling of a single ion to a cavity mode, Journal of Modern Optics, 54:11, 1607-1617, DOI: 10.1080/09500340600792911

[43] M.Fox, Quantum Optics, and Introduction *Oxford Press 2006 ISBN: 978-0-19-856673-1*

[44] M. C. Munnix, A. Lochmann, D. Bimberg, V.A. Haisler Modeling Highly Efficient RCLED-Type Quantum-Dot-Based Single Photon Emitters (2009), IEEE Photonics Society

[45] R. J. Thomson, G. Rempe, H. J. Kimble, Observation of Normal-Mode Splitting for an Atom in an Optical Cavity, PRL Vol 68, No. 8 (1991)

[46] W.D.Phillips. *Laser cooling and trapping of neutral atoms.* S0034-6861(98)00603-5

[47] K.Sheridan, M.Keller. Weighing of trapped ion crystals and its applications *New Journal of Physics, 2011 doi:10.1088/1367-2630/13/12/123002*

[48] E.S.Shuman, J.F.Barry, D.Demille, Laser Cooling of a Diatomic Molecule *Nature Letters, vol 467, 2010 doi:10.1038/nature09443*

[49] D.F.V James, Quantum Dynamics ofcold trapped ions with application to quantum computation *Applied Physics B66, 181-190, 1998*

[50] P.Atkins & R.Friedman *Molecular Quantum Mechanics Chapters 8, 10 & 11*

[51] B.H.Bransden & C.J.Joachain *Physics of Atoms and Molecules Chapters 10 & 11*

[52] B.Roth, U.Fröhlich, and S.Schiller, Sympathetic cooling of 4He+ ions in a radiofrequency trap, *arXiv:physics/0412053v1 physics.atom-ph 2004*

[53] A.Ostendorf, C.B.Zhang, M. A. Wilson, D.Offenberg, B.Roth, and S.Schiller, Sympathetic Cooling of Complex Molecular Ions to Millikelvin Temperatures *PRL 97, 243005, 2006*

[54] W.G.Rellergert, S.T.Sullivan, S.J.Schowalter, S.Kotochigova, K.Chen, E.R.Hudson, Evidence for sympathetic vibrational cooling of translationally cold molecules *Nature Letters vol 495, doi:10.1038/nature11937, 2013*

[55] L.S.Vogelius, L.B.Madsen, M.Drewsen, Blackbody-Radiation-Assisted Laser Cooling of Molecular Ions, *PRL Vol. 89, No. 17 2002, DOS: 10.1103/PhysRevLett.89.173003*

[56] P.F. Staanum, Klaus Højbjerre, P.S.Skyt, A.K.Hansen, M.Drewsen, Rotational laser cooling of vibrationally and translationally cold molecular ions *Nature Physics, Vol6, 2010 DOI: 10.1338/NPHYS1604*

[57] P.Maunz, T.Puppe, I.Schuster, N.Syassen, P.W.H.Pinkse, G.Rempe, Cavity Cooling of a Single Atom, *Nature Letters, Vol 428, 2004*

[58] M.Keller, B.Lange, K.Hayasaka, W.Lange, H.Walther, Continuous generation of single photons with controlled waveform in an ion-trap cavity system. *Nature Letters, 431 doi:10.1038/nature02961*

[59] H.Takahashi, A.Wilson, A.Riley-Watson, F.Oruĉević, N.Seymour-Smith, M.K.Keller, W.Lange, An integrated fiber trap for single-ion photonics. *New Journal of Physics 15 (053011). ISSN 1367-2630*

[60] K.Sheridan, M.Keller, Weighing of trapped ion crystals and its applications, *New Journal of Physics 13, 123002, 2011*

[61] K.Sheridan, N.Seymour-Smith, A.Gardner, and M.Keller, All-optical broadband excitation of the motional state of trapped ions *European Physical Journal D, DOI: 10.1140, 2012*

[62] D.Hunger, T.Steinmetz, Y.Colombe, C.Deutsch, T.W.Hänsch, and J. Reichel, A fiber Fabry Perot cavity with high finesse, *New Journal of Physics 12, 065038, 2010*

[63] D.Hunger, C.Deutsch, R.J.Barbour, R.J.Warburton, and J.Reichel, Laser micro-fabrication of concave, low-roughness features in silica, *AIP Advances 2, 012119, 2012*

[64] M.Hijlkema, B.Weber, H.P.Specht, S.C.Webster, A.Kuhn, and G.Rempe, A single-photon server with just one atom, *Nature Physics 3, 253255, 2007*

[65] S.Ritter, C.Nölleke, C.Hahn, A.Reiserer, A.Neuzner, M.Uphoff, M.Mücke, E.Figueroa, J.Bochmann, and G.Rempe, An elementary quantum network of single atoms in optical cavities. *Nature 484, 195200, 2012*

[66] http://www.ivgfiber.com/datasheetsinglemode.pdf

[67] M. Uphoff, M. Brekenfeld, G. Rempe, and S. Ritter, Frequency splitting of polarization eigenmodes in microscopic Fabry-Perot cavities, arXiv:1408.4367 (2014).

[68] Figure courtesy of H. Takahashi, ITCM, University of Sussex 2014

[69] N. R Seymour-Smith. Ion-trap caviy QED system for probabilistic entanglement. PhD Thesis, 2011

[70] S. Begley, M. Vogt, G.K. Gulati, H. Takahashi, M. Keller (2016) Optimised Multi-Ion Cavity Coupling. Phys. Rev. Lett 116, 223001

[71] J. Gallego, S. Ghosh, S.K. Alavi, W. Alt, M. Martinez-Dorantes, D.Meschede, L.Ratschbacher. High Finesse Fiber Fabry-Perot Cavities: Stabilization and Mode Matching Analysis Applied Physics B (2016) 122: 47.doi:10.1007/s00340-015-6281-z

[72] M. Harlander, M. Brownnutt, W. Hänsel, R. Blatt. Trapped-ion probing of light-induced charging effects on dielectrics, New Journal of Physics, Vol 12, September 2010

[73] A. Seco, H. Takahashi, M. Keller, Novel Ion Trap Design for Strong Ion-Cavity Coupling. *Atoms* 2016, 4, 15.

[74] https://www.openoptogenetics.org/images/5/59/Guide_to_Connectorization_and_Polishing_of_Optical_Fibers.pdf

[75] http://research.physics.illinois.edu/bezryadin/labprotocol/stycast2850.pdf

[76] http://www.noliac.com/products/actuators/shear-plate/kind/card/cardaction/pdf/cardcontroller/Card/show/csap03/pagetype/67589/

[77] https://www.physikinstrumente.com/en/products/piezoceramic-actuators/shear-actuators/p-111-p-151-pica-shear-actuators-102900/?type=5600&downloadUid=895&downloadFileUid=798&cHash=1672d90aa8267d8f0344569461427f7e

[78] http://pi2013.pi-sales.de/download/PI_Datenblatt_P-882_-_P-888$_2$0150123.*pdf*

[79] http://www.epotek.com/site/administrator/components/com_products/assets/files/Style_Uploads/353ND.pdf